



University of Kentucky  
UKnowledge

---

University of Kentucky Doctoral Dissertations

Graduate School

---

2006

## SOLUTION AND SOLID STATE INTERACTIONS BETWEEN IONIC $\pi$ -SYSTEMS

Jing Chen

University of Kentucky, [jchen4@uky.edu](mailto:jchen4@uky.edu)

[Right click to open a feedback form in a new tab to let us know how this document benefits you.](#)

---

### Recommended Citation

Chen, Jing, "SOLUTION AND SOLID STATE INTERACTIONS BETWEEN IONIC  $\pi$ -SYSTEMS" (2006).

*University of Kentucky Doctoral Dissertations*. 289.

[https://uknowledge.uky.edu/gradschool\\_diss/289](https://uknowledge.uky.edu/gradschool_diss/289)

This Dissertation is brought to you for free and open access by the Graduate School at UKnowledge. It has been accepted for inclusion in University of Kentucky Doctoral Dissertations by an authorized administrator of UKnowledge. For more information, please contact [UKnowledge@lsv.uky.edu](mailto:UKnowledge@lsv.uky.edu).



ABSTRACT OF DISSERTATION

Jing Chen

The Graduate School  
University of Kentucky  
2006

SOLUTION AND SOLID STATE INTERACTIONS  
BETWEEN IONIC  $\pi$ -SYSTEMS

---

ABSTRACT OF DISSERTATION

---

A dissertation submitted in partial fulfillment of the  
requirements for the degree of Doctor of Philosophy  
in the College of Arts and Sciences  
at the University of Kentucky

By

Jing Chen

Lexington, Kentucky

Director: Dr. Arthur Cammers, Associate Professor of Chemistry

Lexington, Kentucky

2006

Copyright © Jing Chen 2006

## ABSTRACT OF DISSERTATION

### SOLUTION AND SOLID STATE INTERACTIONS BETWEEN IONIC $\pi$ -SYSTEMS

Although attractive interactions between  $\pi$  systems ( $\pi$ - $\pi$  interaction) have been known for many years, understanding of its origin is still incomplete. Quantitative measuring of  $\pi$ -stacking is challenging due to the weak nature of the  $\pi$ - $\pi$  interaction. This dissertation aims at elucidating a quantitative conformational analysis by NMR ring current anisotropy of an organic compound capable of intramolecular  $\pi$ -stacking in solution and studying charge effects on the stacking of  $\pi$ -systems. This dissertation offers four contributions to the area. (1) A general approach to four-state, conformational analysis based on the magnetic anisotropy of molecules undergoing fast dynamic exchange is described. (2) Study unveiled the importance of charges in the conformation of a dication in the solution. (3) Novel aromatic salt pairs of triangulene derivatives with the delocalized cation-anion interaction were synthesized and studied. (4) Study unveiled ionic  $\pi$ -systems preferred face-to-face stacking due to strong cation- $\pi$  and anion-cation attractions.

A general protocol for the application of magnetic anisotropy to quantitative multi-state conformational analysis of molecules undergoing fast conformational exchange was suggested in the current study. The reliability of this method of conformational analysis was checked by the mass balance. VT-NMR was also conducted to study the enthalpic parameters. This technique can be further used to study canonical interactions such as ion pairing, hydrogen bonding, and molecular recognition.

In the current study, dependence of the probe conformations on the dispersive interactions at the aromatic edges between solvent and probes was tested by conformational distributions of the fluorinated derivatives (**2b** and **2c**) of the probe molecule (**1a**). Solution and solid studies of these molecules put the previous conclusion drawn by the Cammers group in question. Current studies show that the dispersive interaction at the aromatic edge could not be the predominant force on the conformational changes in the probe molecule **1a** during the fluoroalkanol perturbation. This study indicated that charges might be important in the formation of the folding conformations in the solution and solid state of **1a**, **2b**, and **2c**. A contribution of this thesis was to prepare and study a conformational model that lacked charges. The previous molecules were charged.

The solid-state structures of pyridinium-derived aromatic rings from the CSD (Cambridge Structural Database) were studied to investigate the  $\pi$ - $\pi$  interaction between cationic  $\pi$ -systems in solid state. Novel aromatic salt pairs of triangulene derivatives with the delocalized cation-anion interaction were synthesized to study the  $\pi$ - $\pi$  interaction between two aromatic rings that carried opposite charges. This study showed that the interaction between ionic  $\pi$ -systems can be enhanced by cation- $\pi$  and anion-cation attractions. The stackings of these  $\pi$ -systems introduce more overlap, closer packing and stronger atomic contact than that of the solid states of comparable neutral species. Cation- $\pi$  and anion-cation attractions are synergistic in aromatic salts.

KEYWORDS: Conformation analysis, Pyridinium-derived aromatic rings, Aromatic salt pairs, Cation- $\pi$  interaction, Anion-cation attraction.

---

---

SOLUTION AND SOLID STATE INTERACTIONS  
BETWEEN IONIC  $\pi$ -SYSTEMS

By  
Jing Chen

---

Director of Dissertation

---

Director of Graduate Studies

---





DISSERTATION

Jing Chen

The Graduate School  
University of Kentucky  
2006

SOLUTION AND SOLID STATE INTERACTIONS  
BETWEEN IONIC  $\pi$ -SYSTEMS

---

DISSERTATION

---

A dissertation submitted in partial fulfillment of the  
requirements for the degree of Doctor of Philosophy  
in the College of Arts and Sciences  
at the University of Kentucky

By

Jing Chen

Lexington, Kentucky

Director: Dr. Arthur Cammers, Associate Professor of Chemistry

Lexington, Kentucky

2006

Copyright © Jing Chen 2006

Dedicated to  
My parents

## Acknowledgements

The following dissertation is the result of five years' individual work during which I have been supported by many people. I am glad to have the opportunity to express my gratitude to all of them.

I would like to express my deep and sincere gratitude to my advisor, Dr. Arthur Cammers, whose wide knowledge, logic, and dedication to science have made a deep impression on me. His understanding, stimulating suggestions, and encouragement supported me throughout the research for this dissertation. I would like to thank Dr. Robert B. Grossman, Dr. Lynn S. Penn, and Dr. Dong-Sheng Yang, for their service on my advisory committee. I would also like to thank Dr. Robert D. Guthrie and Dr. Mark S. Meier, the directors of Graduate Studies of the Chemistry Department, for their academic advice. Also, I would like to acknowledge my appreciation of the professors who imparted to me the knowledge of advanced chemistry, which was invaluable in my dissertation research.

I would also like to express my thanks to members of Dr. Cammers' research group: Xugang Guo, Marlon D. Jones, Sihui Long, Pramod Prasad Poudel, Dr. Muthusamy Venkatraj, and Dr. Yan Zhu, for helpful ideas and discussions.

Many thanks go to Dr. Jack Goodman, Mr. John Layton and Dr. Sean Parkin, for help with mass spectrometry, NMR and X-ray diffraction.

Finally, I wish to express my gratitude to my family. I'd particularly like to thank my parents, Yiming Chen and Yuying Pan, to whom I owe everything. I feel a deep sense of gratitude for my brother, Dan Chen, who encouraged and supported me to pursue the Ph.D. degree. I would also like to thank my parents-in-law, Mingde Ji and Xiangyuan Huang, for their encouragements and helps. My special thanks go to my wife, Huihua Ji, and sons, Jiningnan Chen and Jason Chen, for their love and support during the Ph.D. period.

## Table of Contents

Acknowledgements.....	III
List of Tables.....	IX
List of Figures.....	XI
<b>Chapter one:</b> Exploring conformational dynamics of $\pi$ system by NMR.....	1
1.1 $\pi$ - $\pi$ interaction and $\pi$ -stacking.....	3
1.1.1 $\pi$ - $\pi$ interaction, weak force on the level of van der Waals attraction.....	3
1.1.2 Simple $\pi$ -stacking.....	5
1.1.3 Canonical intramolecular interactions.....	5
1.1.3.1 van der Waals interaction.....	6
1.1.3.2 Hydrogen bonding.....	6
1.1.3.3 Solvophobic effect.....	6
1.1.3.4 Pauli repulsion.....	7
1.1.3.5 Charge transfer.....	7
1.2 Models used to explain the $\pi$ - $\pi$ interactions.....	8
1.2.1 Solvophobic model.....	8
1.2.2 Electron donor-accepter or charge transfer model.....	9
1.2.3 Quadrupole interaction model.....	10
1.2.4 Atomic charge model.....	11
1.2.5 Electrostatic model.....	12
1.3 Exploring conformational dynamics of $\pi$ system by NMR.....	13
1.3.1 Chemical shift and shielding.....	13
1.3.2 Ring current effects in benzene.....	15
1.3.3 NMR shielding can be accurately calculated.....	16
1.3.4 Conformation changes NMR spectrum.....	17

1.3.5	Models of $\pi$ system for quantification of conformations in solution state.....	17
1.3.5.1	Two-state models.....	18
1.3.5.2	Three-state model of previous work of the Cammers group.....	19
1.4	Quantitative four-state conformational analysis .....	22
1.4.1	Conformational search.....	23
1.4.2	Calculation of chemical shift differences of <b>1a</b> , <b>2b</b> , and <b>2c</b> versus <b>1d</b> in four states.....	26
1.4.3	Calculation of conformational distributions of <b>1a</b> , <b>2b</b> , and <b>2c</b> .....	29
1.4.4	Results and discussion.....	30
1.4.4.1	Reliability of coefficients for the equations.....	30
1.4.4.2	Solution state study---DMSO perturbation of aqueous solution.....	31
1.4.4.2.1	Edgewise dispersive interactions.....	31
1.4.4.2.2	Quadrupole moment interactions.....	33
1.4.4.2.3	Electrostatic interactions between aromatic rings.....	34
1.4.4.2.4	Thermodynamic study.....	36
1.4.4.3	Solid-state study.....	38
1.5	Study of neutral hydrocarbon compound <b>2e</b> .....	39
1.6	Conclusion.....	40
	References.....	43
<b>Chapter Two: The face-to-face, cation-to-cation packing motif in the solid state of simple pyridinium-derived aromatic rings.....</b>		
2.1	Introduction.....	50

2.1.1	Interaction between charges.....	50
2.1.2	C-H/ $\pi$ interactions.....	50
2.1.3	Packing modes in fused-ring aromatic hydrocarbons.....	51
2.1.4	Cation- $\pi$ interaction.....	54
2.1.5	Delocalized cation- $\pi$ interaction.....	55
2.2	Face-to-face packing motif in simple pyridinium crystals.....	55
2.2.1	Pyridinium and nitrogen substituted fused-ring aromatic hydrocarbons.....	55
2.2.2	Methodology.....	56
2.2.2.1	CSD code, packing patterns and the calculation of overlap percentages.....	56
2.2.2.2	Counterions .....	57
2.2.2.3	Definition of pseudo.....	57
2.3	Pyridinium, one-ring cation.....	57
2.3.1	Counterions forming structures of endless hydrogen-bond connections.....	60
2.3.1.1	3D structures formed by counterions.....	60
2.3.1.2	2D structures formed by counterions.....	62
2.3.1.3	1D structures formed by counterions.....	62
2.3.2	Aromatic counterions.....	63
2.3.3	Simple counterions.....	66
2.3.3.1	Small size simple counterions.....	66
2.3.3.2	Large size counterions.....	68
2.3.3.3	Large size counterions with neutral molecules (protonated counterions).....	69
2.4	Cations of naphthalene type aromatic systems (two-ring cations).....	70
2.4.1	Hydrogen-bond structures of the counterions.....	72

2.4.2	Aromatic counterions.....	73
2.4.3	Simple counterions.....	73
2.5	Cations of anthracene and phenanthrene type aromatic systems (three-ring cations).....	74
2.5.1	Aromatic counterions.....	76
2.5.2	Simple counterions.....	77
2.5.2.1	Simple nonaromatic counterions .....	77
2.5.2.2	Simple nonaromatic counterions with neutral aromatic compounds.....	78
2.5.3	Dications.....	79
2.6	Cations of benzanthracene type aromatic systems (four-ring cations)...	80
2.7	Delocalized cation enhanced cationic $\pi$ - $\pi$ interactions.....	82
2.7.1	Delocalized cation- $\pi$ interaction.....	82
2.7.2	Assumptions for the calculation.....	84
2.7.3	Dipole-dipole interaction.....	85
2.7.4	Ion-dipole interaction.....	86
2.7.5	Molecular orbital study.....	87
2.8	Conclusion.....	88
	References.....	89
<b>Chapter Three:</b>	<b><math>\pi</math>-<math>\pi</math> interaction in the Solid state of triangulene salt pairs.....</b>	<b>92</b>
3.1	Introduction.....	93
3.1.1	Fused, flat, benzenoid hydrocarbons with $D_{3h}$ symmetry.....	93
3.1.2	Triangulene type cations and anions.....	96
3.1.3	Cation- $\pi$ interaction and cationic $\pi$ - $\pi$ interaction.....	97
3.2	Solid-state study of triangulene salt pairs.....	97
3.2.1	Solid-state study of salts of triangulene cation and nonaromatic counterion.....	97



3.2.2	Solid-state study of salts of triangulene anion and nonaromatic counterion.....	101
3.2.3	Solid-state study of triangulene salt pairs.....	103
3.2.3.1	Novel delocalized, flat, aromatic ionic salt pair.....	103
3.2.3.2	Solid-state study.....	103
3.3	Delocalized cation-anion pair enhanced $\pi$ - $\pi$ interactions.....	107
3.3.1	Delocalized cation-anion pair coulombic attraction.....	107
3.3.2	Delocalized cation- $\pi$ interaction.....	108
3.3.3	Other interactions: anion- $\pi$ repulsion, dipole-dipole, and ion-dipole interactions.....	108
3.3.4	Cationic $\pi$ -system dimer versus cation-anion $\pi$ -system dimer.....	109
3.4	Molecular orbital study.....	111
3.5	Conclusion.....	113
	References.....	114
	<b>Chapter Four: Conclusions.....</b>	<b>116</b>
	<b>Chapter Five: Experimental section.....</b>	<b>119</b>
5.1	Experiments of Chapter one.....	119
5.2	Experiments of Chapter three.....	121
	References.....	128
	Appendix.....	129
	Vita.....	167

## LIST OF TABLES

Table 1.1.	Chemical shifts differences of <b>1a</b> , <b>2b</b> , and <b>2c</b> , versus <b>1d</b> . Values are in ppm. Values marked with an asterisk (*) were substituted by 0 due to overestimation in gas-phase calculation. In the first column, <i>a1a</i> is the proton <i>H<sub>a</sub></i> of the molecule <b>1a</b> (shown in italic).....	26
Table 1.2.	Enthalpies of conformers from van't Hoff analysis in pure D <sub>2</sub> O and DMSO (kcal/mol).....	36
Table 2.1.	Parameters defining four types of packing patterns in the crystals of planar or near planar polynuclear aromatic hydrocarbons.....	52
Table 2.2.	CSD codes, corresponding counterions, packing patterns and the overlaps of pyridinium crystals.....	58
Table 2.3.	Pyridinium crystals with aromatic counterions. Pattern 1 is viewed from pyridinium only and pattern 2 includes all the aromatic rings inside the crystals, including the pyridinium and the counterion.....	63
Table 2.4.	Pyridinium crystals with small size simple counterions.....	67
Table 2.5.	Pyridinium crystals with larger size simple counterions.....	68
Table 2.6.	Pyridinium crystals with anions and neutral molecules (protonated anions).....	69
Table 2.7.	CSD codes, corresponding counterions, packing patterns, and overlaps of two-ring pyridinium crystals. <i>d</i> is interplanar distance.....	71
Table 2.8.	Two-ring pyridinium crystals with hydrogen-bond structure of counterions.....	72
Table 2.9.	Two-ring pyridinium crystals with aromatic counterions. Pattern 1 includes pyridinium only while pattern 2 includes all aromatic rings (pyridinium and counterion) inside the crystals.....	73

Table 2.10.	Two-ring pyridinium crystals with simple counterions.....	74
Table 2.11.	CSD codes, corresponding counterions, packing patterns, and overlaps of three-ring pyridinium crystals. Cat-cat is Cation-cation, d is interplanar distance.....	75
Table 2.12.	Three-ring pyridinium crystals with aromatic counterions. Pattern 1 includes pyridinium only while pattern 2 includes all aromatic rings (pyridinium and counterion) inside the crystals.....	77
Table 2.13.	Three-ring pyridinium crystals with simple nonaromatic counterions.....	78
Table 2.14.	Three-ring pyridinium crystals with simple nonaromatic counterions and neutral aromatic compounds.....	79
Table 2.15.	Three-ring dicationic pyridinium crystals.....	80
Table 2.16.	Four-ring pyridinium crystals.....	80
Table 2.17.	Electrostatic and dispersion energies of benzene. $E_{es}$ is electrostatic interaction energies, $E_{rep}$ is repulsion interaction energies, and $E_{corr}$ is correlation interaction energies.....	84
Table 3.1.	Triazatriangulenium crystals.....	99
Table 3.2.	Parameters of crystal structures of tripropyltriazatriangulenium trioxytriangulene ( <b>3.16</b> ), tripropyltriazatriangulenium tetrafluoroborate ( <b>3.6D</b> ), and tetrabutylammonium trioxytriangulene ( <b>3.1E</b> ).....	104
Table 3.3.	Major interactions between two $\pi$ -systems in a cationic $\pi$ -system dimer versus that between two $\pi$ -systems in a cation-anion $\pi$ -system dimer.....	109

## LIST OF FIGURES

Figure 1.1.	Charged compounds ( <b>1a</b> , <b>2b</b> , <b>2c</b> , and <b>1d</b> ) and neutral compounds ( <b>2e-f</b> ).....	1
Figure 1.2.	Some conformers of benzene dimer. <b>FFEC</b> and <b>EF</b> are the most stable dimers.....	3
Figure 1.3.	Calculated energy of <b>FFCC</b> , <b>FFEC</b> , and <b>EF</b> $\pi$ - $\pi$ interactions.....	4
Figure 1.4.	Quadrupole models of $C_6F_6$ and $C_6H_6$ .....	10
Figure 1.5.	Atomic charge model.....	11
Figure 1.6.	Electrostatic model of benzene ring.....	12
Figure 1.7.	Electrostatic models for $\pi$ - $\pi$ interaction.....	12
Figure 1.8.	Magnetic dipole generated by nuclei spins on the nuclear axis .....	14
Figure 1.9.	Energy difference of proton in a magnetic field $B_0$ .....	14
Figure 1.10.	“Ring current” effect.....	15
Figure 1.11.	Models for $J$ -coupling calculations.....	17
Figure 1.12.	Two-state systems.....	18
Figure 1.13.	Model <b>1a</b> and some three-ring system conformations from conformational search in previous study of the Cammers group.....	20
Figure 1.14.	Examples of perturbation of <b>1a</b> in aqueous solution with fluoroalkanol and alkanol cosolvents in previous study of Cammers group.....	21
Figure 1.15.	<b>C</b> , <b>F</b> , and <b>S</b> conformers of <b>1a</b> , <b>2b</b> , and <b>2c</b> , the $H_a$ , $H_b$ , and $H_c$ are shown in <b>1a</b> . Only two rings are shown, the pyridine rings, H and/or F atoms are omitted for clarity. In each conformer, the ring with $H_a$ , $H_b$ , and $H_c$ is xylyl ring while the other ring is terminal phenyl ring.....	23
Figure 1.16.	Two-ring microstates of the <b>C</b> , <b>F</b> , and <b>S</b> states.....	24
Figure 1.17.	Four microstates of the <b>S</b> state.....	25

Figure 1.18.	Simplification steps used in chemical shift calculations.....	27
Figure 1.19.	Mol fractions of four-state conformers ( <b>C</b> , <b>F</b> , <b>S<sub>ee</sub></b> , and <b>S<sub>ef</sub></b> ) as a function of the mol% DMSO-d <sub>6</sub> in D <sub>2</sub> O. Graphs for compounds <b>1a</b> , <b>2b</b> , and <b>2c</b> are shown from left to right.....	32
Figure 1.20.	Electrostatic effects between aromatic rings.....	34
Figure 1.21.	Complementary electrostatic interactions of <b>C</b> and <b>F</b> states.....	37
Figure 1.22.	Crystal structures of <b>1a</b> , <b>2b</b> , and <b>2c</b> .....	38
Figure 1.23.	Molecular structures and crystal structures of <b>1a</b> and <b>2e</b> .....	40
Figure 2.1.	Interaction between charges. Black circle represents anion.....	50
Figure 2.2.	C-H/ $\pi$ interaction.....	50
Figure 2.3.	Four structure types in the crystals of planar or near planar polynuclear aromatic hydrocarbons.....	52
Figure 2.4.	Polynuclear aromatic hydrocarbons with herringbone packing.....	52
Figure 2.5.	Cation- $\pi$ interaction.....	54
Figure 2.6.	Orientation of the distribution of electrostatic surface on benzene ring.....	54
Figure 2.7.	Examples of the packing patterns.....	56
Figure 2.8.	Packing pattern in KOXREU.....	61
Figure 2.9.	Packing pattern in BAXZOQ.....	61
Figure 2.10.	Packing pattern in COPDEQ.....	62
Figure 2.11.	Packing pattern in LIDYOM.....	62
Figure 2.12.	Packing pattern in PYRPIC03.....	64
Figure 2.13.	Packing pattern in BAXZOQ.....	65
Figure 2.14.	Crystals with <b>FF</b> cation-anion packing of one-ring cations.....	65
Figure 2.15.	Hydrogen-bond structures in JAVFUH and JAVFOB.....	67
Figure 2.16.	Packing pattern in BAYBEJ.....	72
Figure 2.17.	Three-ring cations .....	74

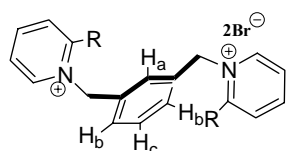
Figure 2.18.	One- and two-ring pyridinium derivatives with <b>FF</b> cation-anion packing style in their crystal structures.....	81
Figure 2.19.	<b>FF</b> and T-shape packing of benzene dimers.....	82
Figure 2.20.	Electrostatic model of pyridinium rings.....	83
Figure 2.21.	Orientation of the cationic rings.....	86
Figure 2.22.	Back-bonding interactions between two cationic- $\pi$ -systems.....	87
Figure 3.1.	The total-resonant-sextet (TRS) series and benzenoid polyradical series (triangulene type) benzenoid hydrocarbons.....	93
Figure 3.2.	Triangulene <b>3.2</b> and triangulene skeleton.....	93
Figure 3.3.	Derivatives of triangulene.....	94
Figure 3.4.	Electron reduction of trioxytriangulene <b>3.1</b> .....	94
Figure 3.5.	Delocalization of the charge by resonance of <b>3.4</b> , <b>3.5</b> , <b>3.6</b> , <b>A</b> , and <b>B</b> .....	96
Figure 3.6.	Triangulene type cations and anions.....	97
Figure 3.7.	Triazatrianguleniums, counterions and their corresponding code....	98
Figure 3.8.	Tripropyl- (top) and triethyl- (bottom) triangulene cations viewed from <i>a</i> axis (left) and their packing patterns.....	98
Figure 3.9.	Prediction of packing pattern of trimethyltriazatriangulenium in <b>3.4C</b> .....	100
Figure 3.10.	Salt tetrabutylammonium trioxytriangulene <b>3.1E</b> (left) and its crystals structure (right).....	101
Figure 3.11.	DSC spectra of tetrabutylammonium trioxytriangulene ( <b>3.1E</b> ), trimethyltriazatriangulenium hexafluorophosphate ( <b>3.4C</b> ), trimethyltriazatriangulenium tetrafluoroborate ( <b>3.5D</b> ), and tripropyltriazatriangulenium tetrafluoroborate ( <b>3.6D</b> ).....	102
Figure 3.12.	Triangulene anion, cation molecules and their corresponding codes for triangulene salt pairs study.....	103

Figure 3.13.	Crystal structures of tripropyltriazatriangulenium trioxytriangulene ( <b>3.16</b> ), tripropyltriazatriangulenium tetrafluoroborate ( <b>3.6D</b> ), and tetrabutylammonium trioxytriangulene ( <b>3.1E</b> ).....	104
Figure 3.14.	DSC spectra of tetrabutylammonium trioxytriangulene ( <b>3.1E</b> ), trimethyltriazatriangulenium trioxytriangulene ( <b>3.14</b> ), triethyltriazatriangulenium trioxytriangulene ( <b>3.15</b> ), and tripropyltriazatriangulenium trioxytriangulene ( <b>3.16</b> ).....	106
Figure 3.15.	Calculated molecular orbitals for the lowest unoccupied molecular orbital (LUMO) (a) of triazatriangulenium cation (b) and the highest occupied molecular orbital (HOMO) (d) of trioxytriangulene anion (c). The simplified packing patterns of salt pair <b>3.16</b> and the hypothesized optimum molecular alignment ( <b>FFCC</b> ) of salt pair <b>3.14</b> are also shown, (e) and (f). In (e) and (f), the dotted lines represent anions. The orientations of the LUMO of cation and the HOMO of anion in <b>FFCC</b> are shown in (g).....	111
Figure 5.1.	Synthesis of <b>2b</b> in two steps.....	119
Figure 5.2.	Synthesis of <b>2c</b> in two steps.....	120
Figure 5.3.	Synthesis of 2, 2'-bis-2-biphenyl- $\alpha, \alpha'$ -m-xylene ( <b>2e</b> ).....	120
Figure 5.4.	Synthesis of 2,2'-bis-2-methylphenyl- $\alpha, \alpha'$ -m-xylene ( <b>2f</b> ).....	121
Figure 5.5.	Synthesis of tetrabutylammonium 4,8-Dioxo-4H-8H-dibenzo[cd,mn]pyren-12-olate ( <b>3.1</b> ).....	122
Figure 5.6.	Synthesis of 4,8,12-Triethyl-4,8,12-triazatriangulenium tetrafluoroborate ( <b>3.5</b> ).....	124
Figure 5.7.	Synthesis of 4,8,12-Tri-n-propyl-4,8,12-triazatriangulenium 4,8-Dioxo-4H-8H-dibenzo[cd,mn]pyren-12-olate ( <b>3.16</b> ).....	127

## Chapter One

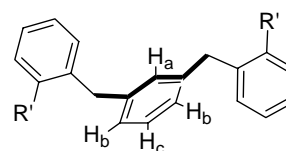
### Exploring conformational dynamics of $\pi$ system by NMR

Six compounds (**1a**, **1d**, **2b**, **2c**, **2e**, and **2f**) were used in the current study. They are shown in Figure 1.1. Two of them, **1a** and **1d**, were synthesized previously by former members of the Cammers group<sup>(1,2)</sup>. All others, **2b**, **2c**, **2e**, and **2f**, were synthesized during this research. Compounds **1a**, **2b**, **2c**, and the reference compound *N,N'*-[1,3-phenylenebis(methylene)]bis(2-phenylpyridinium) dibromide (**1d**) were used to probe the multi-state organic conformation in the solution. Conformational distributions of the probe molecules in different solvents and temperatures were quantitatively calculated using calculated chemical shift difference and experimental data from proton NMR studies. In this study, a general protocol for the application of magnetic anisotropy to quantitative multi-state conformational analysis of molecules undergoing fast conformational exchange was proposed. The mass balance was checked to inspect the reliability of this method of conformational analysis. Positive solutions for the equations under different conditions confirmed the reliability. VT-NMR was conducted to study the enthalpic parameters.



**1a**: R=phenyl, **2b**: R=2, 4, 6-trifluorophenyl;

**2c**: R=pentafluorophenyl; **1d**: R=methyl



**2e**: R'= phenyl, **2f**: R'=methyl

Figure 1.1 Charged compounds (**1a**, **2b**, **2c**, and **1d**) and neutral compounds (**2e-f**).

Also, 2,2'-biphenyl- $\alpha,\alpha'$ -*m*-xylylene (**2e**) was synthesized to study the charge effect on the packing of the  $\pi$  system. Solid-state structures of **1a**, **2b**, **2c**, and **2e** were studied. The dications, **1a**, **2b**, and **2c**, were packed intramolecularly face-to-face while the neutral compound **2e** had no intramolecular  $\pi$ -stacking. Apparently, charges are important in the formation of the conformations in this family of molecules.



In the sections that follow a brief primer is offered about the interatomic forces involved in  $\pi$ -stacking (sections **1.1-1.2**). Since this thesis is concerned with NMR conformational analysis, a very brief overview of some pertinent literature is offered (section **1.3**). This work focuses on the synthesis and study of **2b**, **2c**, **2e**, and **2f**. Conformational analysis of molecules **1a** and **1d** were reported prior to the current work by the Cammers group. In section **1.3.5** below the previous conformational analysis of the Cammers group is described. The last portion of the document describes the current solution phase conformational analysis of hydrocarbon and fluorocarbon **1a**, **2b**, **2c**, and **1d** collectively (section **1.4**). This contribution is novel because it is the only quantitative, four-state NMR analysis in the chemical literature in which the analysis is based solely on chemical shift due to aromatic anisotropy of conformers that exchange rapidly on the NMR timescale. Corroborative solid-state studies conclude this section.

After struggling to interpret the observations on an atomic level, it was realized that a neutral model was necessary. Molecules **2e** and **2f** were synthesized and studied (section **1.5**). This study led to the conclusion in the preceding paragraph. The possible involvement of charge-enhanced  $\pi$ -stacking and/or solvent-dependent ion pairing is discussed.

## 1.1 $\pi$ - $\pi$ interaction and $\pi$ -stacking

### 1.1.1 $\pi$ - $\pi$ interaction, weak force on the level of van der Waals attraction

The fact that there are attractive interactions between  $\pi$  systems ( $\pi$ - $\pi$  interaction) has been known for many years.  $\pi$ - $\pi$  interaction is one of the non-covalent intermolecular forces that are important for the stability of the proteins, DNA helical structure,<sup>(3,4)</sup> host-guest binding systems,<sup>(5-8)</sup> supramolecular self-assembly,<sup>(9,10)</sup> aggregation of porphyrin,<sup>(11-14)</sup> and the packing patterns in the crystal structures of aromatic molecules,<sup>(15)</sup> *etc.* Many papers have been published about  $\pi$ -stacking; however, there is still incomplete understanding of its origin. Quantitative measuring of  $\pi$ -stacking is challenging due to the weak nature of the  $\pi$ - $\pi$  interaction.

Benzene dimer has been used as the prototypical model for  $\pi$ - $\pi$  interactions.<sup>(15-20)</sup> Two proposed lowest energy conformers of benzene dimer are: face-to-face, edge-to-center packing (**FFEC**); and T-shape, edge-to-center (**EF**); as shown in Figure 1.2.<sup>(20)</sup> Among these, the **FFEC**-dimer is a stacked arrangement. The other stacked arrangement, which has been mentioned in many papers, is face-to-face, center-to-center (**FFCC**). **FFCC** has slightly higher energy than **FFEC**.

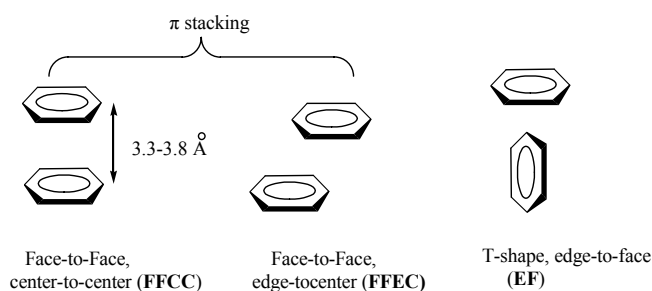


Figure 1.2. Some conformers of benzene dimer. **FFEC** and **EF** are the most stable dimers.

Many quantum methods have been used to calculate the  $\pi$ - $\pi$  interaction energy of benzene dimers. Different levels of theory showed different minima energy results. Most of them are between 2-3 kcal/mol,<sup>(16-21)</sup> which is on the level of van der Waals attraction. The calculation by Tsuzuki showed that the **FFEC** is the energy global

minimum with -2.48 kcal/mol with the center of the two benzene rings offset by 1.8 Å and vertically separated by 3.5 Å.<sup>(20)</sup> The energy of **EF** is higher by 0.02 kcal/mol, within calculational and experimental error. The **FFCC** has the highest energy (-1.48 kcal/mol) of the three due to the  $e^-/e^-$  repulsion (Figure 1.3). Simple neutral  $\pi$ -stacking is commonly referred to the non-covalent interaction between the approximately parallel stacks of neutral aromatic planes with  $\sim 3.3$ – $3.8$  Å interplanar distances,<sup>(15)</sup> basically the **FFCC** and **FFEC**  $\pi$ - $\pi$  interactions discussed above.

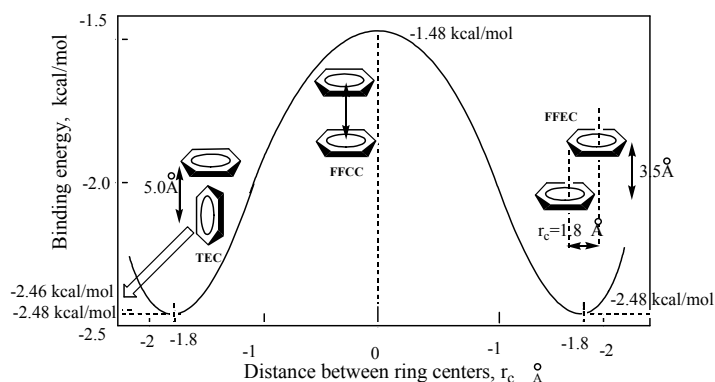


Figure 1.3. Calculated energy of **FFCC**, **FFEC**, and **EF**  $\pi$ - $\pi$  interactions.

Amino groups with aromatic rings are found in the DNA and protein structures. Most of these aromatic rings are involved in the  $\pi$ - $\pi$  interactions in native conformations of these biopolymers, through either **FFEC** or **EF** patterns. None of them have **FFCC** geometry.<sup>(22-24)</sup> Although  $\pi$ - $\pi$  interactions are weak, they are very important for protein structural stability.<sup>(3)</sup> The contributions of  $\pi$ - $\pi$  interactions to the stability of proteins or other organic compounds in solution have been investigated. The pair of Phe-Phe side chain contributed -0.55<sup>(25)</sup> kcal/mol in aqueous solution in the  $\beta$ -hairpin developed by Gellman,<sup>(26)</sup> while the average energy of the **EF** aromatic interaction in the zipper complex is -0.3 kcal/mol, which changed with the substitution groups on the rings (from 0.29 to -1.1 kcal/mol).<sup>(27)</sup> More recently, circular dichroism studies showed the stability energy of the Phe-Phe  $\pi$ - $\pi$  interaction in monomeric  $\alpha$  helices can get up to -0.8 kcal/mol.<sup>(28)</sup>

### 1.1.2 Simple $\pi$ -stacking

$\pi$ -stacking commonly refers to the non-covalent  $\pi$ - $\pi$  interaction between aromatic groups separated by  $\sim 3.3$ – $3.8$  Å interplanar distances,<sup>(15)</sup> basically the **EF**, **FFCC** and **FFEC**  $\pi$ - $\pi$  interactions discussed above. The possible molecular orbital interaction between stacked aromatic rings invoked great interest in the investigation of  $\pi$ -stacking.<sup>(29)</sup> Many papers have been published to investigate the  $\pi$ -stacking.<sup>(30-38)</sup> Many models have also been proposed to explain the stacking.

The packing of benzene and hexafluorobenzene is noteworthy because none of the  $\pi$ -stacking in proteins take the **FFCC** packing style.<sup>(22,23)</sup> In the mixed 1:1 benzene/hexafluorobenzene crystal, the benzene and hexafluorobenzene are packed alternately along the  $C_6$  axis of the benzene ring, using a nearly face-to-face, center-to-center (**FFCC**) packing pattern.<sup>(39)</sup> The physical properties of the benzene/hexafluorobenzene mixture are quite different from the pure benzene or hexafluorobenzene. The melting point of  $C_6F_6/C_6H_6$  is 24 °C, which is much greater than that of  $C_6F_6$  (4 °C) or  $C_6H_6$  (5 °C).<sup>(40)</sup> This means the interactions between  $C_6F_6/C_6H_6$  are much stronger than those between the pure  $C_6F_6$  or  $C_6H_6$ . The  $C_6F_6$  can be mixed and co-crystallized well with an equal amount of  $C_6H_6$  despite the fact that liquid perfluoroalkanes form separate phases with analogous hydrocarbons. The **FFCC** packing pattern is probably due to the large quadrupole moments with opposite signs between hexafluorobenzene and benzene,<sup>(39,41)</sup> which will be discussed later.

### 1.1.3 Canonical intramolecular interactions

Non-covalent interactions between molecules, which involve several forces, such as: Van de Waals interaction, hydrogen bonding, solvophobic effect, electrostatic interactions,  $\pi$ - $\pi$  interactions, are very important to the stability of the association inside the protein structures and drug design.<sup>(16)</sup> Some of the interactions are discussed as follows:

### **1.1.3.1 Van der Waals interaction**

Van der Waals interaction is an intermolecular attraction that involves the dispersion forces, dipole-induced dipole, and dipole-dipole attractions. The two important distance dependences are  $1/r^3$  and  $1/r^6$ . The dispersion force is a weak intermolecular force that arises from the attraction between transient dipole moments of molecules. Sometimes it is also called London dispersion forces. The dipole-dipole force is the attraction between molecules that have dipole moments. The van der Waals interaction is typically a weak interaction having a value of only a few kcal/mol. For example, the magnitude of the dispersion energy for two methane molecules separated by 0.3 nm is approximately 1.4 kcal/mol.<sup>(42)</sup>

### **1.1.3.2 Hydrogen bonding**

Typically this happens when the positively charged hydrogen atom connected to an atom of high electro-negativity, such as: oxygen and nitrogen atoms, comes close to another high electronegative atom. It's a strong interaction and sometimes can get 5-10% of the energy level of the covalent bond (e.g. the hydrogen bonding energy for water molecules is about 5.6 kcal/mol<sup>(43)</sup>).

### **1.1.3.3 Solvophobic effect**

The solvophobic effect happens when there is a large difference of polarity exists between solvent and solute. The solutes tend to aggregate instead of dissolving in the solvent. The hydrophobic effect is the solvophobic effect of the apolar solute in the aqueous media. The thermodynamic factors of the hydrophobic effect are complex. According to the traditional theory, for the small solute at low temperature (room temperature or below), the hydrophobic effect is entropically driven; the small solutes don't break the hydrogen bonding of the surface waters. Water tends to form cages around the apolar solute. The surface of the cage is more ordered than the bulk solution. When the solutes aggregate, the surface water is released into the bulk solution and the system is more chaotic (has larger entropy value).<sup>(29,52)</sup>

#### 1.1.3.4 Pauli repulsion

When two molecules get very close with each other, the electron clouds of each molecule start to overlap. There will be repulsion between the electron clouds. This is called Pauli repulsion which will be dominant when the molecules are closer than the van der Waals distance.<sup>(16)</sup>

#### 1.1.3.5 Charge transfer

A charge transfer or electron donor–acceptor effect is a kind of coulombic attractions that happens between two molecules which can form an excited charge-separated state when mixed together. Normally, this is a very small interaction.<sup>(44-47)</sup>

Except the hydrogen-bonding, all these non-covalent interactions are more or less involved in the  $\pi$ - $\pi$  interactions. Compared with the hydrogen-bonding, the  $\pi$ - $\pi$  interaction, which is the overall interaction of several non-covalent effects, is a kind of very weak force on the level of van der Waals attraction, most of which are between 2-3 kcal/mol.<sup>(16-20)</sup> Yet, it is important for the stability of bio-structures, such as proteins.

London dispersion interactions are considered to be the major contribution of the stabilization energy of  $\pi$ - $\pi$  interactions between aromatic rings while other components, such as quadrupole moment, electrostatic, Pauli exchange/repulsion interactions, determine the geometry of the  $\pi$ - $\pi$  interaction. In aqueous solution, the  $\pi$ - $\pi$  interaction is further affected by additional hydrophobic effects.<sup>(29)</sup> The surface overlaps of the aromatic systems are very important to the magnitude of London dispersions of  $\pi$ - $\pi$  interactions.

## 1.2 Models used to explain the $\pi$ - $\pi$ interactions

Many papers have been published discussing the molecular forces involved in  $\pi$ - $\pi$  interactions. Several hypotheses have been proposed, such as: solvophobic model, electron donor-acceptor or charge transfer model, quadrupole interaction model, atomic charge model, and electrostatic model.

### 1.2.1 Solvophobic model

Solvophobic model explained the  $\pi$ -stacking phenomenon in solution by favorable desolvation of aromatic groups. Different from the traditional theory, in which the hydrophobic effect is entropically driven, the benzene dimer and pyrene-cyclophane  $\pi$ - $\pi$  interactions showed large enthalpy changes.<sup>(48,49)</sup> Monte Carlo calculation showed that water structure near the surface of benzene dimer is only slightly perturbed by the presence of the benzene molecule.<sup>(50)</sup> Beveridge *et al.* showed that there are around 23 water molecules in the first solvation shell of benzene in water, two of them located above and below the center of the benzene ring, with the hydrogen atom extended into the  $\pi$  cloud.<sup>(51)</sup> Severance *et al.* calculated the minimum of free energy for the benzene dimer in different solvents. They found that the binding of the dimers was enhanced by solvent polarity. The free energy for benzene was -0.4, -1.0, and -1.5 kcal/mol in benzene, chloroform, and water solutions respectively.<sup>(52)</sup> Diederich *et al.* studied the inclusion complex of macrobicyclic cyclophane and pyrene in water and 17 other organic solvents. They found the stabilities of the complexes decreased with decreasing polarity of the solvents. The most stable form is in water. Because the complex used nearly the same geometry in these solvents, they suggest that these differences in binding strength results from solvation effects, which were driven by enthalpic change. For the large, nonpolar, planar solutes, the interactions between the solvents and solute surface are different from those between the bulk solvents. Polar solvents preferred to interact with the bulk more than with the apolar solute surface. When forming complexes, solvent molecules that interacted with the solute surface were released to the bulk solvents and enthalpy was

gained. For example, in water solution, water-water interactions inside the bulk solvent get more hydrogen bonds. Part of the hydrogen bonds of the water around the solute is broken by the planar aromatic solutes. When these water molecules are released from the solute surfaces to the bulk during the complexation step, enthalpy is minimized.<sup>(49-52)</sup> In polar solvents, the solvation was characterized by large enthalpy changes (for example, -20.0 kcal/mol in TFE solution).<sup>(49)</sup> This is different from the traditional hydrophobic effects.

### 1.2.2 Electron donor-acceptor or charge transfer model

The electron donor-acceptor or charge transfer models have been used for the molecular design of organic conductors.<sup>(53)</sup> Charge transfer happens when one molecule with low ionization potentials (IP) is packed close to the other molecule with high electron affinity (EA). In organic conductors, charge transfer can happen between electron donors and acceptors in conductive crystals lead to charge transfer complexes, in which donor and acceptor molecules can bring partial positive and negative charge. Studies of the guest-host complex between naphthalene with different types of electron withdrawing and/or electron donating groups and cyclophane host showed that these aromatic complexes were not solvophobically controlled, but basically electron donor-acceptor (EDA) interactions due to the similar behaviors of the complexes in methanol, water-methanol and DMSO solutions.<sup>(54)</sup> Similar models also have been used to explain the  $\pi$ - $\pi$  stacking phenomena in cyclophane-arene inclusion complex<sup>(55)</sup> and the complex between a pyrene-based tweezer molecule and macrocyclic ether-imide-sulfone molecule.<sup>(56)</sup> Calculation showed that interaction energy in an electron donor-acceptor (EDA) complex may include electrostatic interaction, charge-transfer interaction, polarization interaction, and dispersion energy.<sup>(55)</sup> Sanders showed that the EDA or charge transfer models are not good ones for the regular  $\pi$ - $\pi$  interaction, although these models can very well explain some specific cases of  $\pi$ - $\pi$  stacking.



### 1.2.3 Quadrupole interaction model

The nearly face-to-face, center-to-center (FFCC) packing of mixed 1:1 benzene/hexafluorobenzene crystals was explained by the quadrupole interaction model.<sup>(39,41)</sup> The quadrupole moment was used to measure the distribution of charge within a molecule, relative to a particular molecular axis. In benzene, due to the six C ( $\delta^-$ )-H ( $\delta^+$ ) bond dipoles and high degree of symmetry present in this molecule, this molecule can be treated as a charge-separated molecule with negative charges above and below the center of the benzene plane and the balancing positive charges surrounding the edge of ring. This would give the negative quadrupole moment along  $C_6$  axis of the benzene ring. As for hexafluorobenzene, it has six polar bonds C ( $\delta^-$ )-F ( $\delta^+$ ) with the opposite direction to those of benzene. So, the quadrupole moment of hexafluorobenzene is opposite to that of benzene,<sup>(39)</sup> as shown in Figure 1.4. The negative and positive quadrupole moment of benzene and hexafluorobenzene have been checked by experiment, as  $-29$  and  $31.7 \times 10^{-40} \text{Cm}^2$ .<sup>(58)</sup> The quadrupole moment of the trifluorobenzene (close to zero) confirmed the bond additivity character of this molecular property.<sup>(41,58)</sup> Quantum calculation showed that the electrostatic interactions provide less than  $\sim 15\%$  to the total van der Waals  $\pi$ - $\pi$  interactions. This is due to atomic interaction and related directly to the overlap areas.<sup>(59-61)</sup> The dispersive van der Waals attractions are the main energy sources for the typical  $\pi$ - $\pi$  interaction, while the electrostatic interactions related to quadrupole interactions determine the orientation of the stacking.<sup>(29)</sup>

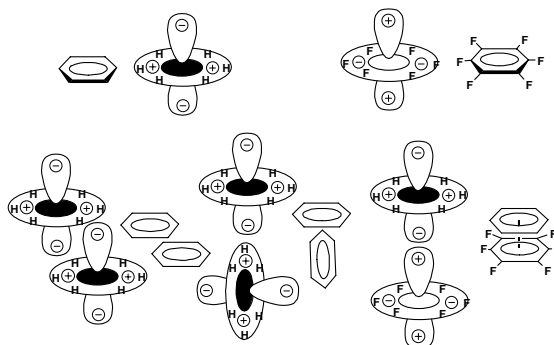


Figure 1.4. Quadrupole models of  $C_6F_6$  and  $C_6H_6$ .

### 1.2.4 Atomic charge model

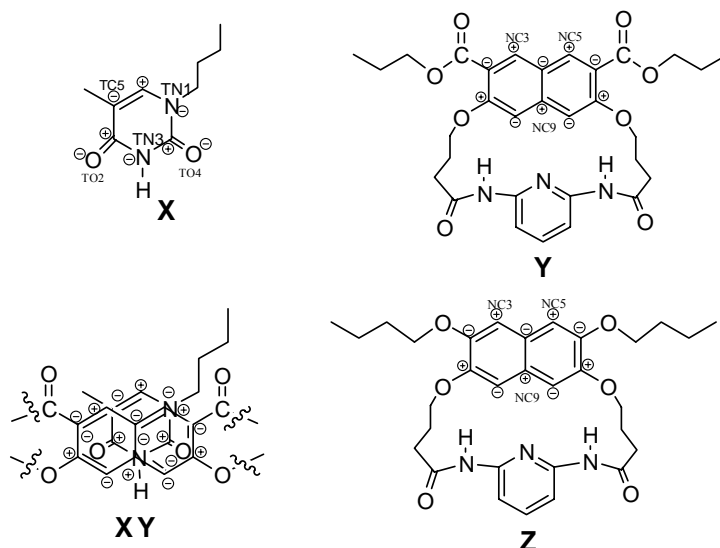


Figure 1.5. Atomic charge model.

Hamilton and co-workers found that diester macrocycle **Y** forms a strong complex with 1-butylthymine **X**,  $\Delta G^\circ = -3.75$  kcal/mol. The complex used **FFCC**  $\pi$ - $\pi$  stacking patterns in which naphthalene of **Y** is positioned directly above pyrimidine of **X** with a distance of 3.54 Å, but the packing pattern of compound **Z** with **X** is different. **Z** is the same as **Y**, except that the carboxyl groups of **Y** were replaced by butoxyl groups. The association energy is weaker,  $\Delta G^\circ = -2.92$  kcal/mol, and naphthalene of **Z** is almost perpendicular to the pyrimidine of **X** (**EF** packing pattern). Hamilton used the atomic charge model to explain the packing difference. In this model, the  $\pi$ - $\pi$  interaction comes from the uneven charge distribution of the  $\pi$  systems shown in Figure 1.5. Electrostatic complementarity between two rings is very important. If the partial charges on one ring can be aligned with the opposite charges of the other rings, strong face-to-face  $\pi$ - $\pi$  stacking will be formed. Otherwise, edge-to-face interaction will be preferred. As shown in Figure 1.5, in **XY** complex, NC2-TO2, NC4-TN1, NC5-TC5, NC7-TO4, NC9-TN3 are pairs of oppositely charged atoms on different rings, which can be packed exactly face-to-face with each other in the **FFEC** pattern. Changing the carboxyl groups of **Y** to

butoxyl groups will change the charge distribution pattern of the naphthalene ring which in turn will change the packing pattern of the complex **XZ**.<sup>(62)</sup>

### 1.2.5 Electrostatic model

Sanders and Hunter investigated the  $\pi$ - $\pi$  interaction between porphyrin molecules in solution and solid state by experiment and calculation. They showed that the  $\pi$  system can be viewed as a sandwich structure with positively charged  $\sigma$ -framework in the middle and two negatively charged  $\pi$ -electron clouds on the top and bottom of the ring. Each carbon atom in the  $\pi$ -system was treated as  $+1\delta$  charge at the nucleus center and two  $-\delta/2$  charges at a  $d$  distance, which was determined by the experimental quadrupole moment of benzene as shown in Figure 1.6.

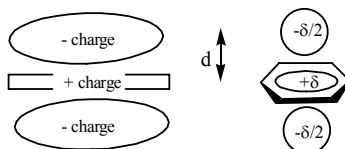


Figure 1.6 Electrostatic model of benzene ring.

The attraction of the  $\sigma$  backbone to the  $\pi$  electron determines the orientation of the stacking and the van der Waals attraction of the aromatic rings decided the magnitude of the interaction energy.

Using this model, they indicated that the  $\sigma$ - $\pi$  electrostatic effect is the major contribution to the  $\pi$ - $\pi$  stacking pattern, while the van der Waals interactions and solvophobic effects are minor ones. It is  $\sigma$ - $\pi$  not  $\pi$ - $\pi$  electrostatic effect that determines the  $\pi$ - $\pi$  stacking pattern<sup>(14)</sup> as shown in Figure 1.7.

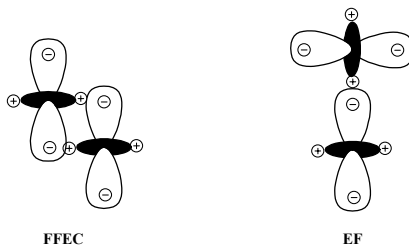


Figure 1.7 Electrostatic models for  $\pi$ - $\pi$  interaction.

The basic molecular forces that are involved in the typical  $\pi$ - $\pi$  stacking are: van der Waals, electrostatic, and/or quadrupole. These three forces contribute to the total energy of the  $\pi$ - $\pi$  interaction, with each having different contribution in different models.<sup>(14,63)</sup>

### 1.3 Exploring conformational dynamics of $\pi$ system by NMR

Conformational isomerism is important in the biomolecule studies. It is also useful in the drug development. Many spectroscopic techniques have been used in the conformational study of organic and biological molecules. Compared with others, NMR methods are more powerful. In NMR, coupling constants, integration, and NOE can be very useful. Analyzing these data can give incisive answers about the molecular conformation when, (1) the exchange of conformers (two or three) is slower than the NMR time scale, (2) there is only one stable conformer.<sup>(64)</sup> However, for those multi-state exchanges that are faster (e.g. on the NMR time scale), it will be difficult to determine quantitatively the conformational distributions.

In the current study, a hydrocarbon and two fluorocarbon derivatives of model molecules (**1a**, **2b**, and **2c**) together with a reference molecule (**1d**) have been synthesized to probe the rapid, multi-state organic conformation of  $\pi$  systems in solution. Compound **1a** and **1d** were first synthesized by former group members<sup>(2)</sup>. Chemical shift differences between model and reference molecules due to the influence of diamagnetic anisotropy of aromatic groups were calculated. Experimental data of proton NMR studies were also collected. A general protocol using these data to quantitative analyze multi-state conformational of molecules undergoing fast conformational exchange was proposed

#### 1.3.1 Chemical shift and shielding

A nucleus carries charge. When it spins, it can possess a magnetic moment along the spinning axis, Figure 1.8. The orientation of this microscopic magnetic moment will be separated into different energy levels when the nucleus is placed in a uniform magnetic field. The total number of the orientation is determined by  $2I + 1$ , where  $I$  is the

spin number, the intrinsic property of a nucleus. Nuclear magnetic resonance or NMR happens when the nuclei of some atoms are put in a static magnetic field and exposed to a second electromagnetic radiation in the radio frequency.

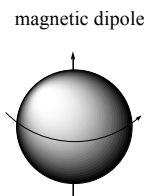


Figure 1.8. Magnetic dipole generated by nuclei spins on the nuclear axis.

For hydrogen atom, the value of  $I$  is  $1/2$ . There are two different spin directions of the protons,  $+1/2$  and  $-1/2$ . The energy of protons with different spin directions will be different as shown in Figure 1.9. The  $N_\beta$  and  $N_\alpha$  are the numbers of the protons in each level.  $N_\beta > N_\alpha$  according to Boltzmann distribution. The energy difference of these two spin directions is based on the Equation 1.1.

$$\Delta E = \frac{h\gamma}{2\pi} B_0$$

Equation 1.1. Energy difference of protons in magnetic field.  $h$  is Planck constant,  $\gamma$  is magnetogyric ratio, an intrinsic nuclear constant.  $B_0$  is strength of the magnetic field.

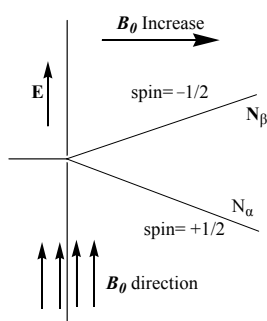


Figure 1.9. Energy difference of proton in a magnetic field  $B_0$ .

Under a certain magnetic field strength  $B_0$ , when the introduced radiofrequency satisfied Equation 1.1, the proton will absorb the energy, which results in a spectrum, nuclear magnetic resonance spectrometry.

According to Equation 1.1, an isolated proton can only absorb certain energy of radiofrequency under certain  $B_0$  and give out only one peak, chemical shift, in NMR. Fortunately, there exists the shielding and deshielding in the real world. These effects apply a small magnetic field to the protons, same as (deshielding) or against (shielding) the stationary magnetic field. The direction and magnitude depend on the different chemical environments of the protons. The real magnetic field strength applied to the protons should be modified by a shielding constant in Equation 1.1, as shown in Equation 1.2, where  $\sigma$  is the shielding constant.

$$\Delta E = \frac{h\gamma}{2\pi} B_0 (1 - \sigma)$$

Equation 1.2. Different energy differences of different protons in magnetic field.

The shielding or deshielding effect creates differences in the absorption energy and makes different chemical shifts for different protons. In a molecule, a proton is always shielded by an electron cloud. The density of the electron cloud varies with different chemical environments, which confers various chemical shifts to the different protons.

### 1.3.2 Ring current effects in benzene

For benzene ring protons, there is another kind of shielding or deshielding called the “ring current” effect, which exerts a large deshielding effect on the benzene ring protons. Figure 1.10 shows the effect.

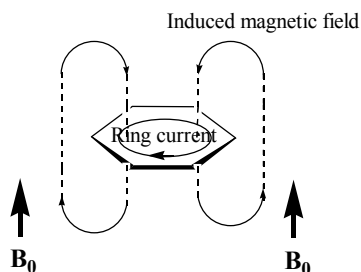


Figure 1.10. “Ring current” effect.

When the ring is perpendicular to the applied field  $B_0$ , circulation of valence electrons will be induced by the applied field. This induced circulation of valence electrons generates a magnetic field that opposes the applied field above and below the ring.

The ring current effect of benzene is directly connected with the different position of the proton to the ring. There is a connection between the chemical shift differences (between model and reference molecules) and the proton position to the ring. The change of proton chemical shift reflects the change of proton position.

### 1.3.3 NMR shielding can be accurately calculated

$^1\text{H}$  NMR shielding differences between model and reference molecules, due to diamagnetic anisotropy of aromatic groups, can be accurately calculated. Density functional theory at the level of B3LYP/6-311+G (2d, p) was considered to be the best one.<sup>(81)</sup>

This is a relatively new fact. This was not the case when Karabatsos made the following statement in 1970:

*“Since the chemical shift of  $H_a$  in the various conformations is neither known nor even understood very well as yet, [the changes in the chemical shift of  $H_a$ ] cannot presently be used for quantitative conformational analysis . . .”*<sup>(65)</sup>

Karabatsos went on to say that for the reason above, coupling is more important than chemical shift in conformational analysis.<sup>(65)</sup>

Analyzing coupling constants can sometimes give quantitative results of the multi-state, conformational distributions for appropriate structures as shown in Figure 1.11.<sup>(66-68)</sup> For example, Cimino applied the coupling-based conformational analysis to characterize multiple conformer equilibria of sapinofuranone A.<sup>(66)</sup> *Ab initio* quantum mechanics and vicinal H-H NMR couplings were used by Kent to investigate conformational equilibria of butanedinitrile due to solvent effects.<sup>(67)</sup> Belostotskii used *ab initio* and molecular mechanics calculations to calculate the J coupling of the alkyl- and Ph-substituted 3-piperideines to qualitatively estimate the conformation of these

compounds.<sup>(68)</sup> However, chemical shift differences due to the coupling and the aromatic diamagnetic anisotropy<sup>(69)</sup> are often used for the qualitative studies of the conformational changes.<sup>(70-80)</sup>

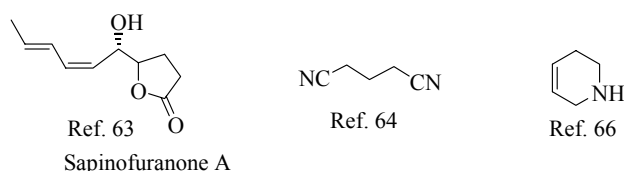


Figure 1.11. Models for *J*-coupling calculations.

### 1.3.4 Conformation changes NMR spectrum

Proton chemical shifts are closely related to the different chemical environments of the protons. Any change that results in the changing of the proton's environment will change the NMR chemical shift. Solvent,<sup>(82)</sup> temperature, or specific molecular associations<sup>(83)</sup> can change conformation. The changing of the conformation will cause the different shielding or deshielding effects to the protons, and change the NMR spectrum. If we accept the facts above, NMR calculation and real spectra could be used to quantitatively determine conformational states of molecules in solution.

### 1.3.5 Models of $\pi$ system for quantification of conformations in solution state

Many minimal models have been built to investigate the conformation isomerism of  $\pi$  systems in solution state by the NMR method and tried to explain the origins of the isomerism, which will be useful in the study of biological molecules and drugs development.<sup>(84-89,1,2)</sup> All these models can be separated into different groups according to the total isomerism that is described.



### 1.3.5.1 Two-state models

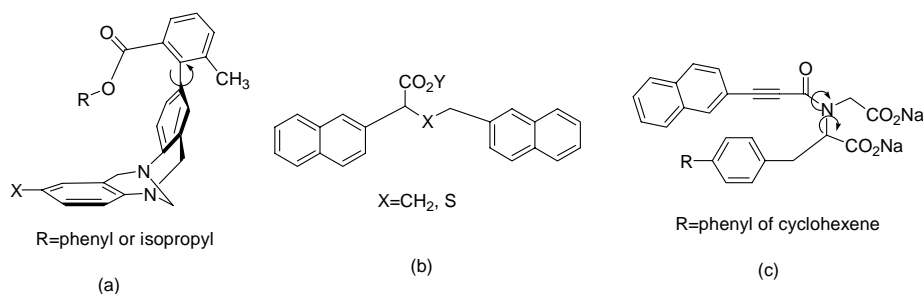


Figure 1.12 Two-state systems.

Wilcox used a series of the derivatives of *N,N* disubstituted benzodiazepine, model **a** in Figure 1.12, to investigate the origins of the preference for edge-to-face folding of **a** in the solid state. They found that compound **a** had two folding states in  $\text{CDCl}_3$ , which can be quantified by NMR. There was about 0.5 and 0.3 kcal/mol energy difference between the two states of the isopropyl esters and phenyl esters for all substituents. The insignificant difference in substituent effect questions the theory that the orientation of solid state is dominated by electrostatic forces. They concluded that London dispersion forces between aryl groups are the driving force.<sup>(85,86)</sup>

Compounds of **b** models were studied by the Gellman group through NMR and XRD. The dinaphthyl compounds, which showed edge-to-face in solid state, were compared with the mononaphthyl carboxylates for the upfield shifts in the aromatic region in aqueous,  $\text{CDCl}_3$ , and  $\text{C}_6\text{D}_6$  solutions. Due to the similarity of the di- and mononaphthyl carboxylates in the NMR upfield area, they concluded that the upfield shifts are due to random conformational motion instead of the hydrophobic collapse.<sup>(87)</sup>

Another minimal model, compound **c**, was also studied by the Gellman group. The tertiary amide provides slow rotation for NMR observation. Effects of different substitution groups were compared through NMR studies on the Gibbs free energy needed for the transformation from E state to Z state. In E state, the phenyl group is at the

same side as the naphthyl group to form naphthyl-aryl clustering, while in Z state, these two groups are on different sides. The result showed that the preference of the clustering in phenyl over cyclohexyl substitution was due to the intrinsic affinity of aromatic groups.<sup>(88)</sup>

All these models are two-state systems. Most of them are hindered systems of large energy difference between two conformations; this decelerated the exchange rate to the NMR scale and separated the system into two states. Only folded versus non-folded states are defined by these systems. Gradual changes of the models in solvent are needed for clear description of the interactions behind the affinity of the  $\pi$  system and the causes of the isomerism. These models can provide more information of the  $\pi$ - $\pi$  interactions in the  $\pi$  systems which will be helpful in interpretation of the  $\pi$ - $\pi$  interactions.

### 1.3.5.2 Three-state model of previous work of the Cammers group

Before I started this project, Cammers *et. al.* had demonstrated workability of the concept that calculated NMR spectra can be used to describe the conformational distribution of a molecule.<sup>(1,2,89,90)</sup> In this previous work, the Cammers group synthesized compounds **1a** and **1d**. Compound **1d** was used to correct for the effect of solvent on the chemical shift of **1a**. After correction, the resultant difference in chemical shift between **1a** and **1d** could be assumed to be due to the effect of conformational difference only.

The three-state model developed by the Cammers group<sup>(1,2)</sup> provides much conformational information that can be described by NMR chemical shifts. The methylene tethers between the central phenyl ring and the phenylpyridine moieties allow the two phenyl rings on the end to move easily above and below the central m-xylylene ring. This easy motion results in the dynamic exchange of the different conformations, which are very sensitive to perturbations by the surrounding solvent, in NMR time scale.

In compound **1a** the chemical shifts of the protons H<sub>a</sub>, H<sub>b</sub>, and H<sub>c</sub> are different. This difference is due to the 1,3-disubstitution of the xylyl ring and the ring current effect of the phenyl rings. Proton H<sub>a</sub> is the most sensitive to conformational changes among the

three. The unique chemical shifts of these protons can provide much information about molecular conformations, which will make quantification of conformational changes by means of  $^1\text{H}$  NMR possible.

Unfortunately, the  $^1\text{H}$  NMR spectrum cannot provide enough information for the simultaneous analysis of all three rings in the structure. In its previous work, the Cammers group made the simplifying realization that the conformation of **1a** is composed of two half-structures through  $C_s$  symmetry and that, because of this, the entire three-ring system could be treated as the sum of two half-structures of two-ring systems. This simplifies the analysis considerably.

In the previous studies of the Cammers group, a three-state model was applied to describe the conformational behavior of **1a** through the conformational search of the Monte Carlo program. In the three-state model, two phenyl rings on the ends of the molecule occupy three different spaces of the central phenyl ring: front (cluster, **C**), top (face-to-face, **F**) or back (splayed, **S**)<sup>(1)</sup>. **C** and **F** are stacked conformers that include interaction between three phenyl rings. Some examples are shown in Figure 1.13, in which conformations of three-ring systems are shown as combinations of two two-ring systems.

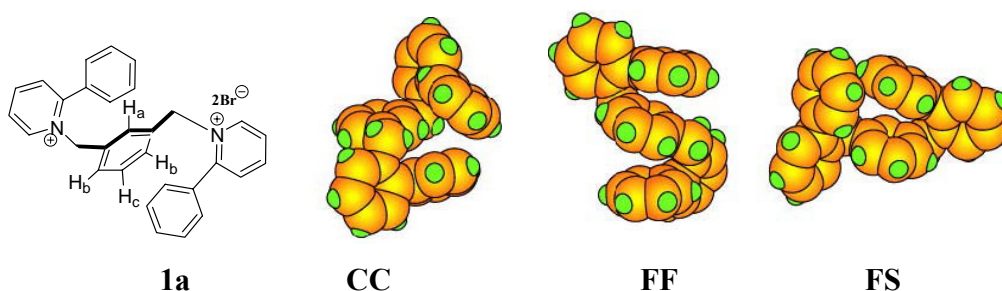


Figure 1.13. Model **1a** and some three-ring system conformations from conformational search in previous study of the Cammers group.

The Cammers group previously calculated the shielding differences between the three symmetry-unrelated protons of **1a** ( $H_a$ ,  $H_b$ , and  $H_c$  on the central phenyl ring) and those of **1d** due to the diamagnetic anisotropy of the terminal phenyl rings by means of

density functional theory (see Figure 1.13). These differences in calculated values for chemical shifts in **1a** versus **1d** in **C**, **F**, and **S** states were used in three equations to calculate the distribution of these states for molecule **1a**. The equations include the experimental chemical-shift differences of  $H_a$  and  $H_b$  between the molecules of **1a** and **1d**.

In the studies described above, *ab initio* calculations of chemical shifts, modeling, and NMR experiments were used together to provide a way to calculate the relative conformational populations from NMR data. This combination of techniques was used to calculate the distribution of the three states of the molecule **1a** in solution. Molecule **1a** was perturbed in aqueous solution with low concentrations of fluoroalkanol and alkanol cosolvents to study the solvent effects on  $\pi$ -stacking. Variable temperature (VT) NMR was also conducted to calculate the entropic and enthalpic contributions to conformational stability. Solvent accessible surface areas (**SASA**) of different conformers were calculated to explore the different exposure to bulk solvent of the hydrogen atoms on the carbohydrate model in different conformers. The results were used to understand hydrophobic effects on  $\pi$ -stacking.

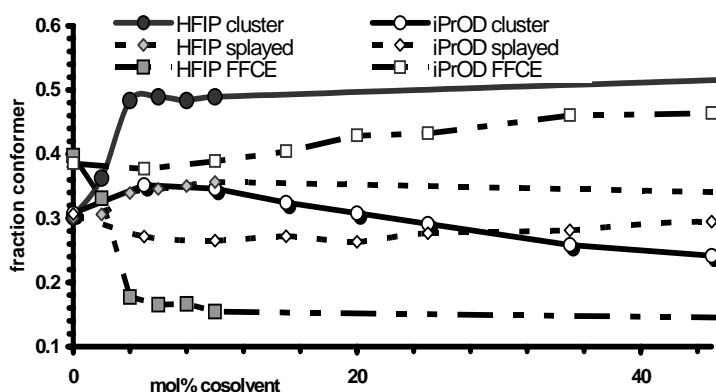


Figure 1.14 Examples of perturbation of **1a** in aqueous solution with fluoroalkanol and alkanol cosolvents in previous study of the Cammers group.

The results of the Cammers group study in Figure 1.14 showed that the conformer (**C**), which has the least hydrogen atom **SASA**, was most stable when

fluoroalkanol was used as cosolvent; the conformer (**F**), which has the most hydrogen atom **SASA**, turned out to be most stable while alkanol was cosolvent. The thermodynamic results showed that the free energy change of **F** state ( $\Delta G_F$ ) from alkanol to fluoroalkanol was most dramatic. This free energy change was determined by the enthalpy change ( $\Delta H_F$ ) of the **F**-conformer.

The following conclusions were drawn from the Cammers group's studies<sup>(1,2)</sup>:

- 1) The dication folding of aromatic compound **1a** is due to  $\pi$ -stacking interactions of the phenyl rings and the xylyl ring, which will be largely perturbed by the fluoroalkanol cosolvents. The **C** conformer is more favorable in the fluoroalkanol perturbation than the **F** conformer, while the **F** is more favorable in alkanol cosolvents. This is because the **C** conformer has smaller **SASA** and hides more hydrogen atoms from the less enthalpy favorable C-H bond C-F bond interaction.
- 2) The large enthalpy change ( $\Delta H_F$ ) of **1a** from alkanol to fluoroalkanol can be explained as follows. In the case of the fluoroalkanol solvent, the C-H bonds of the solute interact only weakly with the C-F bonds of the solvent. This is due to the nonpolarized state of the C-F bonds. In the case of the alkanol solvent, the C-H bonds of the solute interact favorably with the C-H bonds of the solvent, because the C-H bonds are relatively polarized.

#### 1.4 Quantitative four-state conformational analysis

Compounds **1a** and **1d** were used in previous research, described above, in which *ab initio* calculations, molecular modeling and NMR experiments were used together to quantify multi-conformer, fast exchange in solution.<sup>(1,2)</sup> My project was to inspect the reliability of this method and challenge the previous conclusions. For my study, compounds **2b** and **2c** were synthesized. Differences in the values of chemical shifts of **1a**, **2b**, and **2c** versus **1d** were calculated. Experimental data of proton NMR

studies were also collected. These data were combined to quantify the conformational distributions in different solvent for compounds **1a** through **2c**. VT-NMR was also conducted to acquire thermodynamic parameters to study the solvent effect on the conformational change. The corresponding neutral 2,2'-biphenyl- $\alpha,\alpha'$ -*m*-xylylene (**2e**) was also synthesized to probe the charge effect on the packing of the  $\pi$  system.

#### 1.4.1 Conformational search

The conformational search of minimal conformational models (**1a**, **2b**, and **2c**) for multiple state analysis were conducted with Monte Carlo conformational searching in MacroModel 8.1 program using the AMBER\* force field and the  $\text{CHCl}_3$  as GB/SA solvent.<sup>(91,92)</sup> Microstates with minimal structural and energetic differences were grouped into macrostates. In former studies, the conformers that were produced were grouped into three macrostates, **C** (cluster), **F** (face-to-face) and **S** (splayed), which are shown in Figure 1.15. Conformers **C** and **F** are stacked conformations because the phenyl rings interact with the xylyl ring. The **S** conformers are unstacked because the dissociation of all aromatic carbon rings. In current study, **C** and **F** states were defined similarly as the previous ones. However, two **S** states were found to be not at the same energy level due to fluorine substitution. So, four states instead of three states were defined in the current study. They are **C** (cluster), **F** (face-to-face), **See** (splayed, edge-to-edge), and **SeF** (splayed, edge-to-face).

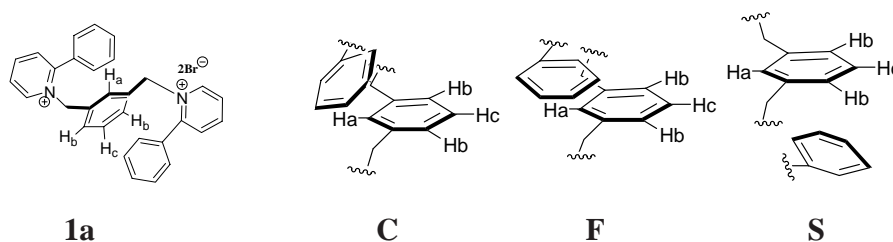


Figure 1.15. **C**, **F**, and **S** conformers of **1a**, **2b**, and **2c**, the  $\text{H}_a$ ,  $\text{H}_b$ , and  $\text{H}_c$  are shown in **1a**. Only two rings are shown, the pyridine rings, H and/or F atoms are omitted for clarity. In each conformer, the ring with  $\text{H}_a$ ,  $\text{H}_b$ , and  $\text{H}_c$  is xylyl ring while the other ring is terminal phenyl ring.

**C** state is the simplest case in molecules **1a**, **2b**, and **2c**. There is only one single conformer of **C** state for each model, as shown in Figure 1.16. When both phenyl rings are in the **C** state, the three aromatic rings of **1a**, **2b**, and **2c** will contact. In this model, both of the phenyl rings will be in front of  $H_a$  (Figure 1.16). Thus, three all-carbon rings are clustered together. In **C** state, the chemical shift value of the proton  $H_a$  is more upfield than that of the  $H_b$ , since  $H_a$  is almost on top of the phenyl rings.

In **F** states, the phenyl rings are on the top and below the xylyl ring. Both phenyl rings can interact with the xylyl ring, but they do not contact with each other. Due to the mobility of the phenyl rings, three conformational microstates were used to define the **F** state. In two of these, the phenyl rings in **1a**, **2b**, and **2c** were on top of  $H_a$  and  $H_b$  (Figure 1.16), respectively. For the third microstate, the phenyl rings were in front of  $H_b$ . However, in the conformer **F**, the three aromatic rings will not contact together. These three microstates have similar energies according to the molecular modeling. They will have similar behaviors. The chemical shift values of **F** state in **1a**, **2b**, and **2c** should be the average of that of these three states.

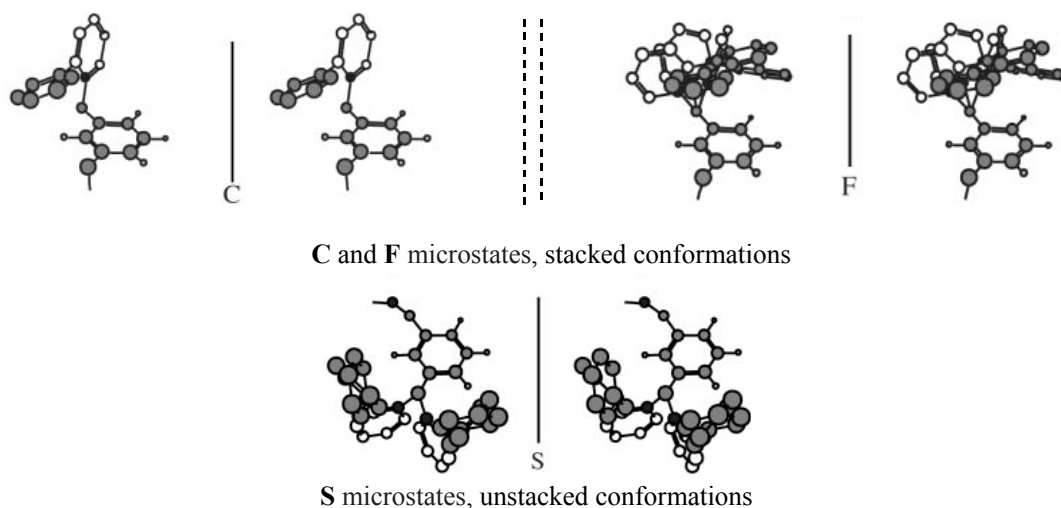


Figure 1.16. Two-ring microstates of the **C**, **F**, and **S** states.

The difference of the current study with the previous one is that two **S** states were found to be not at the same energy level. When the phenyl rings of **1a**, **2b**, and **2c** are on the different sides of the xylyl ring, facing  $H_a$  or  $H_b$ , the energies of these two **S** microstates should be different (**1S** and **2S**). In each of these two states, there exist two conformational microstates due to the different orientations of the phenyl rings to the xylyl rings (**1See-2Sef** in Figure 1.17). In the **See** states, the phenyl rings and the xylyl rings are packed edge-to-edge. While in the **Sef** states, the phenyls pack face-to-edge with the xylyls. Because the energy difference in the **EE** and **EF** packing patterns, **See** and **Sef** states should not be at the same energy level.<sup>(93)</sup> Thus, four chemical shifts value of these microstates need to be averaged to calculate the chemical shifts of **S** state. Another thing need to be careful about is that the microstates of **S** of **1a**, **2b**, and **2c** are not identical because the size of the fluorine atom is different to that of the hydrogen atom. Because the fluorine atom is much larger, in microstates **1See** and **2See**, when the hydrogen atoms on the phenyl ring are substituted by fluorine atoms,  $H_a$  and  $H_b$  will be in the van der Waals radius of one fluorine atom in molecules **2b** and **2c** due to the difference in the C-F and C-H bond length. The dihedral angle of the biphenyl need to be changed to removed these steric interactions.

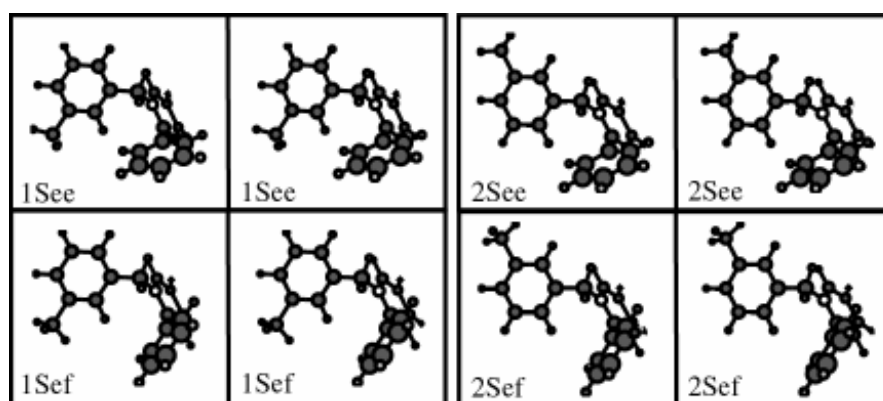


Figure 1.17. Four microstates of the **S** state.



### 1.4.2 Calculation of chemical shift differences of **1a**, **2b**, and **2c** versus **1d** in four states

Table 1.1. Chemical shifts differences of **1a**, **2b**, and **2c** versus **1d**. Values are in ppm. Values marked with an asterisk (\*) were substituted by 0 due to overestimation in gas-phase calculation. In the first column, *ala* is the proton H<sub>a</sub> of the molecule **1a** (shown in italic).

	C	F	See	Sef
<i>ala</i>	1.7	0.52	-1.61	0.14
<i>b1a</i>	0.19	1.26	-0.67	0.22
<i>c1a</i>	0.07	0.4	0.27	0.25 (0)*
<i>a2b</i>	1.49	0.39	-0.55	0.16
<i>b2b</i>	0.11	1.03	-0.17	0.2
<i>c2b</i>	0.05	0.25	0.1	0.17 (0)*
<i>a2c</i>	1.52	0.36	-0.97	0.2
<i>b2c</i>	0.07	0.97	-0.39	0.21
<i>c2c</i>	0.03	0.3	0.09	0.20 (0)*

The chemical shift difference of H<sub>a</sub>, H<sub>b</sub>, and H<sub>c</sub> between the molecules (**1a**, **2b**, and **2c**) and the reference molecule (**1d**) are caused by the different diamagnetic anisotropy effect of phenyl rings in **1a**, **2b**, **2c**, and **1d**. To each proton, these differences are the total effects of the conformer contributions (C, F, S states), which are the average effect of all the microstates. The magnetic contributions of conformers (C, F, S states) to the difference in the chemical shifts of molecules (**1a**, **2b**, and **2c**) versus reference molecule (**1d**) are shown in Table 1.1. In Table 1.1, the first column represents the different protons from different models. The first character represents the protons H<sub>a</sub>, H<sub>b</sub>, and H<sub>c</sub>, while the numbers and the second characters represent the model molecules (**1a**, **2b**, and **2c**), such as *ala* represents the protons H<sub>a</sub> from molecule **1a**. The first row represents different states.

The constants that appear in Table 1.1 were the contributions of conformers in each state to the difference in the chemical shifts of **1a**, **2b**, and **2c** versus **1d**. These values were the averages of all their microstate contributions. Calculations of each microstate was conducted with Gaussian98<sup>TM</sup> in rb3lyp/6-311++g(2d,2p) level, the ‘keyword’ is NMR.<sup>(81)</sup> Because accurate calculations need a lot of time, molecules **1a**, **2b**, **2c**, and **1d** were simplified as shown in Figure 1.18 to minimize the calculations.

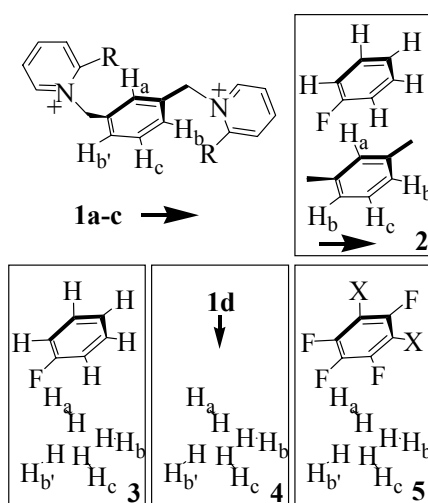


Figure 1.18. Simplification steps used in chemical shift calculations.

**2**, **3**, and **4** in Figure 1.18 show a calculation example of one of the microstate chemical-shift-difference constant for  $H_a$  (C state is shown as an example in the figure) in molecule **1a**. To calculate each microstate included in the C, F, and S states, the molecular structures of **1a**, **2b**, **2c**, and **1d** are simplified in four steps, (1) All rings were deleted except one phenyl and one xylyl ring; (2) The pyridinium ring was substituted with a fluorine atom (**2** in Figure 1.18); (3) Substituted carbon atoms in the xylyl ring were deleted; (4) The other xylyl carbon atoms were replaced with hydrogen atoms (**3** in Figure 1.18). During the simplification process, the relative positions of all atoms were not changed. The shielding of  $H_a$  in **1d** was simplified as in **4**. The calculated shielding of  $H_a$  in **4** minus that of  $H_a$  in **3** was used as one of the microstate chemical shift differences in *Cal<sub>a</sub>*, *Fal<sub>a</sub>*, or *Sal<sub>a</sub>*, according to the spatial arrangement of the model corresponding

to the **C**, **F**, or **S** state. Structure **5** in Figure 1.18 ( $X = \text{H}$  and  $\text{F}$ ) was used to calculate the chemical-shift differences for the microstates of models **2b** and **2c**. Simplification of the structures used in chemical shift calculations greatly shorten the calculation time. However, the results of the calculations were similar.<sup>(2)</sup>

Microstate values needed to be averaged to represent the corresponding magnetic contributions of each conformational state in Table 1.1. The chemical shift of the averaged structure will not be necessarily the same as the averaged chemical shifts. Due to the non-linear relationship between proton positions to the ring and the proton chemical shifts, structures cannot be averaged to simplify the calculations of the chemical shifts. The chemical shifts of each microstate need to be calculated. After all the microstate values have been acquired, these values can be averaged to get the chemical shift constant for each macrostate. Coefficients for **F** and **S** were the averages of the coefficients of all their microstates. Since there is only one microstate for **C**, the value is used directly.

In Table 1.1, the coefficients for  $\delta_{\text{Hc}}$  of the **SeF** states in **1a**, **2b**, and **2c** were set to zero. This is because the chemical shift calculations were conducted in the gas-phase condition. However, in the solution-state, the solvent effect is not negligible when the observed proton is more than 6 Å from the shielding cone of the aromatic ring. Solvent molecules will occupied the space between them and shield the observed protons from magnetic anisotropy of the aromatic ring. Under the gas-phase condition, there is no solvent effect. The gas-phase calculations overestimated the solution-phase shielding of magnetic anisotropy. If the distance between the proton and the aromatic ring is greater than 6 Å, it will be too far away for the aromatic ring to produce an observable ring current effect, the shielding effects from aromatic ring are negligible.<sup>(93,94)</sup>

Since there are two  $\text{H}_b$  protons in the probe molecules, **1a**, **2b**, and **2c**, the calculations of the chemical-shift coefficients for  $\text{H}_b$  were different from those of  $\text{H}_a$  and  $\text{H}_c$ . The values of  $\text{H}_a$  and  $\text{H}_c$  in Table 1.1 represent the magnetic anisotropy effect of only

one phenyl ring because the two phenyl groups have the same effect on these protons. However, for the protons H<sub>b</sub> and H<sub>b</sub>' (**3** in Figure 1.18), the shielding effects produced by the phenyl rings were different. The values of H<sub>b</sub> in Table 1.1, coefficients C<sub>bm</sub>, F<sub>bm</sub> and S<sub>bm</sub> for m = **1a**, **2b**, and **2c**, represent sums of the magnetic effects on H<sub>b</sub> and H<sub>b</sub>'.

#### 1.4.3 Calculation of conformational distributions of **1a**, **2b**, and **2c**

The coefficients acquired from the quantum calculation (Table 1.1) were used in Equations (1) to (4) to calculate the conformational distributions of **1a**, **2b**, and **2c** in solution states.

$$\mathbf{X}_{Cm} + \mathbf{X}_{Fm} + \mathbf{X}_{Sm} = 1 \quad (1)$$

$$\delta_{1dH_a} - \delta_{mH_a} = 2C_{am}\mathbf{X}_{Cm} + 2F_{am}\mathbf{X}_{Fm} + 2S_{eem}\mathbf{X}_{Seem} + 2S_{efm}\mathbf{X}_{Sefm} \quad (2)$$

$$\delta_{1dH_b} - \delta_{mH_b} = C_{bm}\mathbf{X}_{Cm} + F_{bm}\mathbf{X}_{Fm} + S_{eem}\mathbf{X}_{Seem} + S_{efm}\mathbf{X}_{Sefm} \quad (3)$$

$$\delta_{1dH_c} - \delta_{mH_c} = 2C_{cm}\mathbf{X}_{Cm} + 2F_{cm}\mathbf{X}_{Fm} + 2S_{eem}\mathbf{X}_{Seem} + 2S_{efm}\mathbf{X}_{Sefm} \quad (4)$$

Equation (1) is mass balance which requires that the sum of all mol fractions should be 100%. Equation (2) expresses that the chemical-shift differences of H<sub>a</sub> between molecules **1a**, **2b**, and **2c** versus **1d** are the sum of contributions of the four states. Equation (3) and (4) describe that of the H<sub>b</sub> and H<sub>c</sub>. In Equation (2), X<sub>Fm</sub> is the mol fraction of F state in molecule m (m = **1a**, **2b**, or **2c**) (for two-ring system, one phenyl and one xylyl ring). The coefficient F<sub>am</sub> in Equation (2) is the contribution of conformer F (see Table 1.1) to the difference in the chemical shifts of H<sub>a</sub> in molecule m (m = **1a**, **2b**, or **2c**) versus **1d**. Other terms in Equations (2)-(4) have similar meanings.

Equations (2) and (4) are different from Equation (3). The coefficients of the (2) and (4) are multiplied by two whereas (3) is not. This is because coefficients C<sub>bm</sub>, F<sub>bm</sub> and S<sub>bm</sub> for m = **1a**, **2b**, and **2c** were sums of different magnetic effects on H<sub>b</sub> from two phenyl rings, while the values of H<sub>a</sub> and H<sub>c</sub> in Table 1.1 represent the magnetic anisotropy effect from only one phenyl ring.

## 1.4.4 Results and discussions

### 1.4.4.1 Reliability of coefficients for the equations

The reliability of coefficients for the equation was checked.

First, the system of Equations (1)-(4) has four equations for four unknowns. Mathematically, this system allowed negative answers (mol fractions). However, chemically, negative mol fractions make no sense. Moreover, conformational analysis using the same system for a series compounds, **1a**, **2b**, and **2c**, is more sophisticated than the analysis of single compound alone (**1a**).<sup>(1,2)</sup> In the current study, all the answers of the mol fractions for compounds, **1a**, **2b**, and **2c**, under very different conditions (solvent and temperature) were positive. This confirmed that the conformational analysis system we used and the coefficients for the equation (Table 1.1) were reliable. This reasonable analysis was based on the inclusion of all possible conformational microstates and a good reference. Negative mol fractions were obtained when some of the microstates were deliberately omitted.

Second, the mass balance in Equation (1) stipulates that the sum of all mol fractions should be 100%. The reliability of the coefficients was also checked without enforced mass balance. Without mass balance, a system of three equations for three unknown was tried. The three equations were similar to Equations (2)-(4). The same coefficients for the **C** and **F** states were used. The only difference was that the original **S**-state expressions ( $\mathbf{See}_m \mathbf{X}_{\mathbf{Seem}} + \mathbf{Sef}_m \mathbf{X}_{\mathbf{Sefm}}$ ) were substituted by the averaged one ( $\mathbf{Sav}_m \mathbf{X}_{\mathbf{Savm}}$ ). The value of the coefficient  $\mathbf{Sav}_m$  is the average value of  $\mathbf{See}_m$  and  $\mathbf{Sef}_m$ . The mol fractions produced from this system were summed. Calculation results showed that the sum of the mol fractions for **1a**, **2b**, and **2c** in the DMSO titrations were within  $1.0 \pm 0.2$ . This result tells us that (1) the quantum-calculation method we chose to calculate the chemical-shift differences between **1a**, **2b**, and **2c** versus **1d** were adequate; (2) the microstates that were used in the calculation of conformational distributions might be sufficient.

#### 1.4.4.2 Solution state study---DMSO perturbation of aqueous solution

The fluorine atoms on the phenyl rings should not produce hindered interactions between phenyl and xylyl rings in **C** and **F** states of **1a**, **2b**, and **2c**. Due to the isosteric relationship between fluorine and hydrogen atoms, the substitution of hydrogen by fluorine atoms in molecule **1a** should not cause significant structural difference.<sup>(95-97)</sup>

##### 1.4.4.2.1 Edgewise dispersive interactions

Conformational analyses were conducted under room temperature using deuterated DMSO ( $\text{CD}_3\text{SOCD}_3$ ) as an NMR co-solvent to perturb the aqueous solution. DMSO has been used in many chemical and biological studies.<sup>(98,99)</sup> A series of NMR experiments were done by adding DMSO to the aqueous ( $\text{D}_2\text{O}$ ) solution of molecules **1a**, **2b**, and **2c**. The experimental values of chemical shift differences for  $H_a$ ,  $H_b$ , and  $H_c$  between **1a**, **2b**, and **2c** versus **1d** were used in Equations (1)-(4) to calculate the mol fractions of the conformers. The results are drawn in Figure 1.19. In Figure 1.19, four-state solutions for compounds **1a**, **2b**, and **2c** are shown from left to right.

The uncertainties of the y axes in Figure 1.19 were originated from the uncertainties of calculation of the chemical shift difference between **1a**, **2b**, and **2c** versus **1d** plus the uncertainties of chemical shift of the  $H_{a-c}$  from NMR experiments. These uncertainties are complicated. However, all these are systematic errors; they will have the same effects on all models. They will decrease or increase the curves of **1a**, **2b**, and **2c** at the same time, which will not affect the observation of the trends of conformational changes for **F** and **C** states during DMSO perturbation from **1a** to **2c**.

From the conformational distributions in Figure 1.19, **1a**, **2b**, and **2c** have exactly the same trend for **F** and **C** states with the DMSO perturbation in aqueous solution, in which **C** states decrease while **F** states increase. The mol fractions of the four states for **1a**, **2b**, and **2c** were different, but they all changed in the same direction during DMSO titration.

The previously described study by the Cammers group generated the hypothesis that the **C** conformer is more favorable in the fluoroalkanol perturbation than the **F** conformer. It is because the **C** conformer has smaller SASA (solvent-accessible-surface-area) and hides more hydrogen atoms from the less favorable dispersive interactions between solvent and the edge of the aromatic rings of **1a** (C-H C-F bond interactions).<sup>(1,2)</sup>

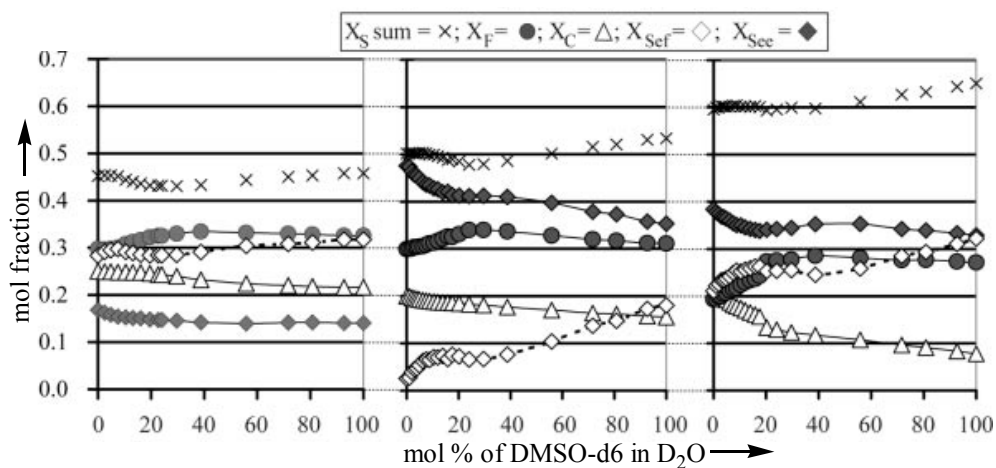


Figure 1.19. Mol fractions of four-state conformers (**C**, **F**, **S<sub>ee</sub>**, and **S<sub>ef</sub>**) as a function of the mol% DMSO-d<sub>6</sub> in D<sub>2</sub>O. Graphs for compounds **1a**, **2b**, and **2c** are shown from left to right.

In my work, a series of fluorinated derivatives (**2b** and **2c**) of the conformational solvent probe (**1a**) were used to test the dependence of the probe conformations on the dispersive interactions at the aromatic edges between solvent and probes. The only differences between the models **1a** to **2c** are the levels of the substitution of the hydrogen atoms on the phenyl rings with the fluorine atoms. **1a** is non-substituted, **2b** is 1,3,5-fluorinated, while in **2c** phenyl rings are all fluorine substituted. The nature of the aromatic edge of **2b** is midway between those of **1a** and **2c**. However, Figure 1.19 shows that fluorine substitutions on aromatic edge of the probes

did not change the trends of the conformational change. The dispersive interactions at the aromatic edges could not be the predominant force on the conformational change in **1a** during the fluoroalkanol perturbation. The same C-H C-F bond interaction exists in the fluoroalkanol cosolvent **1a** solution and DMSO cosolvent **2c** solution. If the less enthalpy favorable C-H, C-F bond interaction is the reason for the increase of cluster **S** and decrease of **F** state of **1a** in fluoroalkanol cosolvent, the same trend should be found in the DMSO perturbation of **2c**. The trend for **1a** DMSO cosolvent solution should be different from that of the **2c** in DMSO cosolvent solution. Some intermediate change should also be shown by **2b**.

However, Figure 1.19 shows exactly the same trend for **1a**, **2b**, and **2c** in DMSO cosolvent solution. The mol fraction of **F** states increase while the **C** states decrease with the increasing of the mol percent of DMSO for **1a**, **2b**, and **2c**. This ruled out the C-H, C-F bond interaction as a dominant effect for the increasing of cluster **C** and decreasing of **F** state of **1a** in fluoroalkanol cosolvent and put the previous results in question. Trends in the conformational change in **1a**, **2b**, and **2c** during the fluoroalkanol perturbation should be different if the edge-wise dispersive interactions between solvent and these probe molecules were dominant.

#### 1.4.4.2.2 Quadrupole moment interactions

The sum of **S** state mol fractions increased from **1a** to **2c**. The increasing of the **S** state means the decreasing of the **F** and **C** states with the increasing number of fluorine atoms on the phenyl rings, which also means the fluorinated phenyls in **2b** and **2c** associated less with the xylyl ring than with the phenyl in **1a**. Hexafluorobenzene and benzene have almost the same strength of the quadrupole moment with different signs.<sup>(39)</sup> According to the quadrupole interaction model, the interaction between hexafluorobenzene and benzene will be much stronger than the benzene-benzene ones.<sup>(40,41)</sup> If this interaction dominated in the solution state dication **1a**, **2b**, and **2c**, the splay **S** state should decrease from **1a** to **2c**, as **1a**>**2b**>**2c**. However, in Figure 1.19, we



have a totally different result, as  $2\mathbf{c} > 2\mathbf{b} > 1\mathbf{a}$ . This result of the calculation in Figure 1.19 questions the importance of quadrupole moment interactions in the dication folding in solution state. The importance of the dispersion forces versus quadrupole interactions has been discussed before with derivatives of *N*-benzyl-2-phenylpyridinium bromide, which are similar to our models.<sup>(100)</sup> Their results corroborated Wilcox's<sup>(85,86)</sup>, in which it was proposed that the dispersion forces are more important than the quadrupole interactions for the solution-phase  $\pi$ -stacking.

The effect of charge density of dication could be an important factor for the hydrophobic effect. The solvent-dependent dynamic conformational behavior could have resulted from ion pairing in solution. Strongly polar or charged compounds can strengthen the water/water interactions near the solute, and increase the density of the liquid state.<sup>(101)</sup> There are two distinct kinds of ion pairs in the solution: 1) contact ion pair  $M^+X^-$ , in which cation and anion contact with each other (no solvent molecule between them) and 2) solvent separated ion pair  $M^+ | \text{solvent} | X^-$ , in which cation and ion are separated by solvent molecules. Ions tend to associate into pairs in the low dielectric solvents, while the equilibria favor the solvent separated ion pair as the dielectric increases.<sup>(102)</sup>

#### 1.4.4.2.3 Electrostatic interactions between aromatic rings

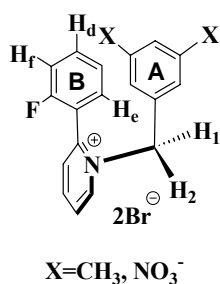


Figure 1.20. Electrostatic effects between aromatic rings.

The solvent-dependent conformational distribution of the probe molecules **1a**, **2b**, and **2c** may be due to the electrostatic interactions between the phenyl and xylyl rings. Waters and Rashkin reported recently the solution-state electrostatic effects between the

aromatic rings of similar molecules.<sup>(103)</sup> They determined the rotational barriers of substituted benzyl pyridinium bromides (Figure 1.20) in aqueous solution by simulating the line-broadened spectra of H<sub>1</sub> and H<sub>2</sub> in D<sub>2</sub>O. They found that in offset stacking of the model compound, the electron withdrawing substitution groups increased the rotational barrier, which depended heavily on the substitution position and the number of the substitution groups. The meta-substituent effect was much greater than the para-. Also the rotational barrier was much higher for a compound with two meta-substituents than that of a singly substituted molecule. This result is explained by the electrostatic interaction between two phenyl rings. Close proximity of meta-substituents in **A** ring to H<sub>d</sub> of the **B** ring make it possible for the attractive electrostatic interaction happening between the edge hydrogen ( $\delta^+$ ) and electron withdrawing groups ( $\delta^-$ ), which cannot happen for the para position.

In Figure 1.19, the total mol fractions of the **S** states (**S<sub>ee</sub>** + **S<sub>ef</sub>**) increased from **1a**, **2b**, to **2c**. This means the phenyl and xylyl rings stacked less with the increasing number of the fluorine atoms on the phenyl rings. Figure 19 also shows that **1a** prefers **S<sub>ef</sub>** conformations (xylyl and phenyl stacked edge-to-face); while **2b** and **2c** preferred **S<sub>ee</sub>** (xylyl and phenyl stacked edge-to-edge). This may be due to the electrostatic interactions between the aromatic rings. With fluorine substitution, due to large electronegativity of fluorine atoms, the fluorine atoms will carry partial negative charges ( $\delta^-$ ) on the phenyl rings. Because the hydrogen atoms on the xylyl ring carried partial positive charge ( $\delta^+$ ), the attractive electrostatic interaction will occur between the phenyl and xylyl ring. This explained the increase of the **S** state from **1a** to **2c**.

#### 1.4.4.2.4 Thermodynamic study

The enthalpies of the conformational distribution in pure D<sub>2</sub>O and DMSO were calculated from the Van't Hoff equation (Equation 1.3 is an example of the calculation of the enthalpies of C state in **1a**). The example equations for calculation of conformational distribution of C state in **1a** is shown in Equation 1.4.

$$\ln[K_{C1a}] = \frac{-\Delta H}{RT} + \frac{\Delta S}{R} \quad \text{-----} \quad (1.3)$$

Equation 1.3. Van't Hoff equation for enthalpy study of C state in **1a**.

$$K_{C1a} = \frac{X_{C1a}}{1-X_{C1a}} \quad \text{-----} \quad (1.4)$$

Equation 1.4. Equation for the calculation of conformational distribution of C state in **1a**.

The enthalpies of the conformational distribution are shown in Table 1.2. Values marked with an asterisk (\*) is because the small value of  $X_{\text{Sef}2b}$  of molecule **2b** gives unreasonable value of  $\Delta H_{\text{Sef}}$  in **2b**. The results of the experiments showed a linear relationship between  $\ln K$  and  $-1/T$ .

Table 1.2. Enthalpies of conformers from van't Hoff analysis in pure D<sub>2</sub>O and DMSO (kcal/mol)

Molecule (solvent)	$\Delta H_c$	$\Delta H_F$	$\Delta H_{\text{Sec}}$	$\Delta H_{\text{Sef}}$
<b>1a</b> (D <sub>2</sub> O)	-0.68	0.6	-0.17	0.11
<b>1a</b> (DMSO)	-0.17	-0.62	0.25	0.6
<b>2b</b> (D <sub>2</sub> O)	-0.82	0.56	-0.37	*
<b>2b</b> (DMSO)	0.17	-0.75	0.26	0.66
<b>2c</b> (D <sub>2</sub> O)	-1.2	0.92	-0.4	0.83
<b>2c</b> (DMSO)	0.34	-0.98	0.26	0.51

From Table 1.2, the values of the molecules show different signs from D<sub>2</sub>O to DMSO solution. The value change in different solvents fit the stability difference of conformers between D<sub>2</sub>O and DMSO in Figure 1.19. The **C** states are much more stable in water than in DMSO solutions, while **F** states appeared to possess higher stability in DMSO solutions.

However, electrostatic interactions between the aromatic rings cannot satisfactorily explain the switching directions of these enthalpies signs under different solvents. The electrostatic interactions of aromatic rings in **C** and **F** states are similar in **1a**, **2b**, and **2c**, but signs of enthalpy change when transferring from aqueous to organic solution, Figure 1.21.

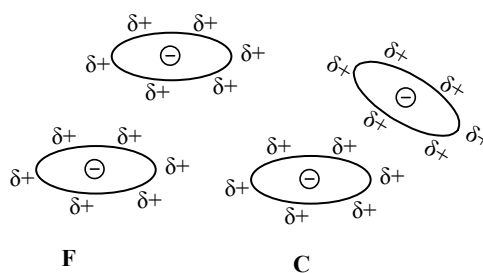


Figure 1.21. Complementary electrostatic interactions of **C** and **F** states.

Different solvents have different dielectric constants. The external dielectric of model molecules **1a**, **2b**, and **2c** changed with the different solvent environments. However, since the solvents could not reach inside the space between the aromatic rings in **1a**, **2b**, and **2c**, their internal dielectrics are more or less undisturbed. The net external, internal dielectric difference will change with different solvents. The different net solvent dielectric will have different effects on the molecular surface, which will affect the molecular conformations.

The enthalpy sign change in **F** and **S** states is probably due to the dielectric effect of solvent on the molecular surface. This is demonstrated by the molecular modeling calculation, in which the GB/SA solvent model was mainly developed to calculate the change of microscopic dielectric caused by the solvent exclusion.<sup>(104)</sup> In the

current study, AMBER and the MM2 force fields were chosen in the calculation; water and CHCl<sub>3</sub> were used as GB/SA solvents. The calculations were designed to mimic the solvent effects of the conformational changes. The calculation results agreed roughly with the conformational analysis described above. The **F** states possess higher stability in organic solutions while the **C** states are favored in water. The fact that molecular modeling calculations in different GB/SA solvent models corroborated with the NMR conformational analysis showed that dielectric effect of solvent may be important to the solution-state conformations of the probe molecules (**1a**, **2b**, and **2c**).

#### 1.4.4.3 Solid-state study

The crystal structures of **1a**, **2b**, and **2c** are shown in Figure 1.22. In the crystal structure of **1a**, there are two water molecules in a unit cell.<sup>(2)</sup> The probe molecule **2b** cocrystallized with two molecules of DMF. For the molecule **2c**, there is no solvent molecule in the crystal lattice.

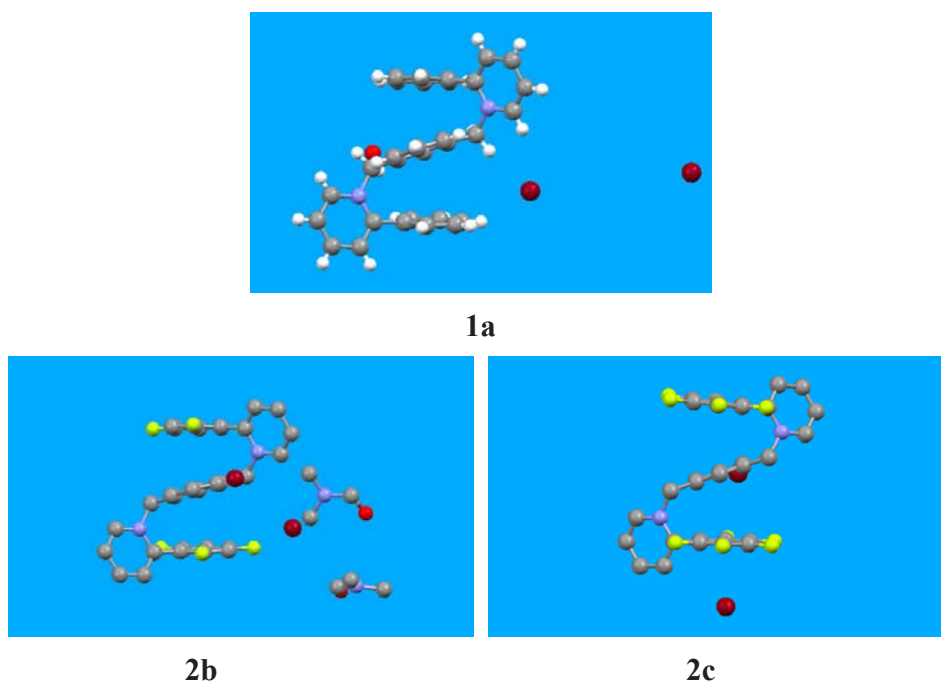


Figure 1.22. Crystal structures of **1a**, **2b**, and **2c**.

Molecules **1a**, **2b**, and **2c** had the same **F**-like conformation in the solid states. Same conformations were also used in the crystals of similar models, such as *N*-benzyl-2-phenylpyridinium bromide derivatives.<sup>(100)</sup> These similar **F**-like solid-state conformations shows the prevalent intramolecular  $\pi$ -stacking in these related structures.<sup>(100,105)</sup> The centroid distances between xylyl and phenyl rings in **1a**, **2b**, and **2c** are 3.94, 3.95, and 4.23 Å , respectively. The increased centroid distances show the increment of coulombic repulsion between aromatic rings, **2c** > **2b** > **1a**, in the solid state. This is counter intuitive to the quadrupole moment interactions.

Benzene has approximately the same magnitude of quadrupole moments as hexafluorobenzene. However, they are in different signs.<sup>(39)</sup> According to the quadrupole interaction model, the packing pattern of 1:1 hexafluorobenzene : benzene is face-to-face, center-to-center and the interaction between them is much stronger than that between benzenes.<sup>(39-42)</sup> However, the pentafluoro-substituted compound **2c** used the same **F** packing style as non-fluorinated compound **1a**; furthermore, **2c** had larger centroid distance than that of **1a**. Apparently, the packing of this series is not dominated by the quadrupole interaction.

Reexamining the series compounds and the similar models of *N*-benzyl-2-phenylpyridinium bromide derivatives, we see that all of these compounds have positive charges in the aromatic system. Many papers have published on the electrostatic interactions, such as cation- $\pi$  and aromatic interactions, of aromatic structures in the solution and solid-state.<sup>(106-111)</sup> To study the charge effect in the stacking of model molecules, neutral hydrocarbon compound **2e** (Figure 1.23) was synthesized.

### 1.5 Study of neutral hydrocarbon compound **2e**

2,2'-biphenyl- $\alpha,\alpha'$ -*m*-xylylene (**2e**) was synthesized. Compared with **1a**, which has two positive charges, **2e** is neutral and substitutes two quaternary nitrogen atoms with carbons. All others are the same. Compound **2e** also includes five aromatic rings and is isoelectronic to **1a**. Yet, **2e** is different from **1a** in solid states (Figure 1.23).

In solid state, **1a** is packed with intramolecular face-to-face  $\pi$ -stacking, while **2e** is packed in a splay pattern. This result tells us that charges are important in the formation of the solid-state stacking conformation of **1a**. When we remove the charge component in the conformational probe, the molecule loses its  $\pi$ -stacking conformation.

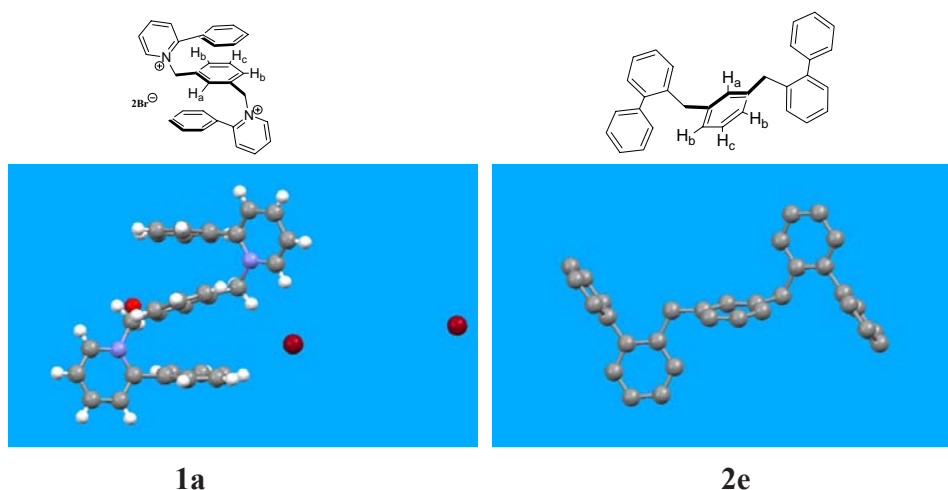


Figure 1.23. Molecular structures and crystal structures of **1a** and **2e**.

The difference between the charged (**1a**) and neutral (**2e**) ones in solid state is probably due to the charge- $\pi$  interaction. To further investigate the ion effect on the solid-state conformation of aromatic systems, the crystal structures of pyridinium derivatives (Chapter 2) and triangulene salt-pairs (Chapter 3) were studied.

## 1.6 Conclusion

A general protocol for the application of magnetic anisotropy to quantitative multi-state conformational analysis was suggested by the current study. The reliability of this method was checked by the mass balance. Positive solutions for the equations under different conditions confirmed the reliability. With carefully conformational analysis included **1a**, **2b**, and **2c**, the trends of conformational distribution of **1a** in different solvents in the previous analysis were corroborated.<sup>(1,2)</sup> This technique can be further used to study canonical interactions such as ion pairing, hydrogen bonding, and molecular recognition.

In the current study, dependence of the probe conformations on the dispersive interactions at the aromatic edges between solvent and probes was tested by fluorinating the probe molecule **1a**. Solution and solid studies of the probe molecules, **1a**, **2b**, and **2c** put the previous conclusion drawn by the Cammers group in question. Previous conformational analysis of **1a** in different solvents by the Cammers group generated the hypothesis that edge-wise dispersive interactions between solvent and aromatic rings are important in the folding of the model molecules. Current studies show that fluorination does not change the trends of conformational distributions of **1a**, **2b**, and **2c** during the DMSO titrations. The dispersive interaction at the aromatic edge could not be the predominant force for the conformational changes of **1a** during the fluoroalkanol perturbation.

Results drawn from solution- and solid-state studies of **1a**, **2b**, and **2c** also questioned the importance of quadrupole moment interactions in the dication folding. In solid state, **1a**, **2b**, and **2c** had the same F-like conformation. The centroid distances between xylyl and phenyl rings of these molecules increase from **1a** to **2c** ( $1a < 2b < 2c$ ). This shows the increment of coulombic repulsion between aromatic rings,  $2c > 2b > 1a$ , in the solid state. In solution state, studies showed that the stacking states decreased ( $1a > 2b > 2c$ ) with the increasing of the number of fluorine atoms on the phenyl rings. This also means the interactions of the phenyls to the xylyls in **2b** and **2c** are weaker than that of **1a**. If the quadrupole moments dominate the probes folding, trend in solid and solution states will be totally different.

Solid-state study of **1a**, **2b**, and **2c** indicated that charges might be important in the folding of these dications in the crystals. Neutral hydrocarbon 2,2'-biphenyl- $\alpha,\alpha'$ -*m*-xylylene (**2e**) was synthesized. It is isoelectronic and structurally similar to **1a**. In solid state, the charged molecules, **1a**, **2b**, **2c**, are packed with intramolecular face-to-face  $\pi$ -stacking while the neutral molecule, **2e**, is packed in a splay



pattern. Solid-state studies of **2e** and **1a** showed that charges are important in the formation of the folding conformations in solid state, which may be due to the charge- $\pi$  interaction.

## References

- 1) H. R. Mulla, A. Cammers-Goodwin, *J. Am. Chem. Soc.* **2000**, *122*, 738-739.
- 2) M. D. Sindkhedkar, H. R. Mulla, A. Cammers-Goodwin, *J. Am. Chem. Soc.* **2000**, *122*, 9271-9277.
- 3) S. K. Burley, G. A. Peko, *Science* **1985**, *229*, 23-28.
- 4) W. Saenger, *Principles of Nucleic Acid Structure*, Springer-Verlag, New York, 1984.
- 5) T. Benzing, T. Tjivikua, J. Wolfe, J. Rebek, Jr, *Science* **1988**, 266-268.
- 6) S. C. Zimmerman, W. Wu, *J. Am. Chem. Soc.* **1989**, 8054-8055.
- 7) J. M. Lehn, F. Schmidt, J. P. Vigneron, *Tetrahedron Lett.* **1988**, *29*, 5255-5258.
- 8) A. V. Muehldorf, D. Van Engen, J. C. Warner, A. D. Hamilton, *J. Am. Chem. Soc.* **1988**, *110*, 6561-6562.
- 9) D. Pasini, A. Kraft, *Curr. Opinion Solid State Mater. Sci.* **2004**, 157-163.
- 10) E. Gazit, *FASEB Journal* **2002**, 77-83.
- 11) A. E. Alexander, *J. Chem. Soc.* **1937**, 1813-1816.
- 12) R. J. Abraham, F. Eivazi, H. Pearson, K. M. Smith, *Chem. Commun.* **1976**, 698-699.
- 13) R. J. Abraham, F. Eivazi, H. Pearson, K. M. Smith, *Chem. Commun.* **1976**, 699-701.
- 14) C. A. Hunter, J. K. M. Sanders, *J. Am. Chem. Soc.* **1990**, 5525-5534.
- 15) G. R. Desiraju, A. Gavezzotti, *J. Chem. Soc. Chem. Commun.* **1989**, 621-623.
- 16) C. Janiak, *J. Chem. Soc., Dalton Trans.* **2000**, 3885-3896.
- 17) P. Hobza, H. L. Selzle, E. W. Schlag, *J. Phys. Chem.* **1996**, *100*, 18790-18794.
- 18) R. L. Jaffe, G. D. Smith, *J. Chem. Phys.* **1996**, *105*, 2780-2788.
- 19) F. Tran, J. Weber, T. A. Wesolowski, *Helv. Chim. Acta* **2001**, *84*, 1489-1503.
- 20) S. Tsuzuki, K. Honda, T. Uchimaru, M. Mikami, K. Tanabe, *J. Am. Chem. Soc.* **2002**, *124*, 104-112.
- 21) M. O. Sinnokrot, E. F. Valeev, C. D. Sherril, *J. Am. Chem. Soc.* **2002**, *124*, 10887-10893.
- 22) S. K. Burley, G. A. Petsko, *Adv. Protein Chem.* **1988**, *39*, 125-189.

- 23) G. B. McGaughey, M. Gagnu, A. K. Rappu, *J. Biol. Chem.* **1998**, *273*, 15458-15463.
- 24) T. Ishida, M. Doi, H. Ueda, M. Inoue, B. M. Scheldrick, *J. Am. Chem. Soc.* **1988**, *110*, 2286-2294.
- 25) S. R. Griffiths-Jones, M. S. Searle, *J. Am. Chem. Soc.* **2000**, *122*, 8350-8356.
- 26) H. E. Stanger, S. H. Gellman, *J. Am. Chem. Soc.* **1998**, *120*, 4236-4237.
- 27) F. J. Carver, C. A. Hunter, D. J. Livingstone, J. F. McCabe, E. M. Seward, *Chem. Eur. J.* **2002**, *8*, 2848-2859.
- 28) S. M. Butterfield, P. R. Patel, M. L. Waters, *J. Am. Chem. Soc.* **2002**, *124*, 9751-9755.
- 29) E. A. Meyer, R. K. Castellano, F. Diederich, *Angew. Chem. Int. Ed.* **2003**, *42*, 1210-1250.
- 30) F. Cozzi, M. Cinquini, R. Annunziata, T. Dwyer, J. S. Siegel, *J. Am. Chem. Soc.* **1992**, *114*, 5729-5733.
- 31) L. F. Newcomb, T. S. Haque, S. H. Gellman, *J. Am. Chem. Soc.* **1995**, *117*, 6509-6519.
- 32) A. Tanatani, K. Yamaguchi, H. Kagechika, *J. Am. Chem. Soc.* **1998**, *120*, 6433-6442.
- 33) A. G. Martinez, J. O. Barcina, A. F. Cerezo, R. G. Rivas, *J. Am. Chem. Soc.* **1998**, *120*, 673-679.
- 34) C. B. Martin, H. R. Mulla, P. G. Willis, A. Cammers-Goodwin, *J. Org. Chem.* **1999**, *64*, 7802-7806.
- 35) C. B. Martin, B. O. Patrick, A. Cammers-Goodwin, *J. Org. Chem.* **1999**, *64*, 7807-7812.
- 36) H. R. Mulla, A. Cammers-Goodwin, *J. Am. Chem. Soc.* **2000**, *122*, 738-739.
- 37) M. D. Sindkhedkar, H. R. Mulla, A. Cammers-Goodwin, *J. Am. Chem. Soc.* **2000**, *122*, 9271-9277.
- 38) J. Chen, A. Cammers-Goodwin, *Eur. J. Org. Chem.* **2003**, 3861-3867.
- 39) J. H. Williams, *Acc. Chem. Res.* **1993**, 593-598

- 40) C. R. Patrick, G. S. Prosser, *Nature* **1960**, 1021.
- 41) J. Vrbancich, G. L. D. Ritchie, *J. Chem. Soc., Faraday Tram. 2* **1980**, 649-659.
- 42) K. A. Dill, S. Bromberg, Molecular Driving Forces, Garland Science, New York, 2003.
- 43) S. J. Suresh, V. M. Naik, *J. Chem. Phys.* **2000**, 9727-9732.
- 44) C. A. Hunter, *Chem. Soc. Rev.* **1994**, 101-109.
- 45) C. A. Hunter, *Angew. Chem., Int. Ed. Engl.* **1993**, 32, 1584-1586.
- 46) F. Cozzi, J. S. Siegel, *Pure Appl. Chem.* **1995**, 67, 683-689.
- 47) C. A. Hunter, K. R. Lawson, J. Perkins, C. J. Urch, *J. Chem. Soc., Perkin Trans. 2.* **2001**, 5, 651-669
- 48) E. E. Tucker, S. D. Christian, *J. Phys. Chem.*, **1979**, 83, 426-427.
- 49) D. B. Smithrud, T.B. Wyman, F. Diederich, *J. Am. Chem. Soc.* **1991**, 113, 5420-5426.
- 50) N. T. Southall, K. A. Dill, *J. Phys. Chem. B.* **2000**, 104, 1326-1331.
- 51) F. Diederich, Cyclophanes, the Royal Society of Chemistry, Cambridge, 1991. pp.253.
- 52) W. L. Jorgensen, D. L. Severance, *J. Am. Chem. Soc.* **1990**, 112, 4768-4774.
- 53) J. Farges, Organic Conductors - Fundamentals and Applications, Marcel Dekker Inc. New York, 1994
- 54) S. B. Ferguson, F. Diederich, *Angew. Chem., Int. Ed. Engl.* **1986**, 1127-1129.
- 55) S. B. Ferguson, E. M. Sanford, E. M. Seward, F. Diederich, *J. Am. Chem. Soc.* **1991**, 5410-5419.
- 56) H. M. Colquhoun, Z. Zhu, D. J. Williams, *Org. Lett.* **2003**, 4353-4356.
- 57) W. A. Sheppard, C. M. Sharts, Organic Fluorine Chemistry, W. A. Benjamin Inc., New York, 1969.
- 58) M. R. Battaglia, A. D. Buckingham, J. H. Williams, *Chem. Phys. Lett.* **1981**, 421-423.

- 59) C. Dai, P. Nguyen, T. B. Marder, A. J. Scott, W. Clegg, C. Viney, *Chem. Commun.* **1999**, 24, 2493-2494.
- 60) S. Lorenzo, G. R. Lewis, I. Dance, *New J. Chem.* **2000**, 24, 295-304.
- 61) O. R. Lozman, R. J. Bushby, J. G. Vinter, *J. Chem. Soc., Perkin Trans. 2.* **2001**, 1446-1452.
- 62) A. V. Muehldorf, D. V. Engen, J. C. Warner, A. D. Hamilton, *J. Am. Chem. Soc.* **1988**, 110, 6561-6562.
- 63) E. C. Lee, B. H. Hong, J. Y. Lee, J. C. Kim, D. Kim, Y. Kim, P. Tarakeshwar, K. S. Kim, *J. Am. Chem. Soc.* **2005**, 127, 4530-4537.
- 64) P. M. Marcos, J. R. Ascenso, J. L. C. Pereira, *Eur. J. Org. Chem.* **2002**, 3034-3041.
- 65) G. J. Karabatsos, D. J. Fenoglio, in *Topics in Stereochemistry*, vol. 5 (Eds.: E. L. Eliel, N. L. Allinger), Wiley Interscience, New York, 1970, pp. 167.
- 66) P. Cimino, G. Bifulco, A. Evidente, M. Abouzeid, R. Riccio, L. Gomez-Paloma, *Org. Lett.* **2002**, 4, 2779-2782.
- 67) D. R. Kent, IV, N. Dey, F. Davidson, F. Gregoire, K. A. Petterson, W. A. Goddard, III, J. D. Roberts, *J. Am. Chem. Soc.* **2002**, 124, 9318-9322.
- 68) A. M. Belostotskii, M. Shokhen, H. E. Gottlieb, A. Hassner, *Chem. Eur. J.* **2001**, 7, 4715-4722.
- 69) C. W. Haigh, R. B. Mallion, *Progress in N. M. R. Spec.* **1979**, 13, 303-344.
- 70) A. M. Belostotskii, H. E. Gottlieb, P. Aped, *Chem. Eur. J.* **2002**, 8, 3016-3026.
- 71) V. Berl, I. Huc, R. G. Khoury, J. M. Lehn, *Chem. Eur. J.* **2001**, 7, 2798-2809.
- 72) Y. Fukazawa, S. Usui, K. Tanimoto, Y. Hirai, *J. Am. Chem. Soc.* **1994**, 116, 8169-8175.
- 73) Y. Fukazawa, T. Hayashibara, Y. Y. Yang, S. Usui, *Tetrahedron. Lett.* **1995**, 36, 3349-3352.
- 74) Y. Fukazawa, Y. Y. Yang, T. Hayashibara, S. J. Usui, *Tetrahedron* **1996**, 52, 2847-2862.

- 75) Y. Shigemitsu, M. Juro, Y. Mukuno, Y. Odaira, *Bull. Chem. Soc. Jpn.* **1978**, *51*, 1249-1250.
- 76) H. Iwamoto, Y. Y. Yang, S. Usui, Y. Fukazawa, *Tetrahedron Lett.* **2001**, *42*, 49-51.
- 77) T. Bürgi, A. Baiker, *J. Am. Chem. Soc.* **1998**, *120*, 12920-12926.
- 78) S. H. Gellman, T. S. Haque, L. F. Newcomb, *Biophys. J.* **1996**, *71*, 3523-3525.
- 79) G. Moyna, R. J. Zauhar, H. J. Williams, R. J. Nachman, A. I. Scott, *J. Chem. Inf. Comput. Sci.* **1998**, *38*, 702-709.
- 80) M. Lofthagen, J. S. Siegel, *J. Org. Chem.* **1995**, *60*, 2885-2890.
- 81) J. R. Cheeseman, G. W. Trucks, T. A. Keith, M. J. Frisch, *J. Chem. Phys.* **1996**, *104*, 5497-5509.
- 82) C. L. Perrin, M. A. Babian, I. A. Rivero, *J. Am. Chem. Soc.* **1998**, *120*, 1044-1047.
- 83) K. A. Connors, Binding Constants: The Measurement of Molecular Complex Stability, Wiley, New York, 1987.
- 84) D. R. Boyd, T. A. Evans, W. B. Jennings, J. F. Malone, W. O'Sullivan, A. Smith, *J. Chem. Soc. Chem. Comm.* **1996**, 2269-2270.
- 85) S. Paliwal, S. Geib, C. S. Wilcox, *J. Am. Chem. Soc.* **1994**, *116*, 4497-4498.
- 86) E. Kim, S. Paliwal, C. S. Wilcox, *J. Chem. Soc.* **1998**, *120*, 11192-11193.
- 87) L. F. Newcomb, T. S. Haque, S. H. Gellman, *J. Am. Chem. Soc.* **1995**, *117*, 6509-6519.
- 88) R. R. Gardner, L. A. Christianson, S. H. Gellman, *J. Am. Chem. Soc.* **1997**, *119*, 5041-5042.
- 89) M. D. Sindkhedkar, H. R. Mulla, M. A. Wurth, A. Cammers-Goodwin, *Tetrahedron* **2001**, *57*, 2991-2996.
- 90) J. Chen, A. Cammers-Goodwin, *Eur. J. Org. Chem.* **2003**, 3861-3867.
- 91) F. Mohamadi, N. G. J. Richards, W. C. Guida, R. Liskamp, M. Lipton, C. Caufield, G. Chang, T. Hendrickson, W. C. Still, *J. Comp. Chem.* **1990**, *11*, 440-467.
- 92) M. Scarsi, J. Apostolakis, A. Caflisch, *J. Phys. Chem. B.* **1998**, *102*, 3637-3641.

- 93) Y. Fukazawa, K. Ogata, S. Usui, *J. Am. Chem. Soc.* **1988**, *110*, 8692-8693.
- 94) M. P. Williamson, T. Asakura, *J. Magn. Reson.* **1991**, *94*, 557-562.
- 95) G. A. Patani, E. J. LaVoie, *Chem. Rev.* **1996**, *96*, 3147-3176.
- 96) Y. Takeuchi, T. Shiragami, K. Kimura, E. Suzuki, N. Shibata, *Org. Lett.* **1999**, *1*, 1571-1573.
- 97) C. W. Thornber, *Chem. Soc. Rev.* **1979**, *8*, 563-580.
- 98) J. Catalan, C. Diaz, F. Garcia-Blanco, *J. Org. Chem.* **2001**, *66*, 5846-5852.
- 99) F. G. Bordwell, X. M. Zhang, *Acc. Chem. Res.* **1993**, *26*, 510-517.
- 100) C. B. Martin, H. R. Mulla, P. G. Willis, A. Cammers-Goodwin, *J. Org. Chem.* **1999**, *64*, 7802-7806.
- 101) Kanno, H.; Ohnishi, A.; Tomikawa, K.; Yoshimura, Y. *J. Raman Spectrosc.* **1999**, *30*, 705-713.
- 102) T. H. Lowry, K. S. Richardson, Mechanism and Theory in Organic Chemistry, 3<sup>rd</sup> ed., Harper & Row, New York, 1987.
- 103) M. J. Rashkin, M. L. Waters, *J. Am. Chem. Soc.* **2002**, *124*, 1860-1861.
- 104) F. Mohamadi, N. G. J. Richards, W. C. Guida, R. Liskamp, M. Lipton, C. Caufield, G. Chang, T. Hendrickson, W. C. Still, *J. Comp. Chem.* **1990**, *11*, 440-467.
- 105) D. R. Body, T. A. Evans, W. B. Jennings, J. F. Malone, W. OSullivan, A. Smith, *Chem. Commun.* **1996**, 2269-2270.
- 106) S. Mecozzi, A. P. West, D. A. Dougherty, *J. Am. Chem. Soc.* **1996**, *118*, 2307-2308.
- 107) J. C. Ma, D. A. Dougherty, *Chem. Rev.* **1997**, *97*, 1303-1324.
- 108) G. W. Coates, A. R. Dunn, L. M. Henling, D. A. Dougherty, R. H. Grubbs, *Angew. Chem.* **1997**, *36*, 248-251.
- 109) G. W. Coates, A. R. Dunn, L. M. Henling, J. W. Ziller, E. B. Lobkovsky, R. H. Grubbs, *J. Am. Chem. Soc.* **1998**, *120*, 3641-3649.
- 110) P. Metrangolo, G. Resnati, *Chem. Eur. J.* **2001**, *7*, 2511-2519.
- 111) G. W. Gokel, L. J. Barbour, R. Ferdani, J. Hu, *Acc. Chem. Res.* **2002**, *35*, 878-886.

## Chapter Two

### The face-to-face, cation-to-cation packing motif in the solid state of simple pyridinium-derived aromatic rings

A study of solid-state structures of pyridinium-derived aromatic rings from the CSD (Cambridge Structural Database) was performed to investigate the solid-state  $\pi$ - $\pi$  interaction between cationic  $\pi$ -systems. The survey of pyridinium-derived aromatic rings showed a tendency of the cations to stack face-to-face (**FF**) as dimers. These **FF** packing patterns of the pyridinium-derived aromatic rings are different from their corresponding aromatic hydrocarbons, which are packed in herringbone patterns. The **FF** packing ( $\pi$ -stacking) of the pyridinium-derived aromatic rings may be due to the cation- $\pi$  interactions. Cations that can  $\pi$ -stack could likely lead to very strong cation- $\pi$  interactions. Maxima molecular orbital overlaps of the aromatic cations can happen in the **FF** packing ( $\pi$ -stacking). Since the molecules possess both empty orbitals and  $\pi$  bonds, they can be electronic donors and acceptors at the same time. Strong interactions may result from the overlap of these charged aromatic species.



## 2.1 Introduction

### 2.1.1 Interaction between charges

There are three kinds of charge interactions: cation-cation, cation-anion, and anion-anion, as shown in Figure 2.1.

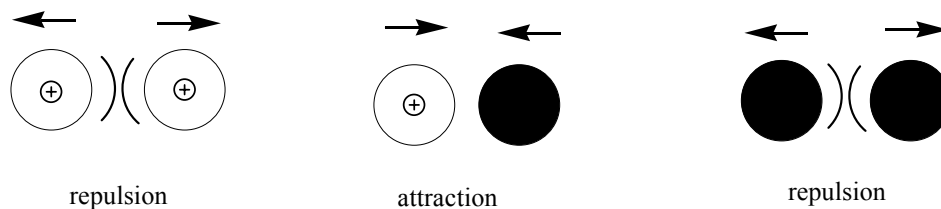


Figure 2.1. Interaction between charges. Black circle represents anion.

From what we learned in physics, the norm for the charge interactions is: there is repulsion between same sign charges; charges with different signs will attract each other. So, it is easy to imagine that two substances carrying same charges will repel each other. They will tend to stay farther away from each other than the similar, neutral compounds. However, this is not the case in the cationic  $\pi$ -systems, in which the cationic species will be packed closer than that of the isoelectronic neutral ones, which was inferred by measuring atomic distances between two rings in solid state.

### 2.1.2 C-H/ $\pi$ interactions

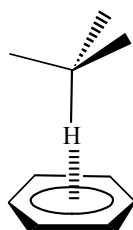


Figure 2.2. C-H/ $\pi$  interaction.

The C-H/ $\pi$  interaction refers to the attractions between hydrocarbons and  $\pi$ -systems, including arenes, alkenes, or alkynes within van der Waals distance as shown in Figure 2.2. Though it is a weak interaction, it is important in the stabilizing of the

bio-molecule structures.<sup>(1,2)</sup> It's also considered as weak hydrogen-bonds between C-H (soft acids) and  $\pi$ -systems (soft bases)<sup>(3)</sup> originated largely from dispersion interactions and also controlled to some extent by directional electrostatic interactions, which makes it orientation dependent,<sup>(3)</sup> similar to  $\pi$ - $\pi$  interactions. *Ab initio* calculations of Tsuzuki showed the interaction energies (De) between benzene-hydrocarbon complexes of ethane, ethylene, and acetylene are -1.82, -2.06, and -2.83 kcal/mol respectively, which increased with the acidity of the C-H residue participating in the binding.<sup>(4)</sup>

### 2.1.3 Packing modes in fused-ring aromatic hydrocarbons

Crystal engineering, with the goal of designing organic crystals with specific physical and chemical properties, is important in the research of material science and drug design. Predicting and further controlling the crystal structure is one of the major targets. Understanding the intermolecular interactions including non-covalent and hydrogen bonding is crucial to this job.<sup>(5-7)</sup>

X-ray crystallography can provide accurate molecular structures of the crystals from which the information of the non-covalent intermolecular interactions in the solid state can be acquired.<sup>(7)</sup> CSD (Cambridge Structural Database) and PDB (Protein Data Bank) are two data bases which are growing fast and providing enormous crystallographic information.<sup>(7-12)</sup> They have been increasingly important in finding information on intermolecular interactions,<sup>(8)</sup> such as hydrogen bonding,<sup>(13-20)</sup> C-C and CH- $\pi$  interaction,<sup>(6-9)</sup> and rational drug design.<sup>(6,9)</sup>

Gavezzotti described four structure types for crystals of planar or near planar polynuclear aromatic hydrocarbons.<sup>(6,8)</sup> They are represented by the packing patterns of naphthalene (herringbone (HB)), pyrene (herringbone structure with dimers (HBD)), coronene ( $\gamma$ ), and tribenzopyrene ( $\beta$ ), as shown in Figure 2.3. In the figure, packing patterns were generated with the Mercury program (version 1.4, released 2004 by CCDC) from corresponding Crystallographic Information Files (CIF) in CSD. The parameters defining these types are the shortest axis (SA) and interplanar angles (IA) (Table 2.1).

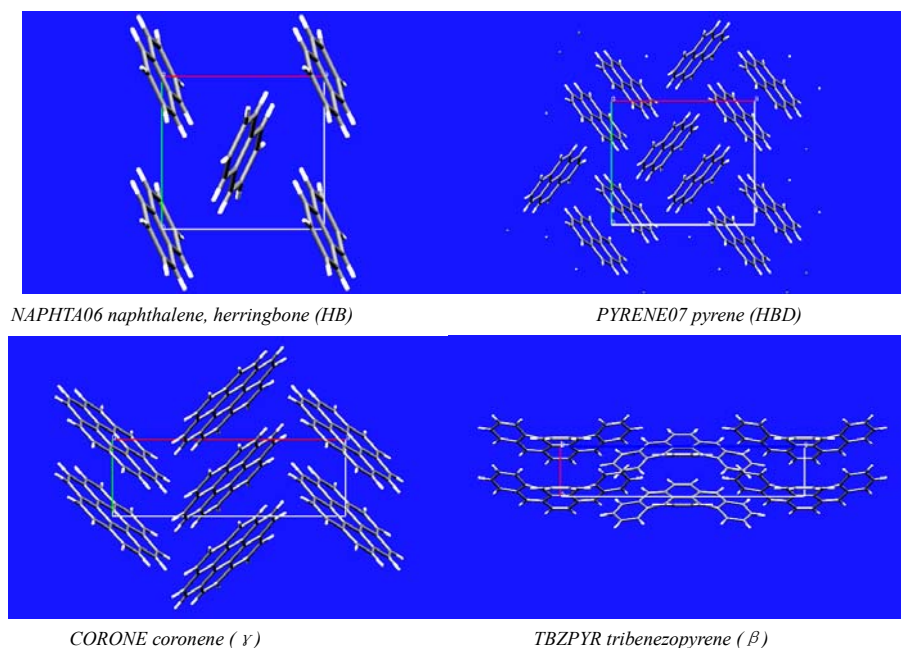


Figure 2.3. Four structure types in the crystals of planar or near planar polynuclear aromatic hydrocarbons.

Table 2.1. Parameters defining four types of packing patterns in the crystals of planar or near planar polynuclear aromatic hydrocarbons

	herringbone (HB)	herringbone with dimers (HBD)	$\gamma$	$\beta$
interplanar angles (IA)	$> 20^\circ$	$> 20^\circ$	$> 20^\circ$	$< 20^\circ$
shortest axis, Å (SA)	5.6-8 Å	$> 8$ Å	4.6-5.4 Å	$< 4$ Å

Herringbone (HB): In the crystal, nonparallel adjacent molecules with interplanar angles greater than 20 degrees are the closest molecules (with the shortest centroid distance), while there is no overlap between the parallel molecules. The  $\pi$ - $\pi$  interaction is weak in the HB structures. Some polynuclear aromatic hydrocarbons with herringbone crystals were shown in Figure 2.4.

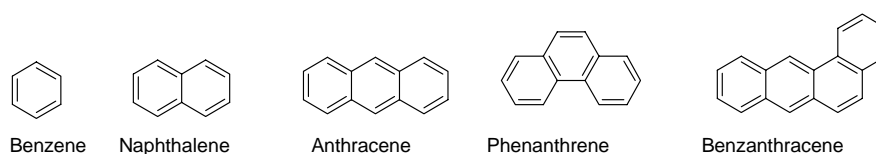


Figure 2.4. Polynuclear aromatic hydrocarbons with herringbone packing.

Herringbone structure with dimers (HBD): In HBD, the molecular pairs with parallel overlaps are packed with herringbone patterns.

$\gamma$ : In this type, herringbone-type packings are formed between columns containing face-to-face, overlapped, approximately parallel molecules separated by 3.4-3.8 Å interplanar distance.

$\beta$ : In  $\beta$  structures, all planar or near planar molecules are packed face-to-face, approximately parallel with each other and separated by 3.4-3.8 Å interplanar distance. The  $\pi$ - $\pi$  interaction dominates in these structures. The dihedral angles between aromatic planes are smaller than 20 degrees.

As shown above in Figure 2.3, the difference between the HB and the other three packing patterns is whether there is  $\pi$ - $\pi$  overlap inside the crystals. For the herringbone structure type, there is no  $\pi$ - $\pi$  overlap. The change of the packing pattern from herringbone to  $\beta$  structure was explained by the importance of the  $\pi$ - $\pi$  interaction versus C-H/ $\pi$  interaction.  $\pi$ - $\pi$  interactions turned out to be more important from non-herringbone to herringbone structures.<sup>(6,8,23)</sup>

With few exceptions, non-zero interplanar angles always exist in the crystal structures of aromatic hydrocarbons, as an intrinsic property.<sup>(6,8,23)</sup> The interactions between the aromatic systems are complicated; they may include the  $\pi$ - $\pi$  interaction (face-to-face **FF** and/or edge-to-face **EF**) and/or C-H/ $\pi$  interaction. What we are interested in here is the structure of  $\pi$ - $\pi$  interaction (non-herringbone) versus that of non  $\pi$ - $\pi$  interaction (herringbone). The trend of the change of the packing pattern from herringbone to non-herringbone (HBD,  $\gamma$ ,  $\beta$ ) structures shows increased importance of the  $\pi$ - $\pi$  interaction with the closest molecules. The face-to-face contacts (overlaps) within van der Waals distance of aromatic rings increase from HB to other patterns. These overlaps will provide more atomic interactions between aromatic rings, which in turn increase the  $\pi$ - $\pi$  interactions.  $\pi$ - $\pi$  interaction, which was inferred by measuring atomic distances in solid state, turned out to be more important from herringbone to

non-herringbone structures. Nevertheless, we still use the four packing patterns (HB, HBD,  $\gamma$ ,  $\beta$ ,) when we describe the packing of pyridinium for clearer descriptions.

#### 2.1.4 Cation- $\pi$ interaction

Cation- $\pi$  interaction has been shown to be a major non-covalent force in many chemical and biochemical systems.<sup>(24-34)</sup> The binding force is strong for the prototype cation- $\pi$  interaction. In  $K^+$ -benzene complex, the cation- $\pi$  interaction (19 kcal / mol) is greater than the  $K^+$ -water interaction energy (18 kcal / mol).<sup>(35)</sup> The most stable configuration for the simple cation-benzene interaction is to place the cation in the center of the benzene ring along the 6-fold axis of the ring,<sup>(29)</sup> as shown in Figure 2.5.

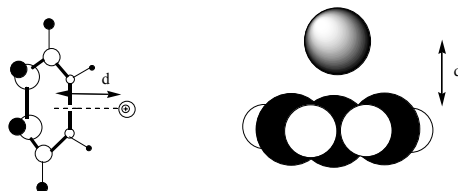


Figure 2.5. Cation- $\pi$  interaction.

Based on the calculation, it is the electrostatic, not the quadrupole interaction that plays a prominent role (>60%) in the cation- $\pi$  interaction, although some other interactions, as polarizability, dispersion forces, or charge-transfer, may also exist.<sup>(27)</sup> It is because the distance between the centers of the cation and benzene (<3 Å) is much shorter than the 5 Å distance for a valid stable point charge-quadrupole interaction.<sup>(29)</sup> The orientation of the distribution of the electrostatic surface on the benzene rings, which can be treated as  $+\delta$  charge at the nucleus center and two  $-\delta/2$  charges at a  $d$  distance, as shown in Figure 2.6, determines that the best position (orientation) of the cations is on the top of the 6-fold center of the benzene rings.<sup>(36)</sup>

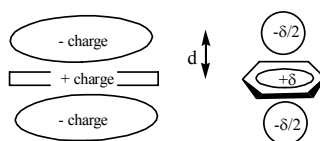


Figure 2.6. Orientation of the distribution of electrostatic surface on benzene ring.

### 2.1.5 Delocalized cation- $\pi$ interaction

Delocalized cation- $\pi$  interaction refers to the interaction between two cationic-aromatic-systems in which the charges are delocalized. The inorganic (or point-charge) cation- $\pi$  interaction is strong.<sup>(45)</sup> How about the delocalized cation- $\pi$  interaction? Will it show the same behaviors as the point-charge-cation- $\pi$  interaction? What impact will the delocalized charge make to the  $\pi$ - $\pi$  interactions, hence to the crystal structure patterns in these compounds? Furthermore, how about the delocalized cation-delocalized anion interaction?

## 2.2 Face-to-face packing motif in simple pyridinium crystals

It was hypothesized that the cationic aromatic system will have a tendency to stack face-to-face and the  $\pi$ -stacking interaction between them will be stronger than that of the neutral  $\pi$ -stacking. This is because the strong cation- $\pi$  interaction could be formed between the delocalized charge of one ring and the  $\pi$ -system of the other ring. The work of this chapter supports this hypothesis. A study of the CSD (Cambridge Structural Database) was performed to investigate the solid-state interaction between cationic  $\pi$ -systems. The packing patterns of the crystal structures of pyridinium-derived aromatic rings were studied. The charged  $\pi$ -stacking of pyridinium-derived cations were compared with the neutral  $\pi$ -stacking of corresponding hydrocarbons.

### 2.2.1 Pyridinium and nitrogen substituted fused-ring aromatic hydrocarbons

Pyridinium is a simple, stable cation which carries one delocalized charge. It is very common in chemistry and biochemistry. Pyridinium is an aromatic cation that is isoelectronic to benzene. In recent years, many crystal structures of pyridinium and some other nitrogen substituted fused-ring aromatic hydrocarbons (most of them have two and three rings) with different anions have been collected in the crystal structure database, CSD (Cambridge Structural Database). These crystals are good sources for the investigation of delocalized cation- $\pi$  interaction in solid state.

## 2.2.2 Methodology

The crystallographic information of benzene, naphthalene *etc.* of the twelve herringbone structures were used directly from the literature.<sup>(6,8)</sup> Searching of the corresponding pyridinium substructures was conducted on ConQuest (version 1.7, Copyright© 2004 the Cambridge Crystallographic Data Center (CCDC)): the twelve aromatic hydrocarbons were used as templates. All the carbon atoms were changed to NM (any non-metal), with extra filters: the R factor < 0.1, not disordered, no errors, not polymeric, no powder structures, and only in organics.

### 2.2.2.1 CSD code, packing patterns and the calculation of overlap percentages

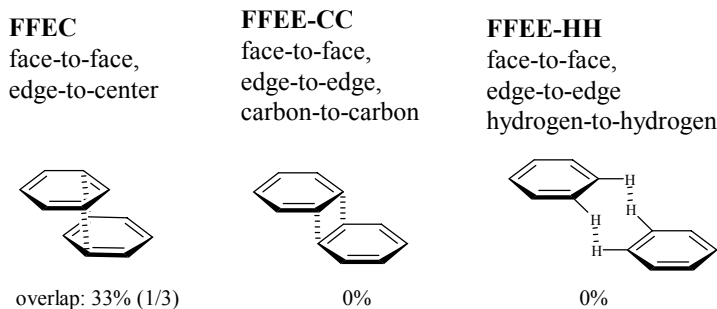


Figure 2.7. Examples of the packing patterns.

In this chapter, each pyridinium derivative is represented by an alphabetic code (code that is used in Cambridge Structural Database (CSD code)) with six capital letters (e.g. PYRDHN represents pyridinium nitrate). Packing patterns and some figures (figure 2.3, 2.8-13, 2.15-16) of pyridinium derivatives were generated with the Mercury program (version 1.4, released at 2004 by CCDC) from corresponding Crystallographic Information Files (CIF) in CSD. There are several kinds of face-to-face packing with different overlap percentages. Some examples of the packing patterns, their names and overlaps are shown in Figure 2.7. The nitrogen atoms were omitted for clarity. The overlap percentages were calculated based on the ratio of overlapped areas to the total areas of the backbone of the face-to-face packing aromatic rings when looking perpendicularly to the aromatic rings.

### 2.2.2.2 Counterions

There are many interactions between aromatic compounds, such as hydrogen bonding,  $\pi$ - $\pi$  interaction, quadrupole-quadrupole interaction, steric issues, *etc.* All of these will contribute to the structures of the aromatic crystals. To minimize the unnecessary effects, such as the  $\pi$ - $\pi$  interaction between the cations and the counterions and steric effect of bulky counterion, choosing of the counterions is important. The bulky counterions, which will make the case more complicated by introducing the steric issues (such as non-planar polyaromatic compounds or simple inorganic compounds which are greater than the size of the cations, as 4.6 Å for pyridinium) were filtered out of the data set.

From the discussion in chapter one, the hydrogen bonding is strong compared to other non-covalent interactions. Some of the hydrogen bonds will form 2D or 3D structures in crystals. Crystals that include these structures formed by counterions or by counterion and neutral compounds will be discussed separately. Crystals with only the inorganic counterions will also be discussed separately.

### 2.2.2.3 Definition of pseudo

In literature, the definitions of the four packing patterns are based on the shortest axis, interplanar angles between columns, and overlaps between the aromatic rings. In the pyridinium crystals, sometimes not all these criteria can be satisfied. The pseudo means either the shortest axis value or the overlap area for the pattern may not be satisfied.

## 2.3 Pyridinium, one-ring cation

A total of 78 crystals were found for the pyridinium cation. All of the bulky (non-planar or inorganic species greater than the size of the pyridine) counterions were deleted, leaving only 36. The CSD codes, corresponding counterions, packing patterns and the overlap of all crystals are shown in Table 2.2.



Table 2.2. CSD codes, corresponding counterions, packing patterns and the overlaps of pyridinium crystals

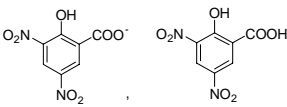
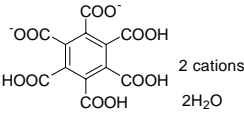
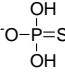
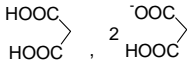
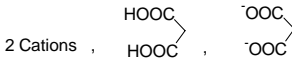
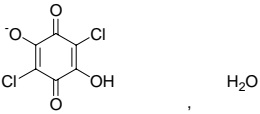
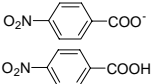
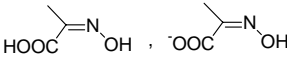
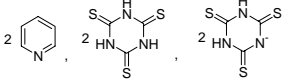
CSD code	anion	packing type	ring overlap, %	interface distance Å
AJEBIA		pseudo $\beta$ cation-cation	<b>FFEE</b> , 0%	3.46
BAXZOQ		NA	<b>FFEC</b> , dimer, 33%	3.47
COPDEQ		pseudo $\gamma$	<b>FFEC</b> , 33%	3.31
DUVLUB		pseudo $\beta$	<b>FFEC</b> , 33%	3.39
DEFCUM		pseudo $\beta$	<b>FFEE-CH</b> , 0%	3.45
DEHSOY10	F <sup>-</sup> , HF	pseudo $\beta$	<b>FFEC</b> , 33%	3.48
DEHSUE10	F <sup>-</sup> , 2HF	pseudo $\beta$	<b>FFEE-CC</b> , 0%	3.44
DEHTAL10	F <sup>-</sup> , 3HF	pseudo $\beta$	<b>FFEE-CH</b> , 0%	3.45
FOXMEK10	Cl <sup>-</sup> , HCl	pseudo $\beta$	<b>FFEE-CH</b> , 0%	3.44
GEQBIN	F <sup>-</sup> , 5HF	pseudo $\beta$	<b>FFEC</b> , dimer, 33%	3.66
GOMPEB		NA	<b>FFEC</b> , dimer, 33% Cat-cat	3.48
HOHMOG01 HOHMOG05	IO <sub>4</sub> <sup>-</sup>	pseudo $\gamma$	<b>FFEE-HH</b> , 0%	2.80 2.85
IDAHOK		NA	NA	NA
JAVFOB	Cl <sup>-</sup> , 3HCl	NA	NA	NA
JAVFUH	Cl <sup>-</sup> , 5HCl	NA	NA	NA
KOWZUR		NA	NA	NA

Table 2.2 (continued)

KOXREU		NA	NA	NA
LEZJIH		pseudo $\gamma$	<b>FFEE-HH</b> , dimer, 0% <b>FFEC</b> with anion	3.37
LIDYOM		pseudo $\beta$	<b>FFEE-CH</b> , 0%	3.37
PYRDHN	$\text{NO}_3^-$	pseudo $\gamma$	<b>FFEC</b> , 33%	3.51
PYRPIC01		pseudo $\gamma$ cation- cation	<b>FFEC</b> , 33%	3.51
PYRPIC02		pseudo $\beta$ Cat-cat	<b>FFEC</b> , dimer, 33%	3.51
PYRPIC03		pseudo $\beta$	<b>FFEE-HH</b> , dimer 0% <b>FFEC</b> with anion	3.58
PYRHCL02	$\text{Cl}^-$	pseudo $\gamma$	<b>FFEC</b> , 33%	3.40
PYRHCL11	$\text{Cl}^-$	pseudo $\beta$	<b>FFEE-CH</b> , 0%	3.23
QAFFOS		pseudo $\gamma$	<b>FFEC</b> , 33%	3.44
QOQVOH	$\text{CH}_3\text{SO}_3^-$	herringb one	0%	NA
RUVYIQ	$\text{CF}_3\text{COO}^-$	herringb one	0%	NA
TURPYB03	$\text{Br}^-$ , $2 \text{H}_2\text{N}-\text{C}(=\text{S})-\text{NH}_2$	pseudo $\gamma$	<b>FFEC</b> , 33%	3.50
UDETOM01	$\text{I}^-$ , $2 \text{H}_2\text{N}-\text{C}(=\text{S})-\text{NH}_2$	pseudo $\gamma$	<b>FFEC</b> , 33%	3.67
VEGKIB	$\text{H}_3\text{PO}_4, \text{H}_2\text{PO}_4^-$	pseudo $\beta$	<b>FFEC</b> , dimer, 33%	3.40
WADPEX		pseudo $\beta$	<b>FFEE-CC</b> , 0%	3.42
XESPEQ XESPEQ01		pseudo $\beta$ cation- cation	<b>FFEC</b> , dimer, 33%	3.63 3.70

Table 2.2 (continued)

XICBAM		NA	FFEE-HH, dimer 0%	3.15
--------	---	----	----------------------	------

As we can see from Table 2.2, most of the pyridinium crystals had face-to-face packing patterns (**FF**) and the interplanar distances are within the  $\pi$ -stacking distance (3.3–3.8 Å).<sup>(37,38)</sup> The packing patterns of these pyridinium crystals will be discussed based on the different categories of the counterions.

### 2.3.1 Counterions forming structures of endless hydrogen-bond connections

Hydrogen bonding is very common inside the crystals and has been extensively studied.<sup>(5-7)</sup> If the counterions have the hydrogen bond donor and acceptor at the same time, structures of endless connections of the counterions through hydrogen bonding may be formed inside the crystals by the counterions.<sup>(42)</sup> They can be grouped as one (1D) to three dimensional (3D) structures. Because hydrogen bonds are stronger than other non-covalent interactions, crystals with anions capable of forming hydrogen-bond structures should be studied separately. There are twelve crystals with the 1D-3D counterion structures formed due to hydrogen bonding.

#### 2.3.1.1 3D structures formed by counterions

Three dimensional (3D) structures of endless connections of the counterions through hydrogen bonding may be formed inside the crystals by the counterions.<sup>(42)</sup> Due to the strong interactions of the hydrogen bonds, the packing patterns of the pyridinium may be dominated by the structures in these crystals. 3D cage shape structures can be formed by some counterions, which included one or two cations inside. The top and the bottom of these cation(s) were occupied by the counterions, which were part of the cage.

**a) Single cation in the cage**

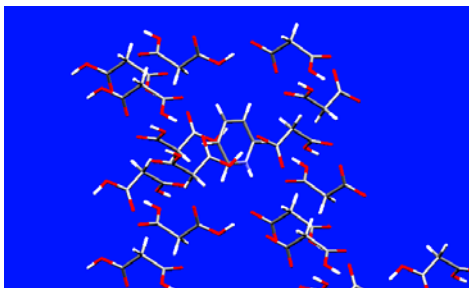


Figure 2.8. Packing pattern in KOXREU.

In the crystal structures of KOWZUR, IDAHOK and KOXREU in Table 2.2, only one pyridine cation was included inside the 3D structure of counterions. The cations were separated from each other, so there was no cationic face-to-face packing. The sample crystal structure is shown in Figure 2.8.

**b) Two cations in the cage**

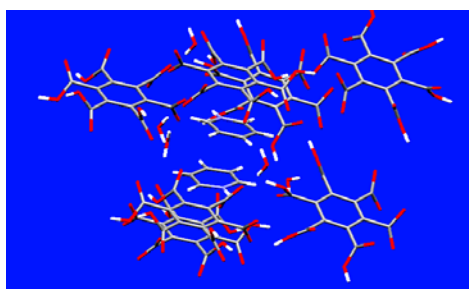


Figure 2.9. Packing pattern in BAXZOQ.

In the crystal structures of BAXZOQ, GOMPEB, XICBAM, VEGKIB and WADPEX, there are two pyridiniums in each anion cage. These two cations were packed as **FFEC** dimer in the cage. The cationic dimers are far away from each other due to the cage separation. However, inside the cage, the cations can choose to pack either the face-to-face or T-shape to each other. The fact that all cations were packed face-to-face inside these crystals shows the preference of the **FF** packing of the pyridinium.

### 2.3.1.2 2D structures formed by counterions

Some counterions can form 2D planar structures inside crystals, such as the anion in the crystal structure of COPDEQ. Parallel 2D planes were formed by  $\text{H}_2\text{PO}_3\text{S}^-$  through hydrogen bonds. When viewed perpendicularly to the 2D planes, the  $\text{H}_2\text{PO}_3\text{S}^-$  molecules overlap with each other forming columnar structures as shown in Figure 2.10. In the figure, the  $\text{H}_2\text{PO}_3\text{S}^-$  molecules are shown in red. The cations were packed **FFEC** inside the column. Similar 2D structures were found in the crystal structures of DUVLUB and QAFFOS (all **FFEC** packing, pseudo  $\beta$  or  $\gamma$ ).

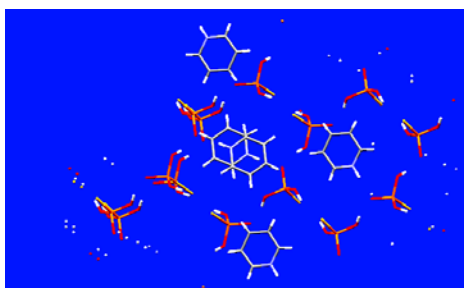


Figure 2.10. Packing pattern in COPDEQ.

### 2.3.1.3 1D structures formed by counterions

In the crystal structures of LIDYOM and DEFCUM, chain-like 1D structures can be formed by the anions through the hydrogen bondings. Figure 2.11 shows the crystal structure of LIDYOM, in which the anions are shown in red. The face-to-face packing or the parallel placement is the only packing pattern for the cations (**FFEC** or **FFEE-CH**, pseudo  $\beta$ ) inside these crystals.

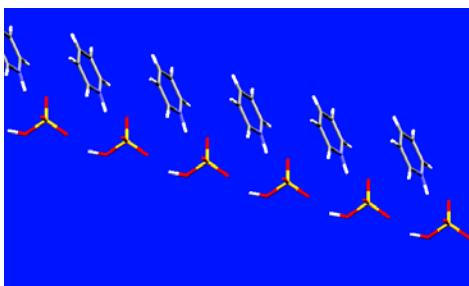
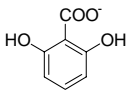
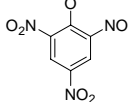
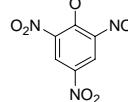
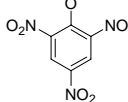
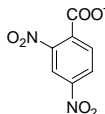
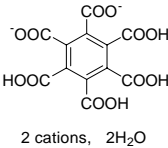
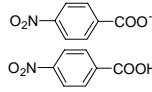
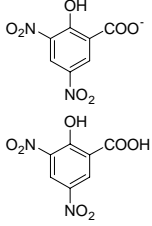


Figure 2.11. Packing pattern in LIDYOM.

Although the hydrogen-bonding interaction is strong and sometimes the counterions can form many kinds of the packing structures by themselves inside the crystals, pyridiniums showed the preference of face-to-face packing motif.

### 2.3.2 Aromatic counterions

Table 2.3. Pyridinium crystals with aromatic counterions. Pattern 1 is viewed from pyridinium only and pattern 2 includes all the aromatic rings inside the crystals, including the pyridinium and the counterion.

CSD code	LEZJIH	PYRPIC01	PYRPIC02	PYRPIC03
counterions				
pattern1	pseudo $\gamma$	pseudo $\gamma$	pseudo $\gamma$	pseudo $\beta$
overlap	<b>FFEE-HH</b> , dimer	<b>FFEC</b>	<b>FFEC</b> , dimer	<b>FFEE-HH</b> , dimer
pattern2	pseudo $\gamma$	pseudo $\gamma$	pseudo $\gamma$	pseudo $\beta$
overlap cation-cation cation-anion	<b>FFEE-HH</b> <b>FFEE-CC</b>	<b>FFEC</b> NA	<b>FFEC</b> NA	<b>FFEE-HH</b> <b>FFEC</b> , dimer
CSD code	XESPEQ XESPEQ01	BAXZOQ	IDAHOK	AJEBIA
counterions				
pattern1	pseudo $\beta$	NA	NA	pseudo $\beta$
overlap	<b>FFEC</b> , dimer	<b>FFEC</b> , dimer	NA	<b>FFEE-CC</b>
pattern2	pseudo $\gamma$	pseudo $\gamma$	pseudo $\gamma$	pseudo $\beta$
overlap cation-cation cation-anion	<b>FFEC</b> , dimer NA	<b>FFEC</b> , dimer <b>FFEC</b> , dimer	NA NA	<b>FFEE-CC</b> NA

There are nine pyridinium crystals that have aromatic counterions. They are shown in Table 2.3. From the table, it can be found that face-to-face (**FF**) packing motif is preferred by the pyridinium in these crystals (except BAXZOQ and IDAHOK).

In the crystal structures of PYRPIC01 and PYRPIC02, the cations were packed in the same style, **FFEC**. In the crystal structure of PYRPIC 03, all the aromatic rings stacked face-to-face, which belong to the pseudo  $\beta$  pattern. The pyridiniums were packed as **FFEE** dimers in this crystal. The **FFEC** anionic dimers and **FFEE** cationic dimers were packed alternately; the cationic dimers were packed **FFEC** to the anionic dimers as shown in Figure 2.12. The crystal structures are exactly the same for XESPEQ and XESPEQ01, in which **FFEC** dimers were formed by the pyridiniums. In the crystal structure of LEZJIH, pyridiniums formed **FFEE-HH** dimers. In AJEBIA, **FFEE-CC** cationic dimers were formed.

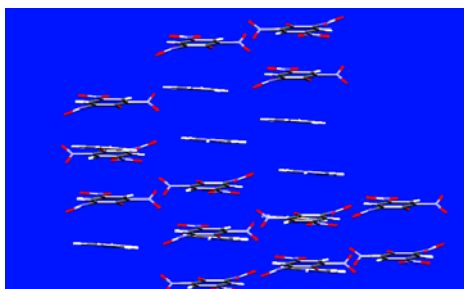


Figure 2.12. Packing pattern in PYRPIC03.

In the crystal structure of BAXZOQ, due to the 3D cage formed by anions and H<sub>2</sub>O (see the 3D structure discussion above in Section 2.3.1.1), the **FF** cationic dimers can be found inside the cage. For the whole crystal, all aromatic rings (cations and anions) were packed **FFEC** and used pseudo  $\gamma$  pattern. The **FFEC** cationic dimers were separated by the **FFEC** cation anion packing, as shown in Figure 2.13

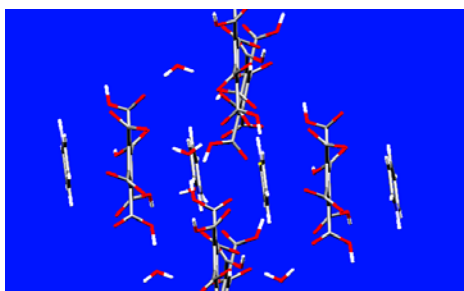


Figure 2.13. Packing pattern in BAXZOQ.

In the crystal structure of IDAHOK, 3D cages (see the 3D structure discussion above in Section 2.3.1.1) were formed by anions around single cations. Although cations were parallel packed, they were too far away from each other to have the  $\pi$ - $\pi$  interaction.

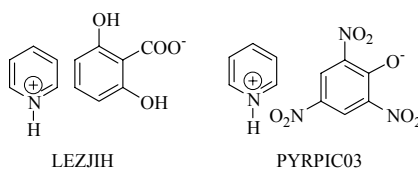


Figure 2.14. Crystals with **FF** cation-anion packing of one-ring cations.

Because  $\pi$ - $\pi$  interaction can be formed between the pyridinium and the aromatic counterions, the packing patterns in pyridinium crystals with aromatic counterions may be complicated. The pyridinium can be packed face-to-face either to cations and/or to the aromatic counterions. For nine crystals of pyridinium with aromatic counterions, most of them preferred the **FF** cation-cation dimer. Only two crystals (Figure 2.14) showed the preference of the cation-anion packings over the cationic dimers. In both crystal structures, only the **FFEE-HH** cationic dimers could be found. However, in the crystal structure of LEZJIH, the cations were packed alternately with the anions in the **FFEE-CC** pattern. In PYRPIC03, **FFEC** dimers were formed between the cations and the anions. This is probably due to the resonance. All the anions had hydroxyl groups. Part of negative charges on oxygen atoms could be transferred to aromatic rings by resonance. The strong aromatic-cation aromatic-anion interactions, which will be discussed in next chapter, will form between the aromatic cations and anions.



Nevertheless, if we consider the packing of cations and anions at the same time, the packing patterns of all these charged aromatic ions introduce better atomic contacts than that of the corresponding hydrocarbon of the cations. All cations packed in either pseudo  $\gamma$  or pseudo  $\beta$  packing styles with aromatic rings. This means that  $\pi$ - $\pi$  interaction is preferred over CH- $\pi$  interaction.

### 2.3.3 Simple counterions

As discussed above, in some crystals, counterions and/or the neutral compounds can form 1D, 2D, or 3D structures through hydrogen bondings. Also, hydrogen bonds can be formed between pyridiniums and counterions. The N--H--X hydrogen bonds were found in many crystal structures.<sup>(40-42)</sup> Because hydrogen bondings are strong interactions, one can argue that the formation of the pyridinium packing patterns may be more or less controlled by the counterion structures (1-3D). However, in the crystals with the simple counterions, the packing patterns of the pyridinium rings will confirm the idea that the packing patterns of the cations are dominated by the interactions between the cations. This will rule out the possibility that the **FF** packing pattern is controlled by hydrogen bonding. All the crystals studied below have only simple counterions, with no special 1D-3D structures and no aromatic counterions.

#### 2.3.3.1 Small size simple counterions

There are eleven crystals formed by pyridinium and small, simple counterions as shown in Table 2.4. Hydrogen bonds may be formed between pyridiniums and the counterions and/or some neutral compounds, such as water. However, in these crystals, there is no 1-3D endless counterion structure. The size and the shape of these counterions, the neutral compounds, and the simple structures formed by them through hydrogen bonds will be important to the packing patterns of pyridiniums. From Table 2.4, face-to-face (**FF**) packing patterns can be found in nine crystals. The crystal structures in which face-to-face-dimer packing pattern cannot be found are that of JAVFUH and JAVFOB. This may be due to the large sizes of the simple structures formed by the

counterions. In the crystal structure of JAVFUH, the counterion,  $\text{Cl}^-$ , forms a square pyramid with  $\sim 5 \text{ \AA}$  on each size, while in JAVFOB, the tetrahedron shape structures with the sizes  $\sim 6 \text{ \AA}$  were formed by a  $\text{Cl}^-$  and four  $\text{HCl}$  molecules, as shown in Figure 2.15.

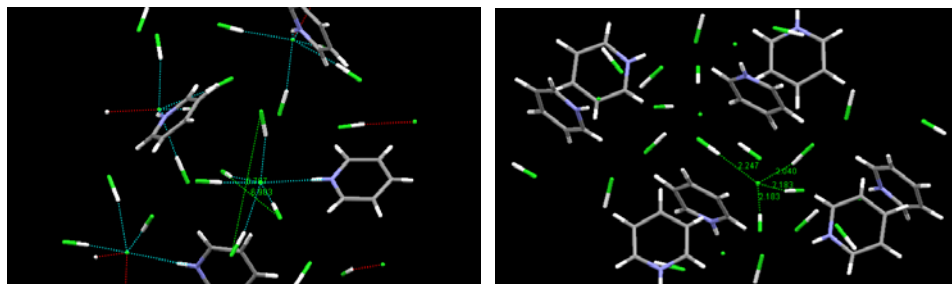


Figure 2.15. Hydrogen-bond structures in JAVFUH and JAVFOB.

Table 2.4. Pyridinium crystals with small size simple counterions

CSD code	DEHSOY10	DEHSUE10	DEHTAL10	FOXMEK10
counterions	$\text{F}^-$ , HF	$\text{F}^-$ , 2HF	$\text{F}^-$ , 3HF	$\text{Cl}^-$ , HCl
pattern	pseudo $\beta$	pseudo $\beta$	pseudo $\beta$	pseudo $\beta$
overlap	<b>FFEC</b>	<b>FFEE-CC</b>	<b>FFEE-CH</b>	<b>FFEE-CH</b>
CSD code	GEQBIN	JAVFOB	JAVFUH	PYRHCL02
counterions	$\text{F}^-$ , 5HF	$\text{Cl}^-$ , 3HCl	$\text{Cl}^-$ , 5HCl	$\text{Cl}^-$
pattern	pseudo $\beta$	NA	NA	pseudo $\gamma$
overlap	<b>FFEC</b> , dimer	NA	NA	<b>FFEC</b>
CSD code	PYRHCL11	TURPYB03	UDETOM01	BENZEN
counterions	$\text{Cl}^-$	$\text{Br}^-$ , $2 \text{ H}_2\text{N}-\overset{\text{S}}{\parallel}{\text{C}}-\text{NH}_2$	$\text{I}^-$ , $2 \text{ H}_2\text{N}-\overset{\text{S}}{\parallel}{\text{C}}-\text{NH}_2$	
pattern	pseudo $\beta$	pseudo $\gamma$	pseudo $\gamma$	herringbone
overlap	<b>FFEE-CH</b>	<b>FFEC</b> , 33%	<b>FFEC</b> , 33%	NA

With the simple counterions (except those formed large size simple structures with other neutral molecules), all pyridiniums were packed face-to-face with each other, in pseudo  $\beta$  or  $\gamma$  patterns, which have much better atomic contact between rings than that in benzene crystals. The centroid distances between two closest parallel rings in these pyridinium crystals are within  $3.77\text{-}4.83 \text{ \AA}$ , much smaller than that of benzene rings ( $5.37$

Å). Since little impact was made on the pyridiniums by the structures or sizes of the counterions, the packing patterns of these cations somewhat show the packing preference of these charged aromatic rings, which is isoelectronic to benzene. The enhanced  $\pi$ - $\pi$  versus CH- $\pi$  interaction was introduced by the delocalized charge of the pyridinium.

The crystal structures of TURPYB03 and UDETOM01 are two special examples with the simple cations. The counterions, Br<sup>-</sup> and I<sup>-</sup>, are small and simple. However, there are two medium size neutral compounds, thiourea or clathrates, in the unit cell. There is no strong hydrogen bond in the crystals because the Br and I atoms have less capability of forming hydrogen bonds. Without the disturbance of the hydrogen bonds, in both cases, the pyridinium were packed with **FFEC**, pseudo  $\gamma$  packing.

### 2.3.3.2 Large size counterions

There are four crystals with only pyridiniums and large size counterions as shown in Table 2.5. With the increase of counterion size, the packing pattern of the cation became less regular. In the crystal structure of PYRDHN,  $\gamma$  structure with **FFEC** packing was found due to the relatively smaller ( $\sim 2.1$  Å), flat NO<sub>3</sub><sup>-</sup> counterion. Compared with NO<sub>3</sub><sup>-</sup>, IO<sub>4</sub><sup>-</sup> is a bulky tetrahedron structure with  $\sim 2.9$  Å on each size, so the interaction between the pyridinium in the crystal structure of HOHMOG is weaker than that of PYRDHN. With larger counterions, the face-to-face packing pattern ( $\pi$ - $\pi$  interaction) is less favorable, as in the crystal structures of QOQVOH and RUVYIQ.

Table 2.5. Pyridinium crystals with larger size simple counterions

CSD code	HOHMOG01 HOHMOG05	PYRDHN	QOQVOH	RUVYIQ
counterions	IO <sub>4</sub> <sup>-</sup>	NO <sub>3</sub> <sup>-</sup>	CH <sub>3</sub> SO <sub>3</sub> <sup>-</sup>	CF <sub>3</sub> COO <sup>-</sup>
pattern	pseudo $\gamma$	pseudo $\gamma$	herringbone	herringbone
overlap	<b>FFEE-HH</b>	<b>FFEC</b>	NA	NA

The packing of the pyridinium is quite sensitive to the size of the counterions. With the increasing of the size of the counterions, chances are also increased that both

sides of the cation rings are occupied by the counterions, leaving no chance to the **FF** packing of the cations, such as in the cases of the  $\text{IO}_4^-$ ,  $\text{CH}_3\text{SO}_3^-$  and  $\text{CF}_3\text{CO}_2^-$ . When they are examined together with the small counterions capable of forming large structures due to the hydrogen bond (as in the crystal structures of JAVFUH and JAVFOB), the trend is clear: the bigger and bulkier the counterion, the worse the packing overlap.

### 2.3.3.3 Large size counterions with neutral molecules (protonated counterions)

Table 2.6. Pyridinium crystals with anions and neutral molecules (protonated anions)

CSD code	anion	packing type	ring overlap	structure type
AJEBIA		pseudo $\beta$	<b>FFEE</b>	NA
DUVLUB		pseudo $\beta$	<b>FFEC</b>	2D
DEFCUM		pseudo $\beta$	<b>FFEE-CH</b> ,	1D
IDAHOK		NA	NA	3D
KOWZUR		NA	NA	3D
KOXREU		NA	NA	3D
QAFFOS		pseudo $\gamma$	<b>FFEC</b>	2D
VEGKIB	$\text{H}_3\text{PO}_4$ , $\text{H}_2\text{PO}_4^-$	pseudo $\beta$	<b>FFEC</b> , dimer	3D
WADPEX		pseudo $\beta$	<b>FFEE-CC</b>	3D
XICBAM		NA	NA	3D

Some crystal structures have the pyridiniums crystallized with large size anions and neutral molecules (protonated anions). There are a total of ten: AJEBIA, DEFCUM, DUVLUB, IDAHOK, KOWZUR, KOXREU, QAFFOS, VEGKIB, WADPEX, and XICBAM, as shown in the Table 2.6. Since the numbers of the anions and neutral

protonated anions in unit cells are at least twice as much as the cations, there are chances that the cations could be separated and surrounded by anions and neutral molecules. Also, because the anion and neutral protonated anion can provide the hydrogen bond donor and acceptor, structures from 3D to 1D may be formed. All these crystals have been discussed in Section 2.3.1. The only one without the anion hydrogen bond structure was the crystal structure of AJEBIA, in which the anions were packed **FFEC** with its neutral protonated anion, and the cations were also packed **FFEC** with each other. This is probably because the anions form intramolecular hydrogen bonds inside the molecules.

From the discussion above, we find that except for those surrounded by the 3D counterion structures, the single pyridinium cations prefer face-to-face packing patterns, which have better atomic contact between aromatic rings than that of the isoelectronic benzene rings, which were packed in herringbone patterns. The size of the counterions is critical to the single ring pyridinium. It was a little complicated in the cases of pyridinium with aromatic counterions due to the  $\pi$ - $\pi$  interaction between cations and anions. However, if we consider the packing of cations and anions simultaneously, the packing patterns are much better compared with the neutral aromatic hydrocarbons.

## 2.4 Cations of naphthalene type aromatic systems (two-ring cations)

There are twelve crystals with naphthalene-type cations can be found in CSD. Nine of them have one nitrogen atom in each molecule. Four of these have the nitrogen atom in position 1; for the rest, it is in position 2. Three cations have two nitrogen atoms in a molecule. In QUOXPC, nitrogen atoms are on the 1, 4 positions, while in RUXQOQ and RUXQIK, they are on 2, 3 positions. The CSD codes, corresponding counterions, and packing styles of two-ring cations are shown in Table 2.7.

In Table 2.7, all of the two-ring pyridinium crystals used face-to-face packing patterns with the interplanar distances right around the  $\pi$ -stacking distance. Except for the cation of QUOXPC, which is packed **FFEE-CC** in the crystal, all two-ring cations adopted **FFEC** packing patterns. Most of them are  $\beta$  packing patterns.

Note: Start from here, all 'two-ring pyridinium-derived aromatic' will be simplified as 'two-ring', and so on, such as three-ring and four-ring, etc.

Table 2.7. CSD codes, corresponding counterions, packing patterns and the overlaps of two-ring pyridinium crystals. d is interplanar distance.

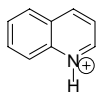
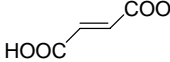
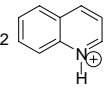
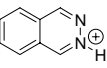
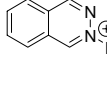
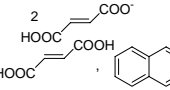
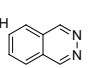
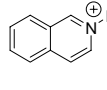
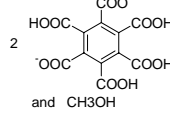
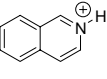
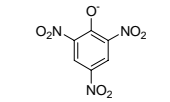
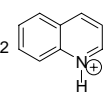
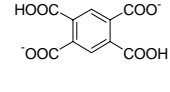
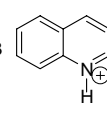
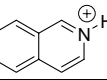
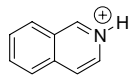
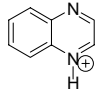
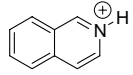
CSD code	cation	anion	cation packing type	ring overlap, %	d, Å
1D hydrogen bond dominated					
RABYID			pseudo $\gamma$	<b>FFEC</b> , 50%,	3.48
VAGDUD	2 	$\text{SiF}_6^{2-}$ , $\text{H}_2\text{O}$	pseudo $\beta$	<b>FFEC</b> , dimer, 50%	3.28
RUXQOQ		$\text{HOOC}-\text{COO}^-$	pseudo $\beta$	<b>FFEC</b> , dimer 16%	3.60
RUXQIK	2 	2  and 	pseudo $\beta$	<b>FFEC</b> , 50%	3.39
aromatic counterions					
BAYBEJ	2 	2  and $\text{CH}_3\text{OH}$	pseudo $\beta$ cation-cation	<b>FFEC</b> , 50%	3.29
JUSRUK			pseudo $\gamma$ cation-anion	<b>FFEC</b> , dimer	3.53
HEYQUX	2 		pseudo $\beta$ cation-cation	<b>FFEC</b> , 33%	3.51
simple counterions					
HEFZAT	3 	$\text{Cl}^-$ , $2\text{I}_3^-$	DHB	<b>FFEC</b> , dimer 50%	3.33
FOJWAC		$\text{NO}_3^-$	pseudo $\beta$	<b>FFEC</b> , 16%	3.46

Table 2.7 (continued)

IQUINC01		Cl <sup>-</sup>	pseudo $\beta$	<b>FFEC</b> , dimer 16%	3.40
QUOXPC		ClO <sub>4</sub> <sup>-</sup>	pseudo $\beta$	<b>FFEE-CC</b> dimer, 0%	3.36
IQUICM		Cl <sup>-</sup> , H <sub>2</sub> O	pseudo $\beta$	<b>FFEC</b> , dimer 50%	3.38

### 2.4.1 Hydrogen-bond structures of the counterions

There are five crystals with hydrogen bond structures formed by the counterions. These are shown in Table 2.8. Except the 3D structure formed by the aromatic counterion and methanol (BAYBEJ), all other crystals have 1D counterion structures. The  $\pi$ - $\pi$  interactions between cations are strong. All the cations were packed **FFEC**, in  $\beta$  or  $\gamma$  pattern. In the crystal structure of BAYBEJ, the aromatic counterion formed a 3D columnar structure with methanol, and the cations were packed **FFEC** inside the column, Figure 2.16. In all other crystals with 1D counterion, the preference of the **FFEC** packing patterns show the enhanced  $\pi$ - $\pi$  interaction between the two-ring cations compared with that of neutral naphthalene.

Table 2.8. Two-ring pyridinium crystals with hydrogen-bond structure of counterions

CSD code	RABYID	RUXQOQ	RUXQIK	VAGDUD	BAYBEJ
pattern	pseudo $\gamma$	pseudo $\beta$	pseudo $\beta$	pseudo $\beta$	pseudo $\beta$
overlap	<b>FFEC</b>	<b>FFEC</b>	<b>FFEC</b>	<b>FFEC</b>	<b>FFEC</b>

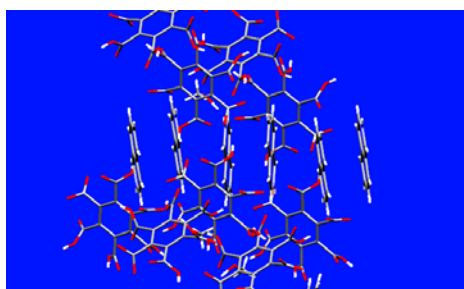


Figure 2.16. Packing pattern in BAYBEJ.

### 2.4.2 Aromatic counterions

There are three crystals that have aromatic counterions. They are shown in Table 2.9. The crystal structure of BAYBEJ, in which the cations packed **FFEC** in  $\beta$  style, has been discussed in the hydrogen bond structure section (Section 2.4.1). In the crystal structure of JUSRUK, the cations are packed **FFEC** with the aromatic counterion packed in a  $\gamma$  pattern. For HEYQUX, the cations packed **FFEC** in  $\beta$  pattern while the counterions packed in separated columns in the crystal. Similar to one-ring cations, the packing patterns of these two-ring pyridinium are much better than those of the neutral hydrocarbons if we consider the packing of cations and anions at the same time.

Table 2.9. Two-ring pyridinium crystals with aromatic counterions. Pattern 1 includes pyridinium only while pattern 2 includes all aromatic rings (pyridinium and counterion) inside the crystals.

CSD code	BAYBEJ	JUSRUK	HEYQUX
pattern 1	pseudo $\beta$	NA	pseudo $\beta$
overlap	<b>FFEC</b>	NA	<b>FFEC</b>
pattern 2	NA	pseudo $\gamma$ <b>FFEC, dimer</b>	pseudo $\gamma$

### 2.4.3 Simple counterions

The sizes of the simple counterions are somewhat less important to the two-ring systems, so all the simple counterions are listed and discussed together. The largest counterion is in the HEFZAT crystal, in which the size of the counterion is 5.8 Å.

From Table 2.10, except for HEFZAT and QUOXPC, all cations were packed face-to-face, edge-to-center in pseudo  $\beta$  pattern in crystals structures. The strong interactions between the charged aromatic faces were shown by this overlap and packing pattern preference. In the crystal structure of HEFZAT, the size of the counterion is 5.8 Å. This is almost the size of the diameter of naphthalene (6.4 Å). The large size of the



counterion probably contributes to the DHB packing pattern in this crystal. In QUOXPC crystal, there are two nitrogen atoms on the same ring of the cation. Less  $\pi$ - $\pi$  overlap of the cations in the crystal structure of QUOXPC may be due to the extra repulsion between the lone pair electron of the nitrogen atom and the  $\pi$  electrons of the other ring.

Table 2.10. Two-ring pyridinium crystals with simple counterions

CSD code	HEFZAT	FOJWAC	IQUICM	IQUINC01	QUOXPC
pattern	DHB	pseudo $\beta$	pseudo $\beta$	pseudo $\beta$	pseudo $\beta$
overlap	<b>FFEC</b> , dimer	<b>FFEC</b>	<b>FFEC</b>	<b>FFEC</b> , dimer	<b>FFEE-CC</b>

In the two-ring pyridinium crystals, most cations packed **FFEC** with  $\beta$  packing patterns. Compared with the single-ring cations, more overlap and better atomic contact between cationic rings show stronger interactions between these two-ring pyridiniums.

## 2.5 Cations of anthracene and phenanthrene type aromatic systems (three-ring cations)

For the fused three-ring cations, there are two kinds of the ring arrangement, anthracene and phenanthrene type, as shown in Figure 2.17. Twenty four crystals can be found from CCD. Two of them belong to anthracene type crystals, PABBEZ and EDVAVOU. Others are phenanthrene types. All phenanthrene types have two nitrogen atoms, three of which are dications (BEQXIE, DPPYAZ and PENPCM).

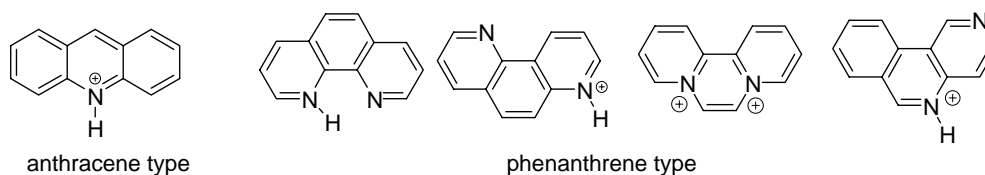


Figure 2.17. Three-ring cations.

All the CSD codes, corresponding counterions, and packing styles of three-ring cations are shown in Table 2.11.

Table 2.11. CSD codes, corresponding counterions, packing patterns, and overlaps of three-ring pyridinium crystals. Cat-cat is Cation-cation, d is interplanar distance.

CSD code	cation	anion	cation packing type,	cation ring overlap, %	d Å
aromatic counterions					
UNEBUK		 and 2 H <sub>2</sub> O	pseudo β, 3D counterion structure	<b>FFEC</b> , dimer, 22%	3.34
EDAVOU			pseudo β	<b>FFEC</b> , dimer 55%	3.48
OMIJAV	2		pseudo β	<b>FFEC</b> , dimer, 33%	3.55
PABBEZ			DHB	<b>FFEC</b> , dimer, 55%	3.47
simple counterions					
BEQXEA	2	$\text{ICl}_2^-$ , $\text{I}_2\text{Cl}^-$	pseudo γ	<b>FFEC</b> , dimer, 33%	3.58
BECPAA		 $\text{ClO}_4^-$	cation-neutral pseudo γ	<b>FFEC</b> , dimer, 33%	3.51
BIBROT		 $\text{H}_2\text{O}$ , $\text{NO}_3^-$	cation-neutral pseudo γ 1D counterion	<b>FFEC</b> , dimer, 55%	3.46
CUZDIK		$\text{Cl}^-$	pseudo β	<b>FFEC</b> , dimer, 55%	3.38
CUZFIM	3	$2\text{Cl}^-$ , $\text{HClCl}^-$ $\text{CHCl}_3$	pseudo γ	<b>FFEC</b> , dimer, 33%	3.48
MIYBOL		$\text{Br}^-$	pseudo β	<b>FFEE-CC</b> , 0%	3.31
NIDXUT		2 $\text{Cl}^-$	DHB cation-cation DHB cation-neutral	<b>FFEC</b> , dimer 33% cation-neutral <b>FF-33%</b>	3.50 3.55
NODZEL		 and 2H <sub>2</sub> O	pseudo β 2D counterion structure	<b>FFEC</b> , dimer 33%	3.42
NOXXIH		$\text{PF}_6^-$	pseudo β	<b>FFEC</b> , 11%	3.26

Table 2.11 (continued)

OPENDN		$\text{NO}_3^-$ $\text{HNO}_3$	pseudo $\gamma$	<b>FFEC</b> , dimer, 45%	3.40
PIDLET			cation-cation pseudo $\gamma$	<b>FFEC</b> , 22%	3.36
PHOLCL PHOLCL0 1		$\text{Cl}^-$ , $\text{H}_2\text{O}$	pseudo $\gamma$ 1D counterion structure	<b>FFEC</b> , dimer, 33%	3.39
TEPBIZ			cation-neutral pseudo $\gamma$	<b>FFEC</b> , dimer, 55%	3.64
TEPBOF			cation-neutral pseudo $\gamma$	<b>FFEC</b> , dimer, 55%	3.65
TIWFIO		$\text{Br}_3^-$	pseudo $\beta$	<b>FFEC</b> , dimer, 45%	3.49
XOHGOQ			pseudo $\beta$	<b>FFEC</b> , dimer, 45%	3.33
<b>di-cations</b>					
BEQXIE		$\text{Cl}^-$ , $\text{I}_2\text{Cl}^-$	pseudo $\beta$	<b>FFEC</b> , dimer, 11%	3.36
DPPYAZ		$2\text{Br}^-$ $\text{H}_2\text{O}$	pseudo $\beta$	<b>FFEC</b> , dimer, 11%	3.46
PENPCM		$2\text{ClO}_4^-$ $\text{H}_2\text{O}$	pseudo $\gamma$	<b>FFEC</b> , dimer, 11%	3.52

### 2.5.1 Aromatic counterions

Four crystals come with the aromatic counterions (Table 2.12). Two of them are anthracene-type cations. In the EDVAVOU crystal, the anion formed a linear 1D structure; the cations were connected through the hydrogen bond with the anion and packed **FFEC** in pseudo  $\beta$  pattern. In the crystal structure of PABBEZ, the cations formed **FFEC**-dimers, which packed with the aromatic counterions in herringbone-style. The aromatic counterions form a planar 2D structure through the hydrogen bond in the crystal of OMIJAV. The cations are packed face-to-face perpendicular to the plane in pseudo  $\beta$

pattern. In the last crystal, UNEBUK, there are two water molecules inside each unit cell and the counterions and waters form a 3D structure, which includes the two cations packed face-to-face with each other. If we consider the packing of cations and anions simultaneously, we see that face-to-face packing motif is preferred by these three-ring aromatics in the crystals with short interplanar distance and large overlap.

Table 2.12. Three-ring pyridinium crystals with aromatic counterions. Pattern 1 includes pyridinium only while pattern 2 includes all aromatic rings (pyridinium and counterion) inside the crystals.

CSD code	PABBEZ	EDAVOU	OMIJAV	UNEBUK
pattern 1	DHB	pseudo $\beta$	pseudo $\beta$	pseudo $\beta$
overlap	cation-cation <b>FFEC</b> , dimer	cation-cation <b>FFEC</b> , dimer	cation-cation <b>FFEC</b> , dimer	cation-cation dimer, <b>FFEC</b> . In 3D counterion structure
pattern 2	DHB	pseudo $\gamma$	NA	pseudo $\beta$

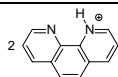
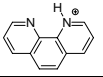
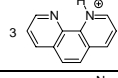
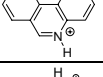
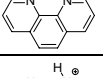
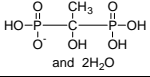
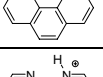
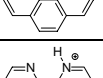
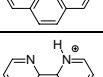
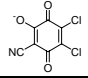
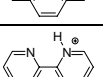
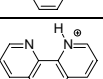

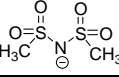
## 2.5.2 Simple counterions

All crystals with simple counterions are phenanthrene-type. Because some of the counterions co-crystallized with neutral aromatic rings, we will discuss this in two parts.

### 2.5.2.1 Simple nonaromatic counterions

There are twelve crystals that contain simple nonaromatic counterions as shown in Table 2.13. In all these three-ring cation crystals, cations are closely associated. They were packed as face-to-face dimers. There are three special crystal structures (NODZEL, PHOLCL, and PHOLCL01) in which the counterions formed 2D or 1D structures inside the crystals. In all these crystal structures, cations packed as dimers in **FFEC** style. Compared with the two-ring or one-ring pyridinium, the three-ring cations packed with more ring overlap. They stack despite large anions present in the lattice. For example, in the crystal structure of XOHGOQ, the size of the bulky anion is 6.1 Å, yet the cations were packed **FFEC** with 45% overlap in pseudo  $\beta$  style.

Table 2.13. Three-ring pyridinium crystals with simple nonaromatic counterions

CSD code	cation	counterions	pattern	cation-cation overlap
BEQXEA		$\text{ICl}_2^-$ , $\text{I}_2\text{Cl}^-$	pseudo $\gamma$	<b>FFEC</b> , dimer, 33%
CUZDIK		$\text{Cl}^-$	pseudo $\beta$	<b>FFEC</b> , dimer, 55%
CUZFIM		$2\text{Cl}^-$ , $\text{HCICl}^-$ $\text{CHCl}_3$	pseudo $\gamma$	<b>FFEC</b> , dimer, 33%
MIYBOL		$\text{Br}^-$	pseudo $\beta$	<b>FFEE-CC</b> , 0%
NODZEL		 and $2\text{H}_2\text{O}$	pseudo $\beta$ , 2D counterion structure	<b>FFEC</b> , dimer 33%
NOXXIH		$\text{PF}_6^-$	pseudo $\beta$	<b>FFEC</b> , 11%
OPENDN		$\text{NO}_3^-$ $\text{HNO}_3$	pseudo $\gamma$	<b>FFEC</b> , dimer, 45%
PIDLET			Cation-cation pseudo $\gamma$	<b>FFEC</b> , 22%
PHOLCL PHOLCL01		$\text{Cl}^-$ , $\text{H}_2\text{O}$	pseudo $\gamma$ , 1D counterion structure	<b>FFEC</b> , dimer, 33%
TIWFIO		$\text{Br}_3^-$	pseudo $\beta$	<b>FFEC</b> , dimer, 45%
XOHGOQ			pseudo $\beta$	<b>FFEC</b> , dimer, 45%

### 2.5.2.2 Simple nonaromatic counterions with neutral aromatic compounds

It was a little complicated in the cases of crystals containing simple nonaromatic counterions and neutral aromatic compounds. Due to the  $\pi$ - $\pi$  interactions between cations and neutral aromatic compounds, the cations have the chance to stack with the neutral rings. In all these crystals, cations-neutral aromatic rings packing patterns are preferred. As shown in Table 2.14, the cations packed face-to-face, edge-to-center with the neutral compounds with large overlap in pseudo  $\gamma$  or DHB style. It is probable due to the lone pairs of the nitrogen atoms on the neutral aromatic rings, which largely increase the exchange-repulsion between two aromatic rings. The cation-neutral packing patterns

alleviate these interactions. However, if we consider the packing of cations and anions simultaneously, the aromatic rings are packed with non-herringbone patterns. Large ring overlap and atomic contact between aromatic rings show stronger  $\pi$ - $\pi$  interactions compared with the corresponding aromatic hydrocarbons, which are packed with herringbone patterns and dominated by CH- $\pi$  interactions.

Table 2.14. Three-ring pyridinium crystals with simple nonaromatic counterions and neutral aromatic compounds

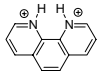
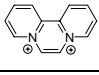
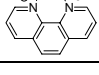
CSD code	cation	counterions	pattern	overlap
BECPAA			cation-neutral pseudo $\gamma$	<b>FFEC</b> , dimer, 33%
BIBROT			cation-neutral pseudo $\gamma$	<b>FFEC</b> , dimer, 55%
NIDXUT			cation-cation DHB cation-neutral DHB	<b>FFEC</b> , dimer, 33% <b>FF</b> -33%
TEPBIZ			cation-neutral pseudo $\gamma$	<b>FFEC</b> , dimer, 55%
TEPBOF			cation-neutral pseudo $\gamma$	<b>FFEC</b> , dimer, 55%

From all seventeen crystals of pyridinium with simple counterions, all cations packed with non-herringbone patterns either with cations or the neutral aromatic rings, which means that the  $\pi$ - $\pi$  interaction is preferred over the CH- $\pi$  interaction. The enhanced  $\pi$ - $\pi$  interaction is probably due to the cation- $\pi$  interaction.

### 2.5.3 Dications

There are three crystals formed by the dications. Two of them are 1,10-phenanthroline. The other one is 12,14-phenanthroline (crystal DPPYAZ). All of them crystallized with simple counterions. Compared with the single-charged cations, the di-cations have less overlap, which was probably due to the increased charge repulsion from the two di-cation rings.

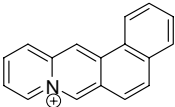
Table 2.15. Three rings dicationic pyridinium crystals

CSD code	cation	counterions	pattern	overlap
BEQXIE		Cl <sup>-</sup> , I <sub>2</sub> Cl <sup>-</sup>	pseudo β	<b>FFEC</b> , dimer, 11%
DPPYAZ		2Br <sup>-</sup> H <sub>2</sub> O	pseudo β	<b>FFEC</b> , dimer, 11%
PENPCM		2ClO <sub>4</sub> <sup>-</sup> H <sub>2</sub> O	pseudo γ	<b>FFEC</b> , dimer, 11%

## 2.6 Cations of benzanthracene type aromatic systems (four-ring cations).

Only one crystal, LUCGEV, has the fused four-ring cation. In this crystal, the counterion is a simple molecule and the cations were packed **FFEC** with 50% overlap in pseudo γ style. No crystal with more than four fused rings could be found.

Table 2.16. Four-ring pyridinium crystals

CSD code	cation	anion	cation packing type, ring overlap, %	d Å
LUCGEV		Br <sup>-</sup> CH <sub>3</sub> OH	pseudo γ <b>FFEC</b> , dimer, 50%	3.40

From the studies above of simple pyridinium-derived aromatic rings salts, we find that these aromatic cations prefer the face-to-face packing pattern; these non-herringbone patterns have more overlap and better atomic contact between cationic rings than their corresponding neutral polynuclear aromatic hydrocarbons, which are packed in herringbone patterns with no overlap between aromatic rings. These packing patterns of the pyridinium salts show stronger interactions between the aromatic pyridiniums rings. Except those that were separated by 3D counterion structures, the simple aromatic cations are packed face-to-face with aromatic rings (other cations or neutral aromatic compounds).

The size of the counterions is critical to the single-ring pyridinium, but it has somewhat less impact with the increase of the rings in cations. Though only a few

examples of the cations with more than three rings can be found, the trend of the packing of these cations is still clear: the more rings the cations have, the more overlap between the cations. This trend is similar to that of neutral aromatic hydrocarbons.<sup>(7)</sup>

It was a little complicated in the cases of pyridinium with aromatic counterions due to the  $\pi$ - $\pi$  interaction between cations and anions. For all crystals that have the aromatic counterions, only in three of them cation-anion  $\pi$ - $\pi$  interactions were preferred over the cation-cation  $\pi$ - $\pi$  interactions, as shown in Figure 2.18.

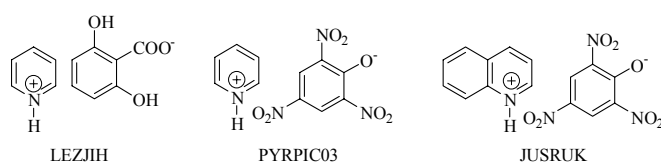


Figure 2.18. One- and two-ring pyridinium derivatives with **FF** cation-anion packing style in their crystal structures.

In these cases, the cations were formed face-to-face to the aromatic anions. All these anions had the hydroxyl groups. It is may be due to the resonance that partial negative charges were transferred to the aromatic ring. The strong aromatic-cation aromatic-anion interactions are formed between the aromatic cations and anions.

Other cases where the cation-cation face-to-face packing was not preferred only occurred in the three-ring phenanthrene-type crystals that contain two nitrogen atoms in an aromatic cation, as shown in Table 2.14. In these crystals, cations were co-crystallized with simple counterions and neutral aromatic rings. In the five crystals, cations packed face-to-face, edge-to-center with the neutral compounds with large overlap in pseudo  $\gamma$  or DHB style. The reason is unclear, perhaps because the lone pairs on the extra nitrogen atoms on the rings. However, if we consider the packing of cations and neutral rings at the same time, the packing patterns have better atomic contact compared with the corresponding aromatic hydrocarbon. All cations packed in either pseudo  $\gamma$  or pseudo  $\beta$  packing style with aromatic rings, which means that the  $\pi$ - $\pi$  interaction is preferred.



## 2.7 Delocalized cation enhanced cationic $\pi$ - $\pi$ interactions

### 2.7.1 Delocalized cation- $\pi$ interaction

In pyridinium rings, due to the delocalization of the pyridine aromatic ring, the positive charge will be distributed on the ring, basically at the hydrogen atoms.<sup>(44)</sup>

From the calculation of the benzene dimers, the stable dimers are **FF** and T-shape,<sup>(43)</sup> the distances of the centroids are shown below in Figure 2.19. Since the distance from the centroid of the benzene to the proton is  $\sim 2.5$  Å, in the T-shape dimer, the distance from the nearest proton of the perpendicular ring to the centroid of the oriental one is also around 2.5 Å.

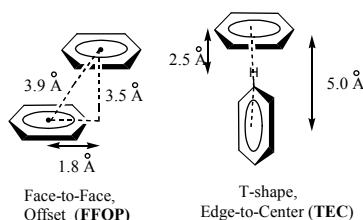


Figure 2.19. FF and T-shape packing of benzene dimers.

Due to the electrostatic nature of the cation- $\pi$  interactions, the coulombic potential functions can be used to describe the interactions, as shown in Equation 2.1. In the equation,  $Q = \pm ne$  ( $n$  is the number and  $e$  is the magnitude of the charges.  $e = 1.602 \times 10^{-19}$  C),  $r$  is the distance between the charges and  $\epsilon$  ( $= 8.854 \times 10^{-12}$  J<sup>-1</sup> C<sup>2</sup> m<sup>-1</sup>) is the dielectric constant.

$$U = \frac{Q_1 Q_2}{4 \pi \epsilon r}$$

Equation 2.1. Coulombic potential functions

Compared with the face-to-face packing, in T-shape packing, the distance is much shorter (2.5 Å versus 3.5 Å) from the proton of the perpendicular ring to the centroid of the oriental one (the other aromatic rings). A larger repulsive electrostatic

interaction may be formed between the positive portion of the ring (due to charge separation) and the positive charge on the hydrogen atom in the T-shape.

However, in the typical cation- $\pi$  interaction,  $\text{Na}^+$ ---benzene, the distance of the sodium cation to the centroid of the benzene is only 2.4 Å.<sup>(45)</sup> This is shorter than the 2.5 Å and the total charge (+1) should be bigger than that on the proton of the ring. So, the repulsive electrostatic interaction between the positive charge on the proton and the positive portion of the other ring (due to charge separation) could not be responsible for the preferring of the **FF** over the T-shape packing.

For the typical cation- $\pi$  interaction, the best position for the cation is on the top of the ring center, with the electrostatic interaction playing a prominent role. The electrostatic model for the benzene<sup>(36)</sup> can be used to explain the delocalized cation- $\pi$  interaction. Due to the orientation of the charge of the rings, the **FF** and T-shape packing are two optimum geometries for best  $\sigma$ - $\pi$  attractive interactions. Those will be the same choices for the electrostatic interaction between two charged rings. However, no T-shape has ever been found in the pyridinium cation crystals.

From the calculation, the stable benzene dimers are **FF** and T-shape,<sup>(43)</sup> the distances of the T-shape centroids is 5 Å and the face-face distance for the **FF** is 3.5 Å. Suppose the pyridine ring can be viewed as an electrostatic model like a benzene ring. This means the  $\pi$ -system can be viewed as a sandwich structure with a positively charged  $\sigma$ -framework in the middle and two half negatively charged  $\pi$ -electron clouds on both sides,<sup>(32)</sup> as shown in Figure 2.20.

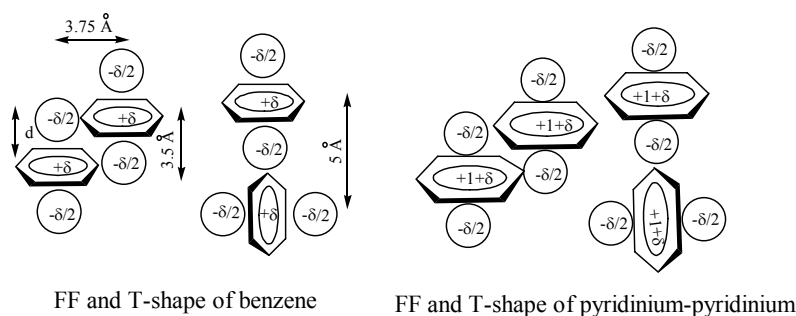


Figure 2.20. Electrostatic model of pyridinium rings.

### 2.7.2 Assumptions for the calculation

- 1) The pyridinium rings will use the same **FFEC** or **EF** (T-shape) packing patterns as benzene rings.
- 2) The pyridinium rings can be viewed as an electrostatic model like benzene rings.
- 3) The charge on the pyridinium can be treated as a single-point charge and will not affect other interactions.

The repulsion interactions between the two pyridinium rings include the exchange repulsion of the rings ( $+\delta$ ,  $+\delta$ ), the coulombic repulsion of positive charges ( $+1$ ,  $+1$ ) and repulsions between charges and rings ( $+\delta$ ,  $+1$ ). In the **FF** and **EF** patterns, the former repulsion is comparable to the charge repulsion in the **FF** and **EF** benzene model, in which the **FF** model is 1.19 kcal/mol higher than that of the **EF** model. This difference is covered by the higher dispersion attraction of **FF** model ( Table 2.17).<sup>(43)</sup>

Table 2.17. Electrostatic and dispersion energies of benzene<sup>(43)</sup>.  $E_{es}$  is electrostatic interaction energies,  $E_{rep}$  is repulsion interaction energies, and  $E_{corr}$  is correlation interaction energies.

energy, kcal/mol	<b>FFCC</b>	<b>EF</b>	<b>FFEC</b>
$E_{total}$	-1.48	-2.46	-2.48
$E_{es}$	1.24	-0.55	0.90
$E_{rep}$	3.02	1.57	2.76
$E_{corr}$	-5.74	-3.48	-6.14

Suppose the positive charges can be treated as point charge and set at the center of the rings. In Figure 2.20, the centroids of the **FFEC** and **EF** are 3.94 Å and 5 Å. According to Equation 2.1, the interaction of the coulombic repulsion between positive charges in **FFEC** can be 1.3 times that of the **EF** model. It will be the same for the repulsions between charges and rings ( $+\delta$ ,  $+1$ ).

Since there is no **EF** pattern in the pyridinium crystals, the extra coulombic repulsion between positive charges in **FFEC** must be covered by some kind of attraction.

As shown in Figure 2.20, two coulombic interactions between a positive charge and a  $-\delta/2$  charge can be found in the face-to-face **FF** pyridinium packing, while only one of this kind of interaction can be found in the T-shape edge-to-face(**EF**) pyridinium packing. Compared with the **EF** packing pattern, the **FF** pattern has twice the chance to obtain coulombic interaction.

Moreover, the **FF** pattern is more flexible than the T-shape; the charged rings can slide easily to get the best interaction. A larger net attraction can be gained to cover the charge repulsion. This could be the reason for the preference of **FF** over T-shape style. The net gaining between the cation- $\pi$  electrostatic attraction and the charge-charge electrostatic repulsion in the **FF** packing is greater than that of the T-shape one.

This model can also explain the trend of the packing of cations: the more rings the cations have, the more overlap between the rings. This is because the larger the aromatic rings, the larger cation- $\pi$  interaction ( $q_2$  will be larger in Equation 2.1).

From the study, we can see that the **FF** packing of the pyridinium rings is due to the cation- $\pi$  interactions, which are dominant in the orientation and stabilization of the packing. Besides cation- $\pi$  interactions, other interactions also need to be considered for the aromatic-aromatic ring interactions of the pyridinium cations.

### 2.7.3 Dipole-dipole interaction

Dipole-dipole interactions may also contribute to the packing patterns of pyridinium rings. Due to the different electronegativities of N and C atoms, the dipole moment exists on the pyridinium rings, which is 1.97 D and points to the nitrogen atom according to the calculation.<sup>(39)</sup> This value is comparable to that of the CH<sub>3</sub>Cl. However, the dipole-dipole forces may not be dominating, because:

1) There are many different kinds of orientation of the cation rings inside the crystals. However, there is no overlap or face-to-face packing among nitrogen atoms in the packing patterns in order to avoid the direct dipole moment confrontation. Nevertheless, the dipole-dipole forces could not be the major forces determining the

packing patterns. If so, the orientation of all crystals would be similar. However, there are many kinds of orientations in the pyridinium crystals. Some of them are shown in Figure 2.21, in which the aromatic rings are simplified. Only the backbones are shown.

2) Compared with the ion-dipole and cation- $\pi$  interactions, which also exist in the crystals, the dipole-dipole forces, which are normally only a few kcal/mol, is much smaller, *e.g.*, only 0.79 kcal/mol for the HCl molecules.

3) The dipole-dipole interactions in the pyridinium ring more or less determine the orientation of the rings inside the packing structure of the crystals, but not the packing patterns.

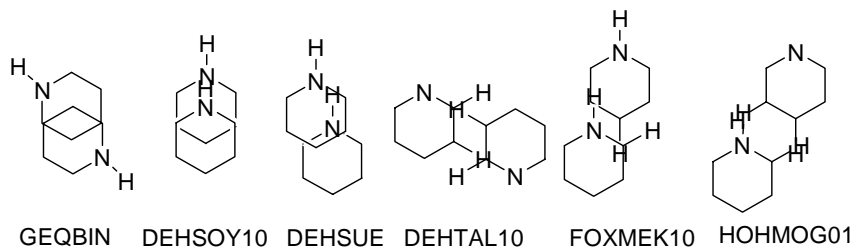


Fig 2.21. Orientation of the cationic rings.

#### 2.7.4 Ion-dipole interaction

The ion-dipole interaction is also involved in the packings of the aromatic cations. Like the dipole-dipole forces, the ion-dipole interaction has the orientation preference and short distance requirement.

1) Anion-dipole interaction. The anion here is the anion part from the charge-separation model. As shown in Figure 2.20, the **FF** packing style will provide two anion-dipole interactions, while T-shape can only obtain one. However, in either the **FF** or the T-shape, the ion dipole interaction is much smaller than the cation- $\pi$  interaction between two rings, which is charge-charge interaction in nature. The dipole moment is only partial charge separation.

2) Cation-dipole interaction. None of the two packing styles show good interaction of the cation-dipole interaction of one ring to the other. The best of this kind of interaction requires the close arrangement of the rings in the same plane inside the crystals, which does not happen in the pyridinium crystals.

Also, from Figure 2.21, the orientations of the dipole moments are different for the cation rings. Some of them are far away from the direction of best anion-dipole interaction; a few of them are in the reverse direction. These orientations show relatively unimportant contributions of the ion-dipole interactions to the crystal packing patterns.

### 2.7.5 Molecular orbital study

Maxima molecular orbital overlaps of the aromatic cations could happen in the FF packing ( $\pi$ -stacking). Since the molecules possess both empty orbitals and  $\pi$  bonds, they can be electronic donors and acceptors at the same time. They are capable of forming strong donor-acceptor interactions of the cation- $\pi$  type. Strong interactions may result from the overlap of these charged aromatic species. Possible interactions between these cationic- $\pi$ -systems are through back-bonding interactions, as shown in Figure 2.22. One pyridinium (**A**) donates electrons from its highest occupied molecular orbital (HOMO) to the lowest unoccupied molecular orbital (LUMO) of the other one (**B**) to form a bonding molecular orbital (MO). However, the HOMO of **B** will also overlap with the LUMO of **A**. They too will form a net bonding MO. **B** will donate electrons to **A**. New molecular orbitals formed through back-bonding will result in strong interactions between the cations, which overcome the charge/charge interactions.

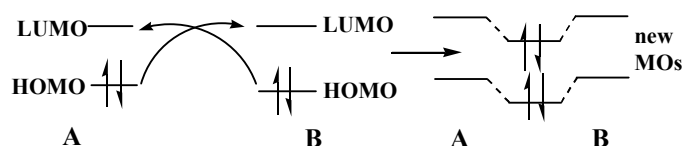


Fig 2.22. Back-bonding interactions between two cationic- $\pi$ -systems.

## 2.8 Conclusion

1) The stacking interactions between aromatic rings of pyridinium cations are greatly enhanced over their corresponding neutral polynuclear aromatic hydrocarbons. The  $\pi$ -stackings shown by the better atomic contact and overlap of the pyridinium cations were probably introduced by the delocalized charges of cations. Except for those pyridinium with bulky counterions, the centroid distances between two closest parallel rings in the pyridinium crystals are within 3.77-4.83 Å, which are much smaller than that of benzene rings (5.37 Å). Cation- $\pi$  interaction could be formed between the delocalized charge of one ring and the  $\pi$ -system of the other ring.

2) The face-to-face packing patterns could get the maximum delocalized cation- $\pi$  interaction for both rings and minimize the system energy. The model of regular point cation- $\pi$  interaction can be used to explain the delocalized cation- $\pi$  interaction. Stacking pattern of aromatic systems could introduce strong cation- $\pi$  interactions. The cation- $\pi$  interaction is dominant in the orientation and stabilization of the packing of pyridinium rings.

3) The dipole-dipole, ion-dipole interactions in the pyridinium ring affect the orientation of the rings inside the packing structure of the crystals, but are not strong enough to determine the packing pattern.

4) The trend of the packing of these cations is: the more rings the cations have, the more overlap between the cations. This is probably because larger systems could alleviate the charge repulsions better and also have larger cation- $\pi$  interactions.

5) The maxima overlap of molecular orbitals of the aromatic cations could happen in the **FF** packing. This may contribute to the enhanced cationic  $\pi$ - $\pi$  interactions.

The cationic  $\pi$ - $\pi$  interactions were greatly enhanced by the delocalized cation- $\pi$  interactions. What will happen if two aromatic rings carried different sign of charges? How will the delocalized cation-anion interactions affect the  $\pi$ - $\pi$  interactions? These questions are examined in the next chapter.

## References

- 1) M. Brandl, M. S. Weiss, A. Jabs, J. Syhnel, R. Hilgenfeld, *J. Mol. Biol.* **2001**, *307*, 357-377.
- 2) Y. Umezawa, S. Tsuboyama, H. Takahashi, J. Uzawa, M. Nishio, *Bioorg. Med. Chem.* **1999**, *7*, 2021-2026.
- 3) M. Nishio, *Cryst. Eng. Comm.* **2004**, *6*, 130-158.
- 4) S. Tsuzuki, K. Honda, T. Uchimaru, M. Mikami, K. Tanabe, *J. Am. Chem. Soc.* **2000**, *122*, 3746-3753.
- 5) G.R. Desiraju, *J. Mol. Struct.* **2003**, *656*, 5-15.
- 6) G. R. Desiraju, A. Gavezzotti, *Acta Cryst.* **1989**, *B45*, 473-482.
- 7) E. A. Meyer, R. K. Castellano, F. Diederich. *Angew. Chem. Int. Ed.* **2003**, *42*, 1210-1250.
- 8) G. R. Desiraju, A. Gavezzotti, *Acta Cryst.* **1988**, *B44*, 427-434.
- 9) H. M. Berman, T. Battistuz, T. N. Bhat, W. F. Bluhm, P. E. Bourne, K. Burkhardt, Z. Feng, G. L. Gilliland, L. Iype, S. Jain, P. Fagan, J. Marvin, D. Padilla, V. Ravichandran, B. Schneider, N. Thanki, H. Weissig, J. D. Westbrook, C. Zardecki, *Acta Cryst.* **2002**, *D58*, 899-907.
- 10) R. Taylor, *Acta Cryst.* **2002**, *D58*, 879-888.
- 11) F. H. Allen, *Acta Cryst.* **2002**, *B58*, 380-388.
- 12) I. J. Bruno, J. C. Cole, P. R. Edgington, M. Kessler, C. F. Macrae, P. McCabe, J. Pearson, R. Taylor, *Acta Cryst.* **2002**, *B58*, 389-397.
- 13) G. A. Jeffrey, An Introduction to Hydrogen Bonding, Oxford University Press, New York, 1997.
- 14) G. A. Jeffrey, W. Saenger, Hydrogen Bonding in Biological Structures, Springer, Berlin, 1991.
- 15) G. R. Desiraju, T. Steiner, The Weak Hydrogen Bond, Oxford University Press, New York, 1999.
- 16) R. Taylor, O. Kennard, *J. Am. Chem. Soc.* **1982**, *104*, 5063-5070.



- 17) Z. S. Derewenda, L. Lee, U. Derewenda, *J. Mol. Biol.* **1995**, *252*, 248-262.
- 18) G. R. Desiraju, *Acc. Chem. Res.* **1996**, *29*, 441-449.
- 19) Y. Mandel-Gutfreund, H. Margalit, R. L. Jernigan, V. B. Zhurkin, *J. Mol. Biol.* **1998**, *277*, 1129-1140.
- 20) G. R. Desiraju, *Acc. Chem. Res.* **2002**, *35*, 565-573.
- 21) G. R. Desiraju, A. Gavezzotti, *J. Chem. Soc., Chem. Comm.* **1989**, 621-623.
- 22) I. Andre, C. Foces-Foces, F. H. Cano, M. Martinez-Ripoll, *Acta Cryst.* **1997**, *B53*, 984-995.
- 23) I. Andre, C. Foces-Foces, F. H. Cano, M. Martinez-Ripoll, *Acta Cryst.* **1997**, *B53*, 996-1005.
- 24) A. M. de Vos, M. Ultsch, A. A. Kossiakoff, *Science* **1992**, *255*, 306-312.
- 25) J. B. O. Mitchell, C. L. Nandi, I. K. McDonald, J. M. Thornton, S. L. Price, *J. Mol. Biol.* **1994**, *239*, 315-331.
- 26) S. Karlin, M. Zuker, L. Brocchieri, *J. Mol. Biol.* **1994**, *239*, 227-248.
- 27) S. Mecozzi, A. P. West, D. A. Dougherty, *J. Am. Chem. Soc.* **1996**, *118*, 2307-2308.
- 28) O. Livnah, E. A. Stura, D. L. Johnson, S. A. Middleton, L. S. Mulcahy, N. C. Wrighton, W. J. Dower, L. K. Jolliffe, I. A. Wilson, *Science* **1996**, *273*, 464-471.
- 29) J. C. Ma, D. A. Dougherty, *Chem. Rev.* **1997**, *97*, 1303-324.
- 30) J. P. Gallivan, D. A. Dougherty, *J. Am. Chem. Soc.* **2000**, *122*, 870-874.
- 31) W. L. Zhu, X. J. Tan, C. M. Pua, J. Gu, H. Jiang, K. Chen, C. E. Felder, I. Silman, J. L. Sussman, *J. Phys. Chem. A* **2000**, *104*, 9573-9580.
- 32) S. Tsuzuki, M. Yoshida, T. Uchimar, M. Mikami, *J. Phys. Chem. A* **2001**, *105*, 769-773.
- 33) D. A. Dougherty, H. A. Lester, *Nature* **2001**, *411*, 252-254.
- 34) K. Brejc, W. J. Dijk, R. V. Klaassen, M. Schuurmans, J. Oost, A. B. Smit, T. K. Sixma, *Nature* **2001**, *411*, 269-276.
- 35) J. Sunner, K. Nishizawa, P. Kebarle, *J. Phys. Chem.* **1981**, *85*, 1814-1820.

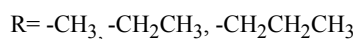
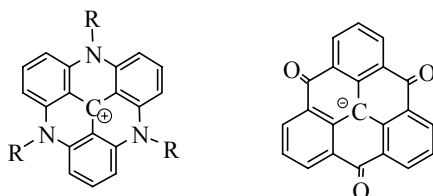
- 36) C. A. Hunter, J. K. M. Sanders, *J. Am. Chem. Soc.* **1990**, 5525-5534.
- 37) C. Janiak, *J. Chem. Soc., Dalton Trans.* **2000**, 3885-3896.
- 38) T. Ishida, M. Shibata, K. Fujii, M. Inoue, *Biochemistry* **1983**, 22, 3571-3581.
- 39) H. Maluszynskal, C. Scherf, P. Czarneckil, A. Cousson, *J. Phys.: Condens. Matter.* **2003**, 15, 5663-5674.
- 40) X. Ren, J. Xie, Y. Chen, R. K. Kremer, *J. Mol. Struct.* **2003**, 660, 139-146.
- 41) J. A. Ripmeester, *J. Chem. Phys.* **1986**, 85, 747-750.
- 42) C. B. Aakeroy, *Acta Cryst.* **1997**, B53, 569-586.
- 43) S. Tsuzuki, K. Honda, T. Uchimaru, M. Mikami, K. Tanabe, *J. Am. Chem. Soc.* **2002**, 124, 104-112.
- 44) J. N. Latosinska, A. Pajzderska, J. Wasicki, *J. Mol. Struct.* **2004**, 701, 105-109.
- 45) D. A. Dougherty, *Science* **1996**, 271, 163-168.

### Chapter Three

#### $\pi$ - $\pi$ interaction in the solid state of triangulene salt pairs

Aromatic salt pairs of triangulene derivative with the delocalized cation-anion interaction were synthesized. The  $\pi$ - $\pi$  interactions of these salts were studied. Stacking interactions are very strong between these charged aromatic salts, evident by the large ring overlaps, short interplanar distances and high melting points. The strong interaction between the salt  $\pi$  system pair is dominated by the coulombic attraction, which is synergistic with the cation- $\pi$  interaction. The stacking pattern and strong interactions between the charged aromatic ions can also be explained by the interactions between these two charged species.

This contribution is novel because these are the only fused, flat, aromatic salt pairs in the chemical literature. It is the first time to discuss the effect of delocalized cation-anion interactions on  $\pi$ - $\pi$  interactions.



### 3.1 Introduction

#### 3.1.1 Fused, flat, benzenoid hydrocarbons with $D_{3h}$ symmetry

The total-resonant-sextet (TRS) benzenoids are benzenoid hydrocarbons, which have  $6n$  carbons ( $6n$   $\pi$  electrons) and are totally built by Clar  $\pi$ -sextets: single benzene rings that are separated from each other by carbon-carbon single bonds. These systems are very stable.<sup>(1-3)</sup>

The total-resonant-sextet (TRS) series and benzenoid polyradical series (triangulene type) are the only two kinds of fused, flat, benzenoid hydrocarbons with  $D_{3h}$  symmetry, (Figure 3.1). The TRS are the most stable systems, while the polyradical series are the most unstable.<sup>(4)</sup>

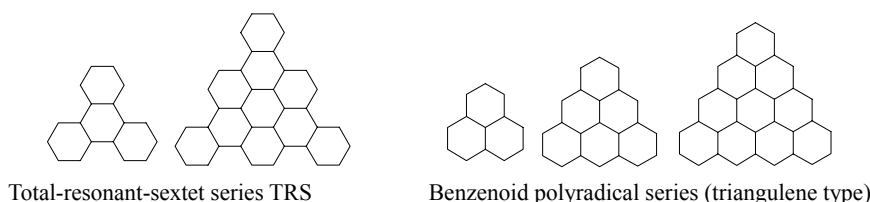


Figure 3.1. The total-resonant-sextet (TRS) series and benzenoid polyradical series (triangulene type) benzenoid hydrocarbons.

Many derivatives of these two series have attracted scientific interest due to their highly conjugated  $\pi$  system and their propensity to form organized one-dimensional columns. Triphenylene derivatives and some hetero-triangulenes have been used as the central discotic cores in discotic liquid crystals.<sup>(6,7)</sup> Discotic liquid crystals have remarkable charge transport properties and have started to be used as optoelectronic devices.<sup>(8)</sup>

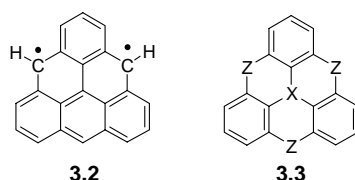


Figure 3.2. Triangulene **3.2** and triangulene skeleton.

According to Hückel molecular orbital calculations, triangulene **3.2** (Figure 3.2) has two unpaired electrons that are distributed on two degenerate nondisjoint nonbonding MOs. It will show a triplet ground state.<sup>(9)</sup> Although attempted synthesis of this non-Kekulé molecule started in the early 1950's by Clar and his co-worker, its successful isolation and characterization have not yet been reported.<sup>(10)</sup>

Triangulene skeleton **3.3** is shown in Figure 3.2. Many triangulene derivatives have been synthesized by replacing some of the  $sp^2$  carbon atoms (X and Z) in **3.3** with heteroatoms.<sup>(11-18)</sup> These derivatives can be separated into three types based on the charges they carry: anion, cation, and neutral, as shown in Figure 3.3.

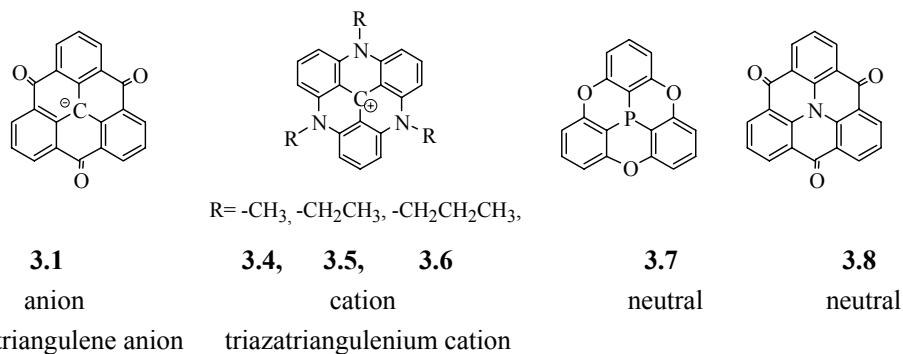


Figure 3.3. Derivatives of triangulene.

The trioxytriangulene anion **3.1** is the only triangulene-type anion that has been reported. The first successfully detected triplet triangulene diradical (**3.9**) was reported by Bushby and co-workers. Compound **3.1** is the precursor.<sup>(11)</sup> One-electron reduction of trioxytriangulene **3.1** anion under vacuum with Na-K alloy in DMF solution gave the stable triangulene diradical **3.9**, which showed the triplet ESR spectrum (Figure 3.4).

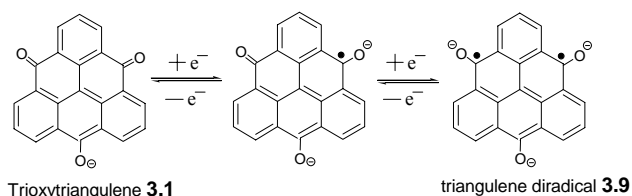


Figure 3.4. Electron reduction of trioxytriangulene **3.1**.

The interest in synthesis of the neutral triangulenes (**3.7**, **3.8**) mainly comes from their high molecular symmetry ( $C_{3v}$  and  $D_{3h}$ ), which is important for achieving high molecular packing ordering in the solid state.<sup>(12-15)</sup>

Structure **3.4** is a very stable molecule, which was shown by its extraordinary  $pK_{R^+}$  value. The  $pK_{R^+}$  values are calculated according to Equation 3.1. When the cation is titrated in basic solutions, the stability of the cation is expressed by the affinity of the carbenium ion toward hydroxide ions.

$$pK_{R^+} = pH + \log \frac{[R^+]}{[ROH]} \dots\dots (1)$$

Equation 3.1.  $pK_{R^+}$  equation.

The  $[R^+]/[ROH]$  is the [carbinol]/[carbenium] ratio in the solution. From Equation 3.1, the  $pK_{R^+}$  is the pH value of the solution when the concentrations of the carbinol and carbenium are equal in the solution.

The  $pK_{R^+}$  value of the trimethyltriazatriangulenium ion **3.4** was  $23.7 \pm 0.2$ , which places the trimethyltriazatriangulenium ion **3.4** among one of the most stable carbenium ions.<sup>(16,17)</sup> The most stable carbenium ions known to date are tris[6-(dimethylamino)-1-azulenyl]methyl hexafluorophosphate (**A**) and bis[6-(dimethylamino)-1-azulenyl] [6-(dimethylamino)phenyl]methyl hexafluorophosphate (**B**) (see Figure 3.5), which have  $pK_{R^+}$  values of  $24.3 \pm 0.3$  and  $21.5 \pm 0.2$ .<sup>(18)</sup> The stabilization of the **A** and **B** were attributed to the delocalization of the charge by the effects of resonance and the three amino groups, as shown in Figure 3.5. These should have similar effects on the stabilization of **3.4**, **3.5**, and **3.6**.

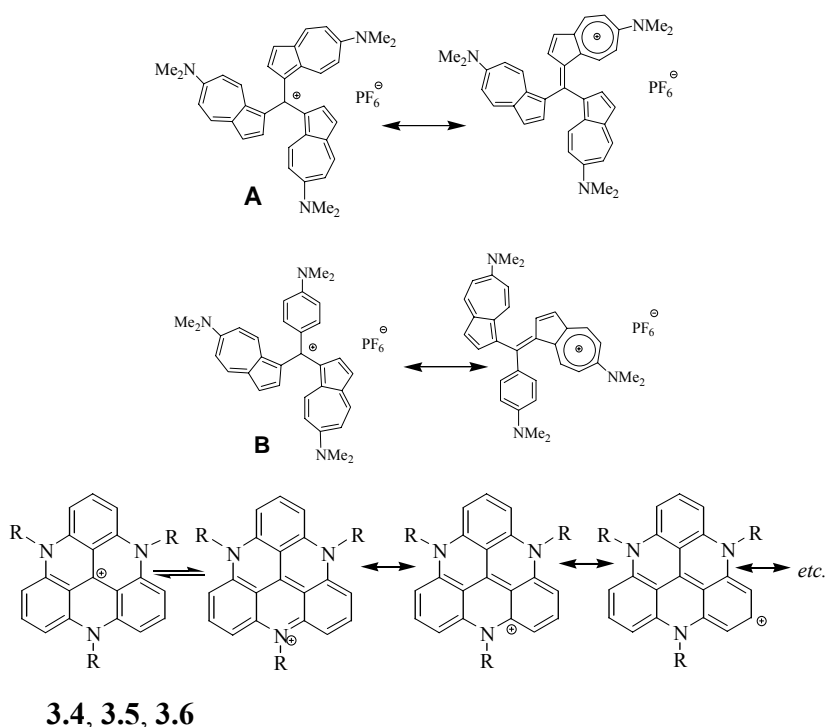


Figure 3.5. Delocalization of the charge by resonance of **3.4**, **3.5**, **3.6**, **A**, and **B**.

### 3.1.2 Triangulene type cations and anions

The total-resonant-sextet (TRS) series and benzenoid polyradical series (triangulene type) are the only two kinds of fused, flat, benzenoid hydrocarbons with  $D_{3h}$  symmetry. They have highly conjugated  $\pi$  systems and the ability of forming organized one-dimensional columns.<sup>(19)</sup> The aromatic ions of such  $D_{3h}$  symmetric and planar fused benzenoid hydrocarbon rings are difficult to prepare. No such kinds of hydrocarbon ions have been reported. All the ions reported to date are triangulene types.<sup>(10,16,17)</sup> Triazatriangulenium ions are the pyridinium type of triangulene cations. The trioxytriangulene anion is the only triangulene type anion that has been synthesized. The crystals of triazatriangulenium trioxytriangulene (**3.14**, **3.15**, and **3.16**) salt pairs were investigated as the delocalized cation-anion interaction models in my study (Figure 3.6).

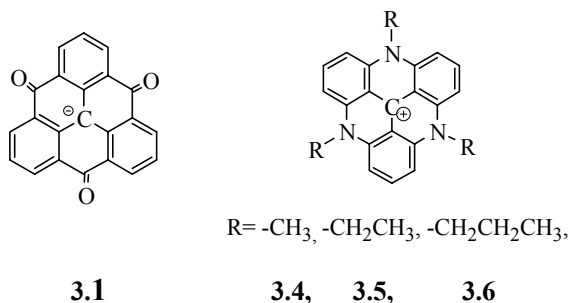


Figure 3.6: Triangulene type cations and anions.

### 3.1.3 Cation- $\pi$ interaction and cationic $\pi$ - $\pi$ interaction

Cation- $\pi$  interaction and cationic  $\pi$ - $\pi$  interaction have been discussed in Chapter 2 (see section 2.1.4 and 2.7). In the latter section of Chapter 2, there was evidence for strong interaction between aromatic cations. This was framed in terms of charge-enhanced  $\pi$ -stacking. Many of the cations stacked in a pair-wise manner. It was hypothesized that analogous species molecules of opposite charge would be more strongly cohesive than the cation pairs. The work below supports this hypothesis.

## 3.2 Solid-state study of triangulene salt pairs

### 3.2.1 Solid-state study of salts of triangulene cation and nonaromatic counterion

The triangulene cations studied are trimethyl-, triethyl-, and tripropyltriazatriangulenium. The trimethyl- and tripropyltriazatriangulenium are known compounds and were prepared according to reference 17. The triethyltriazatriangulenium was also prepared. The triazatrianguleniums and counterions are shown in Figure 3.7. The crystals are trimethyltriazatriangulenium hexafluorophosphate (**3.4C**), trimethyltriazatriangulenium tetrafluoroborate (**3.5D**), and tripropyltriazatriangulenium tetrafluoroborate (**3.6D**). The packing patterns of the cations are shown in Figure 3.8. The centroid distances and overlaps of these crystals are listed in Table 3.1.



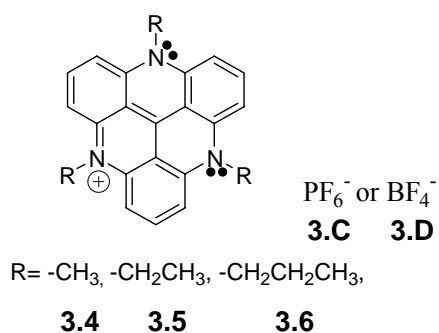


Figure 3.7: Triazatrianguleniums, counterions and their corresponding code.

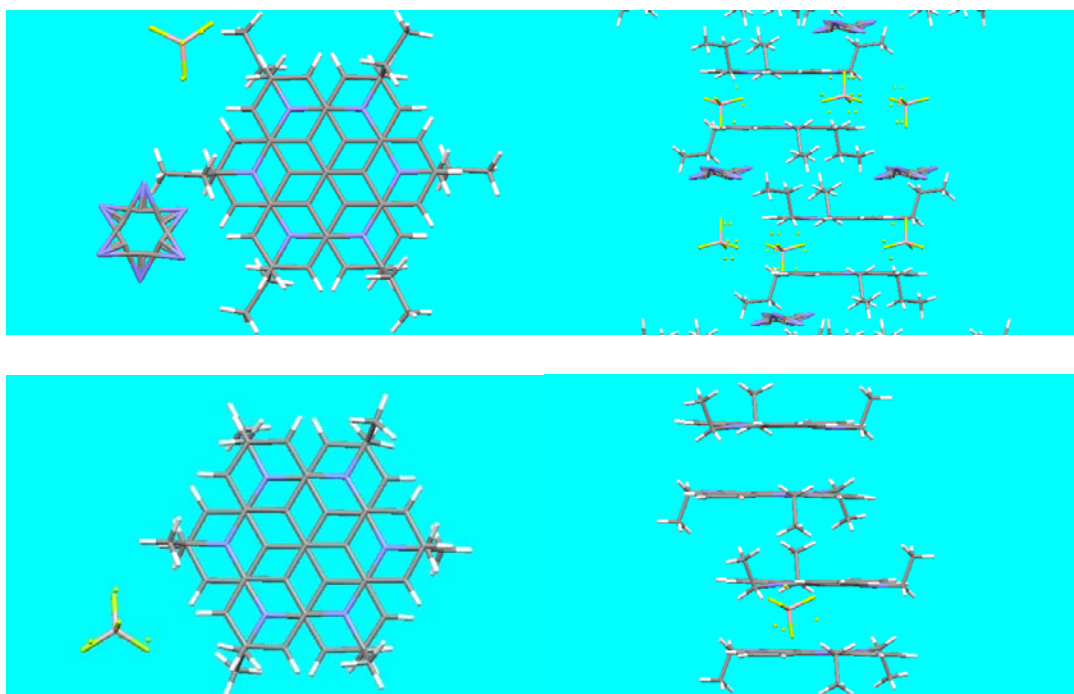
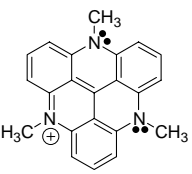
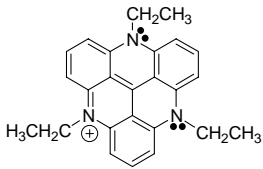
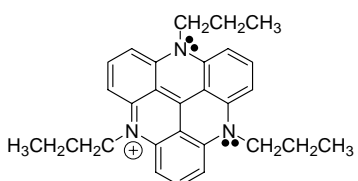


Figure 3.8: Tripropyl- (top) and triethyl- (bottom) triangulene cations viewed from *a* axis (left) and their packing patterns.

From Figure 3.8, we find that the cations of the tripropyl- and trimethyltriangulene are packed face-to-face, center-to-center in a staggered dimer form, which pushes propyl groups on the rings away from the dimers. The crystal structure of trimethyltriangulene cannot be elucidated because of the disorder in the molecule.<sup>(16,17)</sup> The packing patterns and centroid distances of aromatic rings between dimers

(inter-dimer) are different from that inside dimers (intra-dimer). In Table 3.1, in the column labeled ring overlap, the first row for each salt outlines intra-dimer packing style and overlap, while the second row includes the information of inter-dimer. As shown in Figure 3.8, the cations are staggered, with approximate 66% overlap, which is the best overlap in all the cationic crystals we studied (overlap percentages are calculated based on the ratio of overlap areas to total aromatic rings). The distance between two **FFCC** dimers is very short, 3.29 Å. The short distance and large overlap show the strong  $\pi$ - $\pi$  interaction between cations.

Table 3.1: Triazatriangulenium crystals

Cation	Anion	Cation-cation packing type,	Ring overlap, %	d, Å
	PF <sub>6</sub> <sup>-</sup>	NA	NA	NA
			NA	NA
	BF <sub>4</sub> <sup>-</sup>	Pseudo $\beta$	<b>FFCC</b> , dimer 66%	3.29
			<b>FFEC</b> 28%	4.32
	BF <sub>4</sub> <sup>-</sup>	Pseudo $\beta$	<b>FFCC</b> , dimer, 66%	3.29
			<b>FFEE-CC</b> 0%	5.37.

Substituents on the nitrogen atoms change the distances between dimers (inter-dimer distances). The inter-dimer distance of trimethyltriazatriangulenium in **3.5D** is much smaller than the inter-dimer distance of the tripropyltriazatriangulenium in **3.6D**. This is due to steric hindrance from the alkanes on the nitrogen atoms. This steric hindrance is also evident in the longer distance between two octyltriangulenium dimers,

which is 11.5 Å.<sup>(16,17)</sup> The steric hindrances prevent close packing between cationic dimers. The smaller the alkyl group, the less steric hindrance there will be. So, the more overlap can occur and the packing between dimers will be closer. This steric hindrance will be minimized in trimethyltriazatriangulenium (**3.4C**). There will be no difference between two faces of the cation. From the trend of the packing patterns of these cations with different substituents, we can predict that the packing pattern of trimethyltriazatriangulenium in **3.4C** will be columns built by staggered **FFCC** dimers. These dimers could be packed from direct face-to-face, center-to-center (left bottom in Figure 3.9) to swirl face-to-face, center-to-center (right bottom in Figure 3.9). Inside each column, all cations will be packed center-to-center with each other with approximately 66% overlap (Figure 3.9).

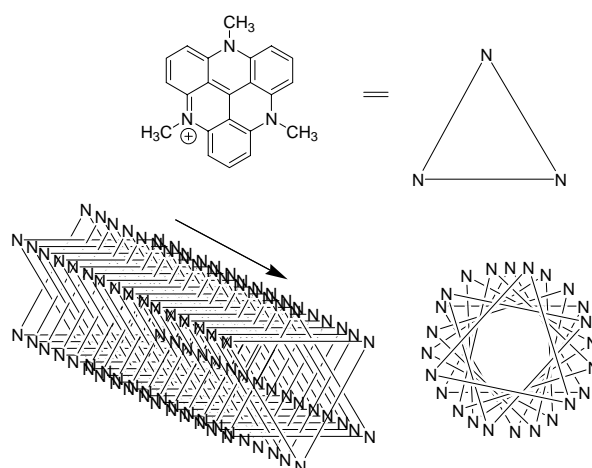


Figure 3.9: Prediction of packing pattern of trimethyltriazatriangulenium in **3.4C**.

The close packing of the triazatriangulenium dimers in **3.5D** and **3.6D** is due to the interaction between delocalized cation and  $\pi$  systems. As shown in chapter two, for the pyridinium-derived dimers, the cation- $\pi$  interactions between triazatriangulenium charge and the triazatriangulenium  $\pi$  system enhances the cationic  $\pi$ - $\pi$  interactions. These interactions overcome the CH- $\pi$  interactions and dominate the **FF** packing pattern of the  $\pi$  systems.

Strong cationic  $\pi$ - $\pi$  interactions were shown by the short centroid distance between the two triazatrianguleniums. The distance is 3.29 Å for the triazatriangulenium dimers in **3.5D** and **3.6D**, which is shorter than any other cationic dimers of pyridinium (e.g. the interplanar distance of the benzanthracene type four-ring pyridinium is 3.40 Å). The shorter the distance, the more stable the atomic interactions between the aromatic rings, and the better the  $\pi$ - $\pi$  interactions.

The results of these studies of the triazatriangulenium packing also agree with the conclusion made in the last chapter about the importance of the size (increase of the rings) of cations in the cationic  $\pi$ - $\pi$  interactions: more rings in the cations cause more overlap between them, which in turn leads to stronger atomic contact.

### 3.2.2 Solid-state study of salts of triangulene anion and nonaromatic counterion

More evidence for the importance of the delocalized cation in the cationic  $\pi$ - $\pi$  interaction comes from the packing of the triangulene anions, which has a similar structure to that of the triazatriangulenium cation, as shown in Figure 3.3. In the crystals of the trioxytriangulene anion salt, tetrabutylammonium trioxytriangulene (**3.1E**), the anions are packed in a herringbone style, with tetrabutylammonium as counterions between them. The cations are on the 6-fold axis, on top of the anion and 4.57 Å away from it, as shown in Figure 3.10. This shows the regular point-charge, cation- $\pi$  interaction. There is no overlap between the aromatic rings.

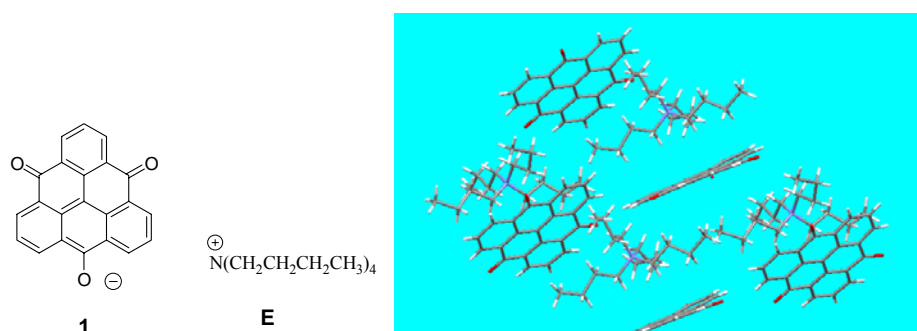


Figure 3.10: Salt tetrabutylammonium trioxytriangulene **3.1E** (left) and its crystal structure (right).

Between two trioxytriangulene anions, the major interactions are the anion-anion repulsion, anion- $\pi$  interaction, and  $\pi$ - $\pi$  attraction. The anion-anion interaction and anion- $\pi$  interaction both are repulsive. The herringbone style packing is probably due to the anion-anion repulsion and anion- $\pi$  interaction between the anionic rings.

Strong cationic  $\pi$ - $\pi$  interactions were shown by the high melting point of these triazatriangulenum salts. The DSC spectra of the triazatriangulenum salts and the ammonium trioxytriangulene are shown in Figure 3.11.

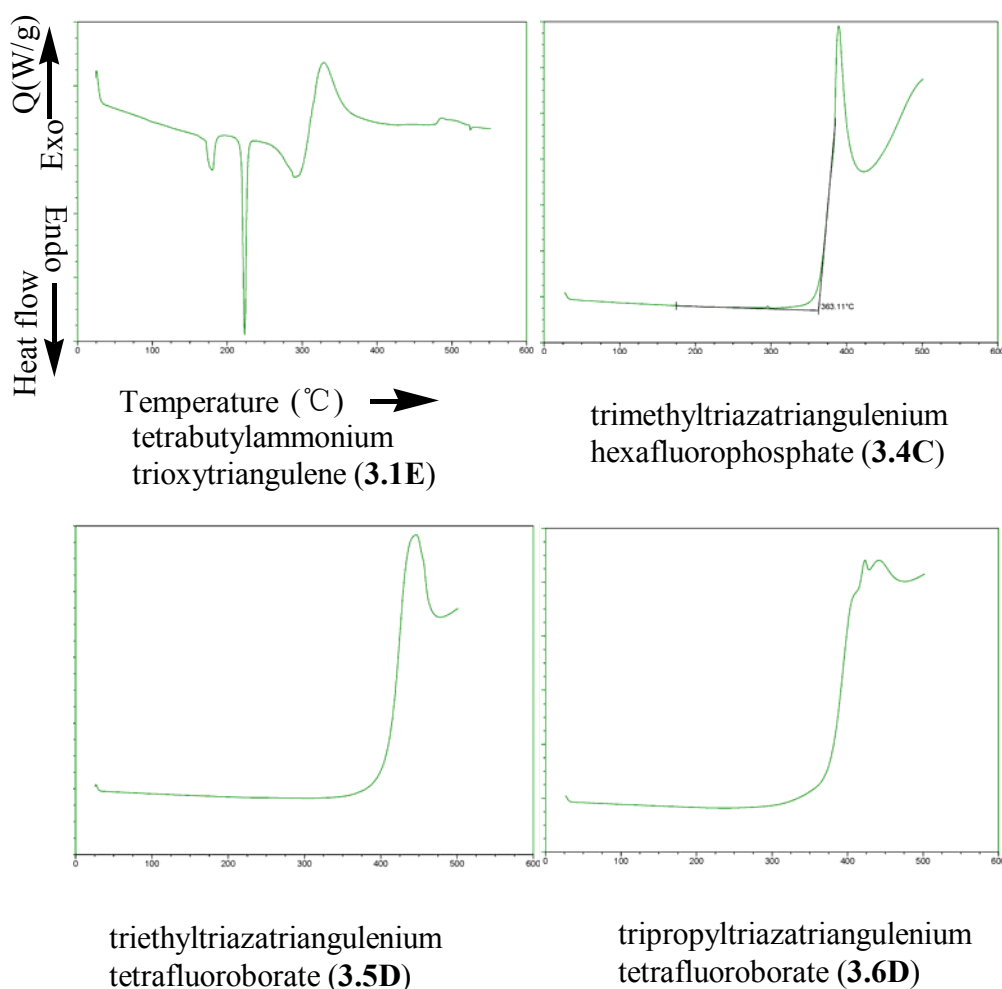


Figure 3.11. DSC spectra of tetrabutylammonium trioxytriangulene (**3.1E**), trimethyltriazatriangulenum hexafluorophosphate (**3.4C**), trimethyltriazatriangulenum tetrafluoroborate (**3.5D**), and tripropyltriazatriangulenum tetrafluoroborate (**3.6D**).

For the DSC spectrum, the X axis is temperature ( $^{\circ}\text{C}$ ); the Y axis is heat flow Q (W/g) with exothermic upward. In Figure 3.11, all triazatriangulonium salts decomposed before melting. Their melting points are much higher than those of ammonium trioxytriangulene salt ( $225\text{ }^{\circ}\text{C}$ ). The trioxytriangulene salt has a similar structure and molecular weight as those of triazatriangulonium salts. The higher melting points show better interactions between cationic aromatic rings than those between trioxytriangulene rings.

### 3.2.3 Solid-state study of triangulene salt pairs

#### 3.2.3.1 Novel delocalized, flat, aromatic ionic salt pairs

There is no reported example of the delocalized, flat, aromatic ionic salt pair in the literature. The cation, anion molecules used in our study of the salt pairs are shown in Figure 3.12.

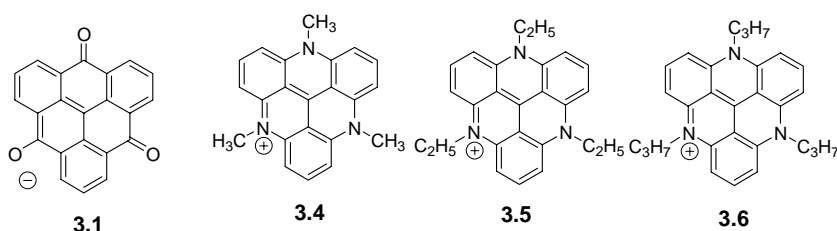
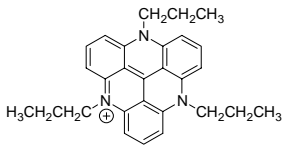
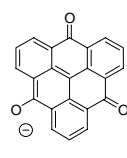
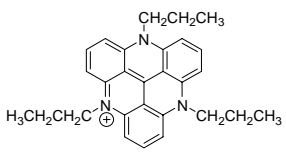
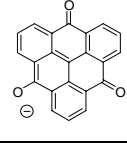


Figure 3.12: Triangulene anion, cations, and their corresponding codes for triangulene salt pairs study.

#### 3.2.3.2 Solid-state study

The triangulene salt pairs (**3.14**, **3.15**, and **3.16**) can only be dissolved in hot DMSO. All the triangulene salt pairs showed a deep brown color. Except for the needle-like tripropyltriangulene salt pair **3.16**, all salt pairs are powder-like solids because they have poor solubility in the hot DMSO solution. Only the crystal structure of the tripropyltriangulene salt pair **3.16** could be elucidated by single-crystal X-ray diffraction. Table 3.2 shows crystal data of salt pair **3.16**, salt **3.1E** and **3.6D**. Figure 3.13 shows crystal structures of **3.16**, **3.1E** and **3.6D**.

Table 3.2. Parameters of crystal structures of tripropyltriazatriangulenium trioxytriangulene (**3.16**), tripropyltriazatriangulenium tetrafluoroborate (**3.6D**) and tetrabutylammonium trioxytriangulene (**3.1E**)

Cation	Anion	Packing type,	ring overlap, %	d, Å
		pseudo $\beta$	<b>FFEC</b> , 66% cation-cation dimer	3.29
			<b>FFEC</b> , 28% inter-dimer	3.30
	$\text{BF}_4^-$	pseudo $\beta$	<b>FFCC</b> , 66% cation-anion dimer	3.29
			<b>FFEE-CC</b> , 0% inter-dimer	5.37
$\oplus$ $\text{N}(\text{CH}_2\text{CH}_2\text{CH}_2\text{CH}_3)_4$		Herring- bone	NA	NA
			NA	NA

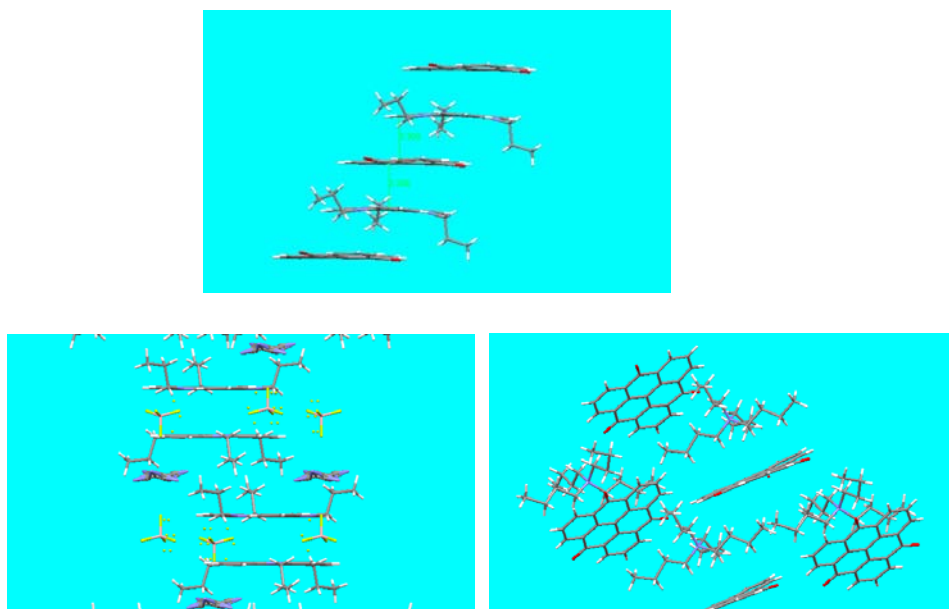


Figure 3.13: Crystal structures of tripropyltriazatriangulenium trioxytriangulene (**3.16**), tripropyltriazatriangulenium tetrafluoroborate (**3.6D**), and tetrabutylammonium trioxytriangulene (**3.1E**).

In Table 3.2, in the column labeled ring overlap, the first entry for each salt is the packing within the dimer (intra-dimer) and % overlap, and the second entry is similar information between dimers (inter-dimer). As shown in Figure 3.13, the tripropyltriazatriangulenium (cation **3.6**) and trioxytriangulene (anion **3.1**) formed dimers with the **FFEC** packing pattern. The interplanar distance within the dimer was as short as 3.29 Å and 66% overlap, the same as those of the cationic dimer in the nonaromatic counterion salt. But the inter-dimer interaction for salt pair **3.16** is much better than that of the cationic dimers in crystals **3.5D** and **3.6D**. The former has 28% overlap and 3.30 Å interplanar distances, while the latter has no overlap with the distance 4.32 and 5.37 Å, which are much greater than the VDW distance (3.4 Å). The increased overlap enhances the atomic contact between **3.1** and **3.6**. Also inside the salt pair **3.16**, the intra-dimer and inter-dimer have almost the same interplanar distances, which means the cation and anion try to pack evenly while contending with the steric issue of the substitution groups. We can predict that, without the steric issue, such as salt pair **3.14**, the cation-anion will pack evenly with either **FFCC** or **FFEC** style with 66% overlap, similar to the prediction of the cationic  $\pi$ -system dimer trimethyltriazatriangulenium (**3.4C**) in Figure 3.9 in section **3.2.1**. The difference is the cationic and anionic  $\pi$ -systems will stack alternately. The improved packing pattern of the ionic salt pair is caused by the enhanced  $\pi$ - $\pi$  interaction, due to the delocalized cation-anion interactions.

The DSC spectra of the salt pairs provide some thermal information about the salt-pair packing. The DSC curves of the salts tetrabutylammonium trioxytriangulene (**3.1E**), trimethyltriazatriangulenium trioxytriangulene (**3.14**), triethyltriazatriangulenium trioxytriangulene (**3.15**), and tripropyltriazatriangulenium trioxytriangulene (**3.16**) are shown in Figure 3.14.



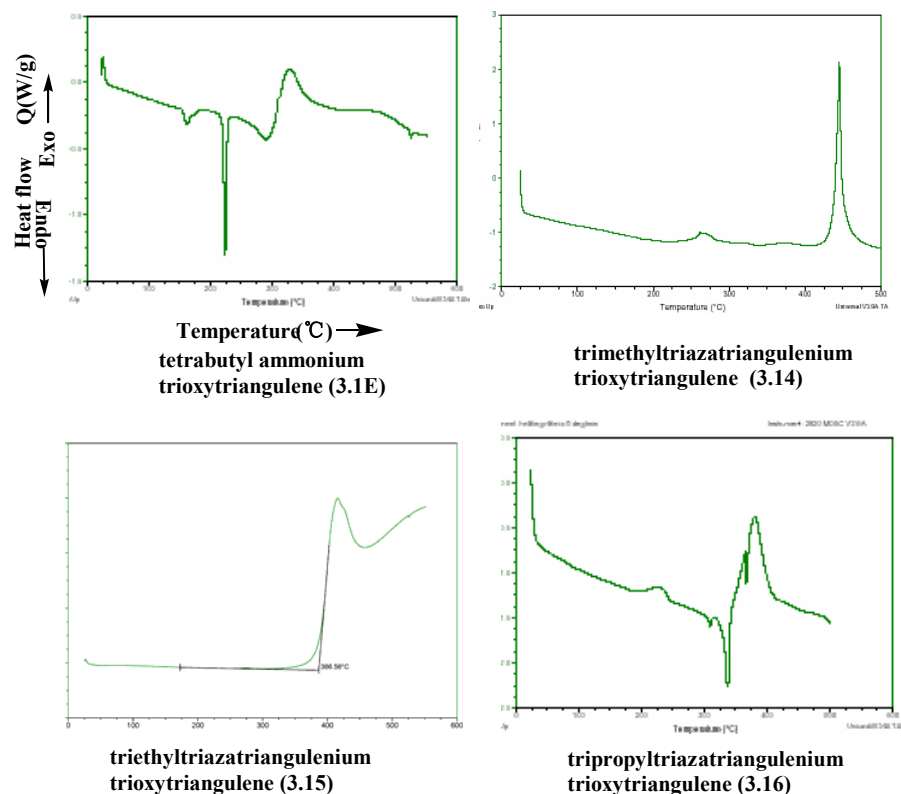


Figure 3.14: DSC spectra of tetrabutylammonium trioxytriangulene (**3.1E**), trimethyltriazatriangulenium trioxytriangulene (**3.14**), triethyltriazatriangulenium trioxytriangulene (**3.15**) and tripropyltriazatriangulenium trioxytriangulene (**3.16**).

In Figure 3.14, the X axis is temperature (°C); the Y axis is heat flow Q (W/g) with exothermic upward. Salt pairs **3.14**, **3.15** and **3.16**, trialkyltriazatriangulenium trioxytriangulene, all decomposed (or while) melting, which were shown by the large exothermic peak and the unrepeatable result in the second scan. The small exothermic peak at ~270 °C for **3.14** was perhaps due to the phase transition. It is impossible to measure the accurate melting points. Nevertheless, some trends are clear:

1) All aromatic salt pairs have higher melting points than that of the salt of **3.1E**. This is due to the delocalized cation-anion interaction in the  $\pi$  system of salt pairs. Compound **3.1E** is a salt that is formed between aromatic anion of the salt pairs (trioxytriangulene in **3.14-6**) and nonaromatic counterion, tetrabutylammonium. There is no delocalized cation-anion interaction in the solid state of salt **3.1E**.

2) Stability of triazatriangulenium trioxytriangulene salt pairs decrease with the increase of the size of substitution groups on the nitrogen atoms: for decomposing temperatures in Figure 3.17, **3.14**>**3.15**>**3.16**. While salt-pairs, **3.15** and **3.16**, decomposed at lower temperatures (415 °C and 380 °C) than their cation salts, **3.5D** (440 °C) and **3.6D** (430 °C), the trimethyltriazatriangulenium trioxytriangulene salt pair **3.14** (445 °C), melted at a much higher temperature than the cation salt **3.4C** (390 °C).

### 3.3 Delocalized cation-anion pair enhanced $\pi$ - $\pi$ interactions

There are many kinds of the molecular interactions between the cationic and anionic  $\pi$ -systems (**3.4-6** and **3.1**). They are delocalized cation-anion pair coulombic attraction, delocalized cation- $\pi$  interaction, anion- $\pi$  repulsion,  $\pi$ - $\pi$  attraction, etc. All of these interactions contribute to the ionic  $\pi$ - $\pi$  interaction. However, the interactions involving ions are of higher magnitude. The salt pair **3.16** was chosen as an example to discuss the ionic  $\pi$ - $\pi$  interaction.

#### 3.3.1 Delocalized cation-anion pair coulombic attraction

Coulombic attraction is the attractive interaction between two opposite charges. The equation for coulombic potential energy is shown below (Equation 3.2), where  $Q = \pm ne$  ( $n$  is the number and  $e$  is the magnitude of the charges.  $e = 1.602 \times 10^{-19}$  C),  $r$  is distance between the charges and  $\epsilon (= 8.854 \times 10^{-12} \text{ J}^{-1} \text{ C}^2 \text{ m}^{-1})$  is the dielectric constant.

$$U = \frac{Q_1 Q_2}{4 \pi \epsilon r}$$

Equation 3.2. Coulombic potential between two charges

According to Equation 3.2, the magnitude of the attraction potential energy is inversely proportional to the distance between two opposite charges: the closer, the stronger. Since the cation and anion  $\pi$ -systems of the salt pair **3.16** are highly conjugated, the positive and negative charges can be easily delocalized on the surface of **3.6** and **3.1**. Suppose the cation-anion attraction can be viewed as two charges interacting with each

other from the center of the  $\pi$ -systems, due to the close centroid to centroid distance, which is 3.56 Å between cation **3.6** to the anion **3.1**. The coulombic attraction between them will be strong. In the **EF** pattern, the centroid distance of the triangulene salt pair will be at least 7.4 Å (shortest center-edge distance 4.15 Å + 1.7 Å of carbon van der Waals distance + 1.55 Å of nitrogen van der Waals distance). The coulombic attraction in the face-to-face pattern is much stronger than that of the edge-to-face pattern. The face-to-face, center-to-center packing will maximize this interaction, which will probably show in the trimethyltriazatriangulenium trioxytriangulene salt pair **3.14** (see section 3.2.3.2).

### **3.3.2 Delocalized cation- $\pi$ interaction**

Large aromatic cations, such as **3.5D** and **3.6D** in Section 3.2.1, are capable of forming strong donor-acceptor interactions of the cation- $\pi$  type. Similar to these salts, the delocalized cation- $\pi$  interaction exists between the delocalized charged on cation **3.6** and the  $\pi$  system of anion **3.1** in the salt pair **3.16**. Instead of pair cation- $\pi$  interactions in **3.6D**, there is only one in **3.16**. This cation- $\pi$  interaction will enhance the  $\pi$ - $\pi$  attraction in the salt pair **3.16**. Stacking pattern of the aromatic system could introduce strong cation- $\pi$  interaction. As with the coulombic attraction discussed above, the face-to-face, center-to-center packing will maximize this interaction, which will probably show in the trimethyltriazatriangulenium trioxytriangulene salt pair **3.14**.

### **3.3.3 Other interactions: anion- $\pi$ repulsion, dipole-dipole, and ion-dipole interactions**

According to the electrostatic model of the benzene rings, the distribution of the electrostatic surface on the benzene rings can be treated as  $+\delta$  charge at the nucleus center and two  $-\delta/2$  charges at a  $d$  distance, as shown in Figure 1.6, pp.12.<sup>(23)</sup> The  $\pi$  systems of the cation **3.6** and the anion **3.1** can also be treated as the electrostatic model, with a positive charge at the backbone and negative charges above and below it. As with the delocalized cation- $\pi$  interaction between the delocalized positive charge on cation **3.6**

and the  $\pi$  system of anion **3.1** in the salt pair **3.16**, there will also be the delocalized anion- $\pi$  interaction between the delocalized negative charge on anion **3.1** and the  $\pi$  system of cation **3.6**. These two interactions should be at the same magnitude.

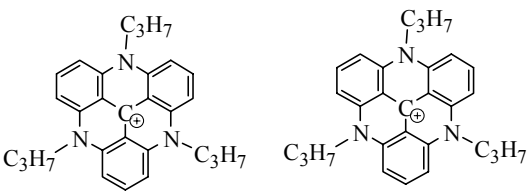
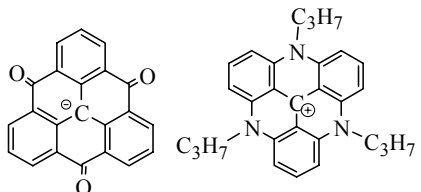
Neither the dipole-dipole nor ion-dipole interactions will be a significant issue here because in the  $D_{3h}$  symmetric molecules, the dipole moments cancel each other. All the cations and the anion have zero net dipole moments.

### 3.3.4 Cationic $\pi$ -system dimer versus cation-anion $\pi$ -system dimer

The cations and anions we studied are all highly conjugated  $\pi$ -systems, so all those positive and negative charges are delocalized. The word “delocalized” will be omitted later on for simplification.

The cationic dimers were studied in Chapter 2. The cation-anion  $\pi$ -system dimers are the dimers that are formed between cationic  $\pi$ -system and anionic  $\pi$ -system, as the salt pair **3.16**.

Table 3.3: Major interactions between two  $\pi$ -systems in a cationic  $\pi$ -system dimer versus that between two  $\pi$ -systems in a cation-anion  $\pi$ -system dimer

cationic $\pi$ -system dimer		cation-anion $\pi$ -system dimer	
			
two positive charges and two $\pi$ -systems		one positive charge, one negative charge and two $\pi$ -systems	
$\pi$ - $\pi$ attraction	x1	$\pi$ - $\pi$ attraction	x1
cation- $\pi$ attraction	x2	cation- $\pi$ attraction	x1
		charge coulombic attraction	x1
charge repulsion	x1	anion- $\pi$ repulsion	x1

In a cationic  $\pi$ -system dimer, there are two positive charges and two  $\pi$ -systems. The major interactions between these two  $\pi$ -systems could include:  $\pi$ - $\pi$  attraction, cation- $\pi$  attractions, and positive-positive charge repulsion. While in a cation-anion  $\pi$ -system dimer, there will be one positive charge, one negative charge and two  $\pi$ -systems. The major interactions between these two  $\pi$ -systems could include:  $\pi$ - $\pi$  attraction, positive-negative charge coulombic attraction, cation- $\pi$  attraction, and non bonding repulsion as shown in Table 3.3.

Suppose the cation- $\pi$  and  $\pi$ - $\pi$  attractions are similar in these two dimers. Compare cation-anion  $\pi$ -system dimers with the cationic  $\pi$ -system dimers, after the similar interactions are subtracted, the interactions that are left in these two dimers will be: one cation- $\pi$  attraction and one positive-positive charge repulsion for cationic  $\pi$ -system dimers; one positive-negative charge coulombic attraction and one anion- $\pi$  repulsion for cation-anion  $\pi$ -system dimers. The charge repulsion and charge attraction, cation- $\pi$  and anion- $\pi$  interactions are similar interactions. Their energies will be similar. The charge-charge interaction is stronger than the cation- $\pi$  interaction. For example, the calculated and experimental results of the sodium cation-benzene interaction are 29.5 and 19.2 kcal/mol when sodium is 2.4 Å from the center of the ring. The calculation results of the potential between two charges at 2.4 Å distance can be 136.7 kcal/mol according to Equation 3.2. The magnitude difference between them should not be easily changed by the resonance effect. This comparison shows that the interactions of ionic  $\pi$ -system pair will be stronger than the cationic  $\pi$ -system pair. The newly introduced cation-anion interaction enhanced the affinity between the rings. This affinity will dominate the packing pattern. In addition, unlike the orientation dominated quadrupole-quadrupole interaction, the dimensionless ion interactions will add to the van der Waals interaction and increase the attractive  $\pi$ - $\pi$  interaction between rings. The strong interaction between the ionic  $\pi$  system pair (**3.1** and **3.6**) is dominated by the positive charge-negative charge coulombic attraction, which enhances the  $\pi$ - $\pi$  attraction between aromatic systems.

### 3.4 Molecular orbital study

The molecular orbitals of triazatriangulenium cation and trioxytriangulene anion were studied. The HOMO of trioxytriangulene anion, LUMO of triazatriangulenium cation, the optimum molecular alignment (**FFCC**), and the alignment in the salt pair (**3.16**) are shown in Figure 3.15.

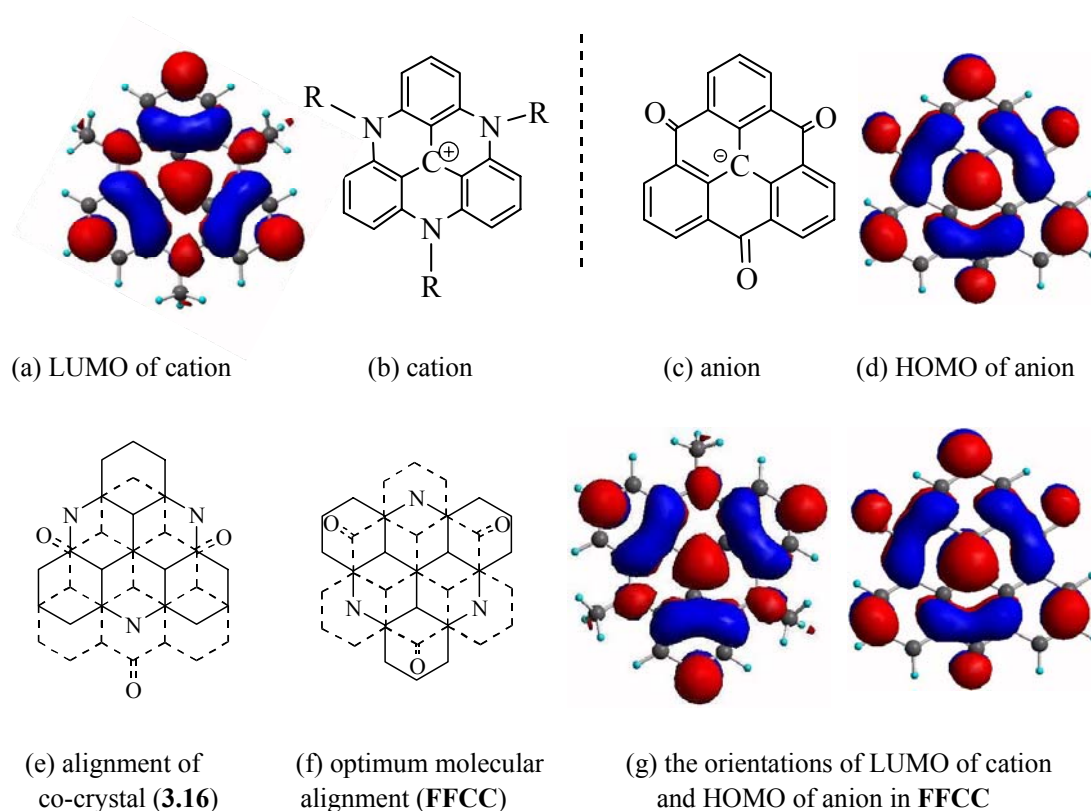


Figure 3.15. Calculated molecular orbitals of the lowest unoccupied molecular orbital (LUMO) (a) of triazatriangulenium cation (b) and the highest occupied molecular orbital (HOMO) (d) of trioxytriangulene anion (c). The simplified packing patterns of salt pair **3.16** and the hypothesized optimum molecular alignment (**FFCC**) of salt pair **3.14** are also shown, (e) and (f). In (e) and (f), the dotted lines represent anions. The orientations of the LUMO of cation and the HOMO of anion in **FFCC** are shown in (g).

Figure 3.15 shows (a) the calculated molecular orbitals for the lowest unoccupied molecular orbital (LUMO) of triazatriangulenium cation (b) and (d) the highest occupied molecular orbital (HOMO) of trioxytriangulene anion (c). The figure

also shows (e) the simplified packing pattern determined from the crystal structure of salt pair **3.16** and (f) the hypothesized optimum molecular alignment (**FFCC**), which could be the possible packing structure of salt pair **3.14**. In (e) and (f), the dotted lines represent anions. The orientations of the LUMO of cation and the HOMO of anion in **FFCC** are shown in (g). The HOMO and LUMO molecular orbitals above show high compatibility with each other. When they are packed in the **FFCC** pattern, the lobes of one sign will perfectly overlap with the lobes of the other sign, in which HOMO and LUMO orbitals will interact with each other, in Figure 3.15, below right. The crystals of trimethyl-, triethyl-, and tripropyltriangulene salt pairs were prepared. However, only the crystal structure of tripropyltriangulene salt pair **3.16** could be elucidated by single-crystal X-ray diffraction. The optimum molecular alignment (**FFCC**) was not observed in salt pair **3.16** due to the steric hindrance of propyl groups on nitrogen atoms.

In the salt pair, restricted Hartree-Fock at the 6-311 level calculated a 2.1 and a 1.3 eV decrease in the energy gap between the HOMO and the LUMO when the cation and anion were compared to the salt pair separated by approximately 3.3 Å. The calculation was run to evaluate the compatibility of the molecular orbitals and not to estimate the energies of the molecular orbitals. The short interplanar distance (3.29 and 3.30 Å) within van der Waals radii of two carbons (3.40 Å) in the solid state of the salt pair **3.16** confirmed the compatibility.

Orbital overlap will lower the system energy. Strong interactions will result from the overlap of these two charged species with compatible molecular orbital coefficients, as with the HOMO of the anion and the LUMO of the cation shown in Figure 3.15. The strong interactions between anionic HOMO and the cationic LUMO should be important for the stability of the dimer. The alternate stacking of anion and cation could provide the large overlap of the HOMO and LUMO orbitals. While the orbitals were partially overlapped in salt pair **3.16**, **FFEC** stacking maximizes the overlap. This could be achieved in the salt pair **3.14**, which, unlike the salt pair **3.16**, has no substitution groups

on nitrogen atoms to break the symmetry of the stacking. The large difference in the melting/decomposition point between the salt pairs **3.14** and **3.16** also hinted that the former associated  $\pi$ -faces better than the latter (see discussion in the sections above).

### 3.5 Conclusion

- 1) Stacking interactions are strong between the charged aromatic salt pairs, which were shown by the large ring overlap, short interplanar distance and high melting points.
- 2) The **FF** packings ( $\pi$ -stackings) of the aromatic salt pairs are due to the charge-charge attraction and cation- $\pi$  interactions. The stacking pattern of the aromatic system could introduce strong charge-charge attraction and cation- $\pi$  interaction. These interactions dominate in the orientation and stabilization of packing patterns of these salt pairs. The face-to-face, center-to-center packing (**FFCC**) will maximize this interaction, which will probably show in the trimethyltriazatriangulenium trioxytriangulene salt pair **3.14**. This is corroborated by the DSC result of salt pairs and cation salts.
- 3) The stacking pattern and strong interactions between the charged aromatic ions (**3.14-16**) can also be explained by the interactions between the compatible HOMO and LUMO orbitals of these two charged species.



## References

- 1) G. Portella, J. Poater, M. Sola, *J. Phys. Org. Chem.* **2005**, *18*, 785-791.
- 2) J. R. Dias, *J. Chem. Inf. Comput. Sci.* **1999**, *39*, 144-150.
- 3) E. Clar, *The Aromatic Sextet*, Wiley, New York, 1972.
- 4) R. J. Dias, *J. Phys. Org. Chem.* **2002**, *15*, 94-102.
- 5) G. Treboux, P. Lapstun, K. Silverbrook, *Chem. Phys. Lett.* **1999**, *306*, 402-406.
- 6) V. Lemaure, D. A. S. Filho, V. Coropceanu, M. Lehmann, Y. Geerts, J. Piris, M. G. Debije, A. M. Craats, K. Senthilkumar, L. D. Siebbeles, J. M. Warman, J. Bredas, J. Cornil, *J. Am. Chem. Soc.* **2004**, *126*, 3271-3279.
- 7) G. Kestemont, V. Halleux, M. Lehmann, D.A. Ivanov, M. Watson, Y. H. Geerts, *Chem. Commun.* **2001**, 2074-2075.
- 8) N. Boden, R. C. Borner, R. J. Bushby, J. Clements, *J. Am. Chem. Soc.* **1994**, *116*, 10807-10808.
- 9) G. Allinson, R. J. Bushby, J. L. Paillaud, D. Oduwole, K. Sales, *J. Am. Chem. Soc.* **1993**, *115*, 2062-2064.
- 10) G. Allinson, R. J. Bushby, J. L. Paillaud, M. Thornton-Pett, *J. Chem. Soc., Perkin Trans. 1.* **1995**, *4*, 385-390.
- 11) G. Allinson, R. J. Bushby, M. V. Jesudason, J. Paillaud, N. Talor, *J. Chem. Soc., Perkin Trans. 2.* **1997**, 147-156.
- 12) F. C. Krebs, P. S. Larsen, J. Larsen, C. S. Jacobsen, C. Boutton, N. Thorup, *J. Am. Chem. Soc.* **1997**, *119*, 1208-1216.
- 13) G. K. H. Madsen, F. C. Krebs, B. Lebech, F. K. Larsen, *Chem. Eur. J.* **2000**, *6*, 1797-1804.
- 14) R. Lin, K. F. Braun, H. Tang, U. J. Quaade, F. C. Krebs, G. Meyer, C. Joachim, K. H. Rieder, K. Stokbro, *Surf. Sci.* **2001**, *477*, 198-208.
- 15) J. E. Field, D. Venkataraman, *Chem. Mater.* **2002**, *14*, 962-964.
- 16) B. W. Laursen, F. C. Krebs, *Angew. Chem., Int. Ed.* **2000**, *39*, 3432-3434.

- 17) B. W. Laursen, F. C. Krebs, *Chem. Euro. J.* **2001**, *7*, 1773-1783.
- 18) S. Ito, S. Kikuchi, N. Morita, T. Asao, *J. Org. Chem.* **1999**, *64*, 5815-5821.
- 19) R. J. Dias, *J. Phys. Org. Chem.* **2002**, 94-102.

## Chapter Four

### Conclusions

The work of this dissertation was separated into two parts. The first part was designed to probe solution-state conformation of derivatives of compound *N,N'*-[1,3-phenylenebis(methylene)]bis(2-phenylpyridinium) dibromide (**1a**, **2b**, and **2c**) in solution. In the second part, crystal structures of pyridinium derivatives and triangulene salt pairs were studied to investigate the ion effect on the solid-state conformation of aromatic systems.

A general protocol for the application of magnetic anisotropy to quantitative multi-state conformational analysis was proposed by the current study. The reliability of this method of conformational analysis was checked by the mass balance. Also, all-positive solutions for the equations under different conditions confirmed the reliability. This novel quantitative conformational analysis technique can be used to study canonical interactions such as ion pairing, hydrogen bonding, and molecular recognition.

In the current study, dependence of the probe conformations on the dispersive interactions at the aromatic edges between solvent and probes was tested by the fluorinated derivatives (**2b** and **2c**) of probe molecule (**1a**). Solution and solid studies of these probe molecules put the previous conclusion drawn by the Cammers group in question. Current studies show that the dispersive interaction at the aromatic edge could not be the predominant force on the conformational change in **1a** during the fluoroalkanol perturbation. Combined with thermodynamic studies and molecular modeling calculations, the current study indicated that charges might be important in the folding of these dicationic systems.

The result of solution and solid-state studies also put the importance of quadrupole moment interactions in the dication folding into question. In solid state, **1a**, **2b**, and **2c** used the same **F**-like conformation. The centroid distances between xylyl and

phenyl rings increased from **1a**, **2b**, to **2c**. In solution state, studies showed that the stacking states decreased (**1a** > **2b** > **2c**) with the increasing of the number of fluorine atoms on the phenyl rings. Both the solution and solid states indicate the interactions of the phenyls to the xylyls in **2b** and **2c** are weaker than that of **1a**. If the quadrupole moment dominates the probes folding, the trend in solid and solution states will be totally different due to the stronger hexafluorobenzene and benzene interaction than that of the benzene-benzene.

Neutral hydrocarbon 2,2'-biphenyl- $\alpha,\alpha'$ -*m*-xylylene (**2e**) was also synthesized. It is isoelectronic and structurally similar to **1a**. Solid-state studies of two isoelectronic, structurally similar compounds, **2e** and **1a**, showed that charges are important in the formation of the stacking conformation in solid state, which may be due to charge- $\pi$  interaction.

In the second part, a study of the CSD (Cambridge Structural Database) was performed to investigate the solid-state interactions between cationic  $\pi$  systems. The survey of pyridinium-derived cations showed a tendency of the cations to stack face-to-face (**FF**) as dimers. These **FF** packing patterns of the pyridinium-derived cations are totally different from their corresponding aromatic hydrocarbons. The aromatic hydrocarbons are packed in a herringbone style. Compared with the herringbone style, the **FF** packings of the pyridinium rings increase the overlaps of the aromatic rings. The increased overlaps enhance  $\pi$ - $\pi$  interactions between aromatic systems.

The model of regular point-charge cation- $\pi$  interaction was used to explain the delocalized cation- $\pi$  interaction. The better interactions of these cationic rings are probably due to the cation- $\pi$  interactions, which overcome the CH- $\pi$  interactions and dominate the **FF** packing pattern of the rings.

The cation- $\pi$  interactions are dominant in the orientation and stabilization of packing of pyridinium-derived cations. Though only few examples of the cations with more than 3 rings can be found, the trend of the packing of these cations is still clear: the

more rings the cations have, the more overlap between the cations. This is probably due to the better alleviation of the charge repulsions and larger cation- $\pi$  interactions.

To further study the charge effects on the  $\pi$ - $\pi$  interactions, novel aromatic salt pairs of triangulene derivative with the cation-anion interaction were synthesized.  $\pi$ - $\pi$  interactions of these salts were studied. Stacking interactions are very strong between these charged aromatic salts, which were shown by the large ring overlap, short interplanar distance and high melting points. The **FF** packings ( $\pi$ -stackings) of the aromatic salt pairs are due to the charge-charge attraction and cation- $\pi$  interactions. Stacking patterns of aromatic systems could introduce strong charge-charge attractions and cation- $\pi$  interactions. The strong interaction between the salt  $\pi$  system pair is dominated by the coulombic attraction which is synergistic with the cation- $\pi$  interaction.

## Chapter 5

### Experimental Section

Data for X-ray crystal analysis were collected at 90 K using a Nonius-Kappa CCD diffractometer. Crystals were mounted in paratone oil. Raw diffraction data was processed by HKL-SMN program package.<sup>(1)</sup> SHELXS-97 program was used to solve the structures. Atomic scattering factors were acquired from the International Tables for Crystallography.<sup>(2)</sup> Crystal structure parameters are shown in the appendix. <sup>1</sup>H NMR experiments were conducted at Varian INOVA 400 MHz NMR spectrometers. Reagents were purchased commercially without further purification. All solvents used were dried and distilled.

#### 5.1 Experiments of Chapter one

##### *N,N'*-[1,3-phenylenebis(methylene)]bis(2-trifluorophenylpyridinium) dibromide (**2b**)<sup>(3,4)</sup>

Compound *N,N'*-[1,3-phenylenebis(methylene)]bis(2-trifluorophenylpyridinium) dibromide (**2b**) was synthesized in two steps, as shown in Figure 5.1. The synthetic conditions and characterizations of compound **5.1** and **2b** can be found in References 3-4.

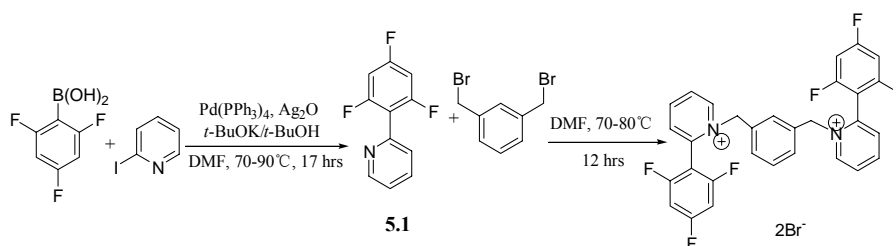


Figure 5.1 Synthesis of **2b** in two steps.

##### *N,N'*-[1,3-phenylenebis(methylene)]bis(2-pentafluorophenylpyridinium) dibromide (**2c**)<sup>(3,4)</sup>

Compound *N,N'*-[1,3-phenylenebis(methylene)]bis(2-pentafluorophenylpyridinium) dibromide (**2c**) was synthesized similarly as **2b** in two steps, as shown in Figure 5.2. The synthetic conditions and characterizations of compound **5.1** and **2b** can be found in References 3-4.

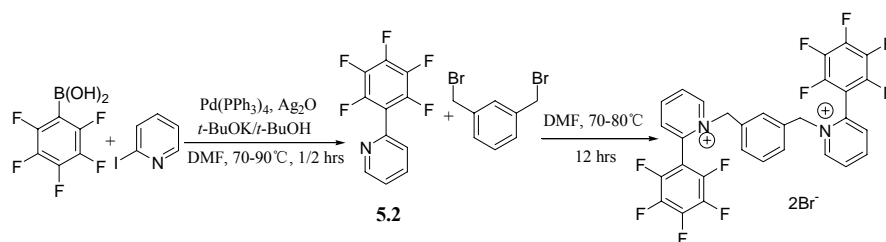


Figure 5.2. Synthesis of **2c** in two steps.

### 2,2'-bis-2-biphenyl- $\alpha,\alpha'$ -*m*-xylene (**2e**)<sup>(5)</sup>

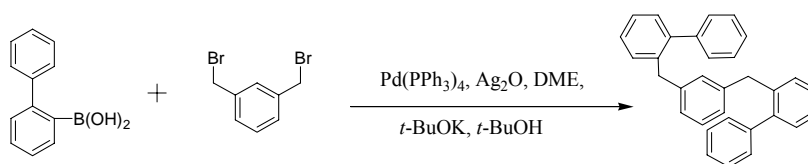


Figure 5.3. Synthesis of 2, 2'-bis-2-biphenyl- $\alpha,\alpha'$ -*m*-xylene (**2e**).

All synthetic operations were performed under a nitrogen atmosphere.  $\alpha,\alpha'$ -dibromo-*m*-xylene (394.5 mg, 1.5 mmol), Pd(PPh<sub>3</sub>)<sub>4</sub> (115.5 mg, 0.1 mmol), and 1,2-dimethoxyethane (20 mL) was added to an oven-dried 50 mL flask. The bright yellow solution was stirred at room temperature for 20 min. 2-biphenylboronic acid (682.4 mg, 3.45 mmol), *t*-BuOK (672 mg, 6.0 mmol), *t*-BuOH (3.0 mL) and Ag<sub>2</sub>O (1390 mg, 6.0 mmol) were added successively. A dark solution with dark precipitate was formed. The mixture refluxed under nitrogen at 85 °C for 17 h. The mixture was cooled, concentrated in vacuum, and partitioned between EtOAc: H<sub>2</sub>O (1:1, 120 mL). The layers were separated and the aqueous layer was washed with two additional 60 mL portions of EtOAc. The combined organic layers were dried over MgSO<sub>4</sub> and concentrated in vacuum. Silica gel column chromatography (Hexane:CHCl<sub>3</sub> = 4:1) gave **2e** as a colorless solid that crystallized from 10:1 Hexane:EtOAc (31%); mp 132–134 °C; <sup>1</sup>H NMR (400 MHz, CDCl<sub>3</sub>):  $\delta$  7.30 (m, 12H), 7.19 (m, 6H), 7.07 (t, *J* = 7.6 Hz, 1H), 6.79 (d, *J* = 7.6Hz, 2H), 6.59 (s, 1H), 3.87 (s, 4H); <sup>13</sup>C NMR (100 MHz, CDCl<sub>3</sub>):  $\delta$  142.4, 141.8, 141.5, 138.5, 130.5, 130.3, 129.8, 129.5, 128.3, 128.2, 127.6, 127.0, 126.5, 126.3, 39.2; MS (IE) *m/z* 410 [M]. X-Ray diffraction confirmed connectivity.

### 2,2'-bis-2-methylphenyl- $\alpha,\alpha'$ -*m*-xylylene (**2f**)<sup>(5)</sup>

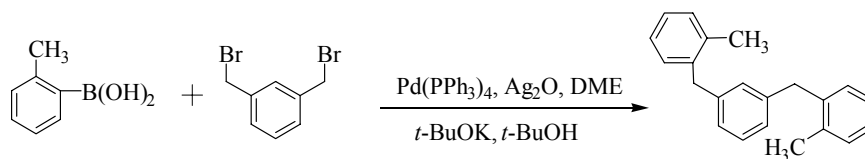


Figure 5.4. Synthesis of 2,2'-bis-2-methylphenyl- $\alpha,\alpha'$ -*m*-xylylene (**2f**).

All synthetic operations were performed under a nitrogen atmosphere.  $\alpha,\alpha'$ -dibromo-*m*-xylylene (394.5 mg, 1.5 mmol),  $\text{Pd}(\text{PPh}_3)_4$  (115.5 mg, 0.1 mmol), and 1,2-dimethoxyethane (20 mL) was added to an oven-dried 50 mL flask. The bright yellow solution was stirred at room temperature for 20 min. *o*-tolylboronic acid (469.2 mg, 3.45 mmol),  $t\text{-BuOK}$  (672 mg, 6.0 mmol),  $t\text{-BuOH}$  (3.0 mL) and  $\text{Ag}_2\text{O}$  (1390 mg, 6.0 mmol) were added successively. A dark solution with dark precipitate was formed. The mixture refluxed under nitrogen at 85 °C for 17 h. The mixture was cooled, concentrated in vacuum, and partitioned between EtOAc:  $\text{H}_2\text{O}$  (1:1, 120 mL). The layers were separated and the aqueous layer was washed with two additional 60 mL portions of EtOAc. The combined organic layers were dried over  $\text{MgSO}_4$  and concentrated in vacuum. Silica gel column chromatography (Hexane: $\text{CHCl}_3$  = 3:1) gave 2,2'-bis-2-methylphenyl- $\alpha,\alpha'$ -*m*-xylylene as white solid; mp 36-38 °C;  $^1\text{H}$  NMR (400 MHz, DMSO):  $\delta$  7.14 (t,  $J$  = 7.6 Hz, 1H), 7.07 (m, 8H), 6.93 (s, 1H), 6.90 (d,  $J$  = 7.6 Hz, 2H), 3.87 (s, 4H), 2.13 (s, 6H);  $^{13}\text{C}$  NMR (100 MHz,  $\text{CDCl}_3$ ):  $\delta$  140.9, 139.7, 136.7, 130.7, 130.2, 129.7, 129.0, 126.9, 126.8, 126.5, 39.2, 19.9; MS (IE)  $m/z$  286 [M].

## 5.2 Experiments of Chapter three

The trioxytriangulene anion **3.1E**, trimethyltriazatriangulenium ion **3.4C** and tripropyltriazatriangulenium ion **3.6D** in chapter 3 are known compounds and were synthesized according to the literatures.<sup>(6,9)</sup> The reductive steps using sodium amalgam reagent to prepare compound **5.6** and **5.7** were substituted by copper activated zinc dust. The syntheses of trioxytriangulene anion (**3.1E**) and triethyltriazatriangulenium tetrafluoroborate (**3.5D**) were shown below. Trimethyltriazatriangulenium ion **3.4C** and tripropyltriazatriangulenium ion **3.6D** were synthesized similarly.



### Tetrabutylammonium 4,8-Dioxo-4H-8H-dibenzo[cd,mn]pyren-12-olate (3.1E)

The synthesis of tetrabutylammonium 4, 8-Dioxo-4H-8H-dibenzo [cd, mn] pyren-12-olate (**3.1E**) was shown in Figure 5.5.

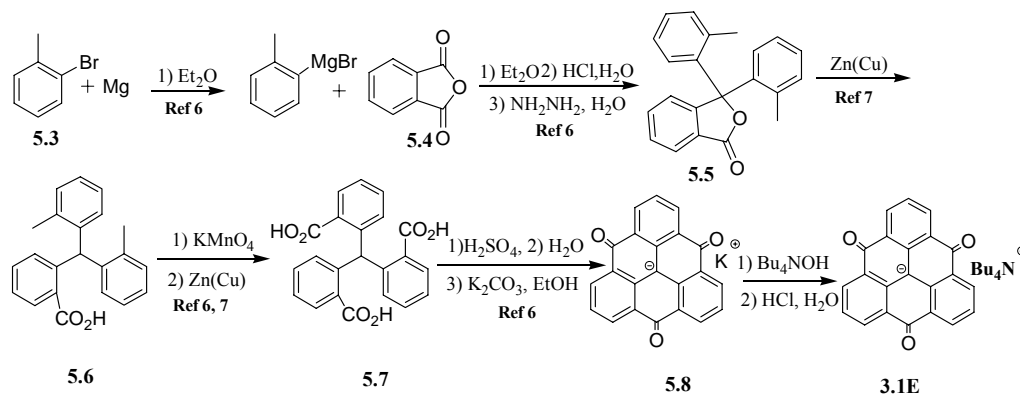


Figure 5.5. Synthesis of tetrabutylammonium 4,8-Dioxo-4H-8H-dibenzo[cd,mn]pyren-12-olate (**3.1E**).

### 3,3-Di-*o*-tolyl-1,3-dihydro-2-benzofuran-1-one (5.5)

In a vigorously stirred 500 mL round bottom flask was added 7.28 g of Mg in 150 mL diethyl ether. 2-bromotoluene (50 g, 0.29 mol) was added in dropwisely for 20 min. The mixture was refluxed for 3 hrs under N<sub>2</sub> and pumped slowly through a PTFE tube into a 1000 mL round bottom flask containing phthalic anhydride (17.3 g, 0.12mol) in 250 mL benzene solution under N<sub>2</sub>. The mixed solution was refluxed for 24 hrs (50-60 °C) then was pumped into a 250 mL 2N HCl solution. The organic phase was separated, washed with 50 mL water for 3 times, and dried with MgSO<sub>4</sub>. The mixture was filtered and evaporated. The viscous gum was dissolved into 200 mL ethanol and refluxed with 15 mL N<sub>2</sub>H<sub>4</sub>·H<sub>2</sub>O for 24 hrs. The solution was evaporated to about 20 mL and filtered. The residue was washed with (3 x 15 mL) ethanol, and dried to yield 11.9 g compound **3** (39.4%). MS (IE) *m/z* 315 [M], <sup>1</sup>HNMR (CDCl<sub>3</sub>, 400 MHz) δ 2.15 (s, 6H), 7.03 (dd, *J* = 7.8, 1.2, 2H), 7.10 (tdd, *J* = 7.8, 1.6, 0.8, 2H), 7.18 (d, *J* = 7.8, 2H), 7.24 (td, *J* = 7.5, 1.2, 2H), 7.40 (dt, *J* = 7.8, 0.8, 1H), 7.57 (td, *J* = 7.5, 1.0, 1H), 7.69 (td, *J* = 7.5, 1.2, 1H), 7.97 (dt, *J* = 7.5, 1.0, 1H). X-Ray diffraction confirmed connectivity.

### **2-(Di-*o*-tolylmethyl)benzoic acid (5.6)**

In a vigorously stirred 100 mL round bottom flask was added **5.5** (4 g, 12.7 mmol) in 30 mL 20% KOH ethanol solution. The mixture was refluxed for 48 hrs during which 15g Zn(Cu) was added in 5 portions. The mixture was diluted with 50 mL water; hot solution was filtered and washed with hot water. The filtrate was boiled for 30 min to move ethanol before the solution was acidified with concentrated hydrochloric acid. **5.6** was obtained as a white crystalline precipitate (3.19 g, 79%). <sup>1</sup>HNMR (CDCl<sub>3</sub>, 400 MHz): δ 2.18 (s, 6H), 6.64 (d, *J* = 7.8, 2H), 6.85 (s, 1H), 6.95 (dd, *J* = 7.8, 1.2, 1H), 7.06 (td, *J* = 7.6, 2.2, 2H), 7.14 (m, 4H), 7.34 (td, *J* = 7.6, 1.2, 1H), 7.43 (td, *J* = 7.8, 1.6, 1H), 8.09 (dd, *J* = 7.8, 1.6, 1H).

### **2,2',2''-(methanetriyl)tribenzoic acid (5.7)**

2 g (6.3 mmol) of **5.6** was added in a vigorously stirred 100 mL round bottom flask which contained 200 mL 0.25 M Na<sub>2</sub>CO<sub>3</sub> aqueous solution. The mixture was refluxed under N<sub>2</sub> until **5.7** was totally dissolved. 6.21 g (39.3 mmol) KMnO<sub>4</sub> was added in 4 portions over 4 hrs. The mixture was refluxed under N<sub>2</sub> for 24 hrs. Then it was reduced to around 20 mL and 55 mL of ethanol was added. The mixture was filtered and the residue was washed with 30 mL ethanol for 3 times. The solid was dried under vacuum. In a clean flask, this dried solid was added with 50 mL 20% KOH ethanol solution and 7.59 g Zn(Cu). Followed the procedure of last step, 1.07 g of a yellow solid **5.7** was obtained (42%). <sup>1</sup>HNMR (DMSO, 400 MHz) δ 6.80 (d, *J* = 7.6, 3H), 7.27 (td, *J* = 7.6, 1.0, 3H), 7.39 (td, *J* = 7.6, 1.4, 3H), 7.81 (dd, *J* = 7.6, 1.4, 3H), 8.01 (s, 1H), 12.45 (s, 3H). X-Ray diffraction confirmed connectivity.

### **Potassium 4,8-Dioxo-4H-8H-dibenzo[cd,mn]pyren-12-olate (5.8)**

0.87 g (3.0 mmol) **5.7** and 18 mL concentrated H<sub>2</sub>SO<sub>4</sub> were added to a 100 mL round bottom flask sequentially. The mixture was kept at 120 °C for 2 hrs. The mixture was cooled to room temperature and was mixed with 55 mL cold water. The mixture was centrifuged and the solid washed with water on the centrifuge. The residue was transfer

to a 25 mL round bottom flask and reflux with 20 mL 0.16 M  $K_2CO_3$  ethanol solution for 24 hrs. 30 mL  $H_2O$  was added to the cooled solution. The mixture filtered, the residue was washed with water (3 x 10 mL) and dried to afford 0.79g product 96.0% (deep blue solid).  $^1H$ NMR (DMSO, 400 MHz)  $\delta$  7.51 (t,  $J = 7.6$ , 3H), 8.75 (d,  $J = 7.6$ , 6H).

#### Tetrabutylammonium 4,8-Dioxo-4H-8H-dibenzo[cd,mn]pyren-12-olate (3.1E)

0.54 g (1.50 mmol) **5.8** and 5.5 mL concentrated HCl were added to a 100 mL  $H_2O$  in a 250 mL round bottom flask sequentially. The mixture was refluxed at 80 °C for 2 hours. The mixture was filtered and the residue was washed with 3 x 50 mL  $H_2O$ . The solid was added to 50 mL 1M aqueous tetrabutylammonium hydroxide solution and vigorously stirred for 1 hour. The blue mixture was filtered and the residue was recrystallized in  $CH_2Cl_2$ . 0.75 g deep blue crystal of **3.1E** was acquired 88%, which is pure in  $^1H$ NMR.  $^1H$ NMR (DMSO, 400 MHz)  $\delta$  8.76 (d,  $J = 7.6$ , 6H), 7.52 (t,  $J = 7.6$ , 3H), 3.12 (m, 8H), 1.56 (m, 8H), 1.27 (m, 8H), 0.91 (t,  $J = 7.6$ , 12H). X-Ray diffraction confirmed connectivity.

#### 4,8,12-Triethyl-4,8,12-triazatriangulenium tetrafluoroborate (3.5D)

Synthesis of 4,8,12-Triethyl-4,8,12-triazatriangulenium tetrafluoroborate (**3.5D**) was representative. The synthesis of **3.5D** was shown in Figure 5.6.

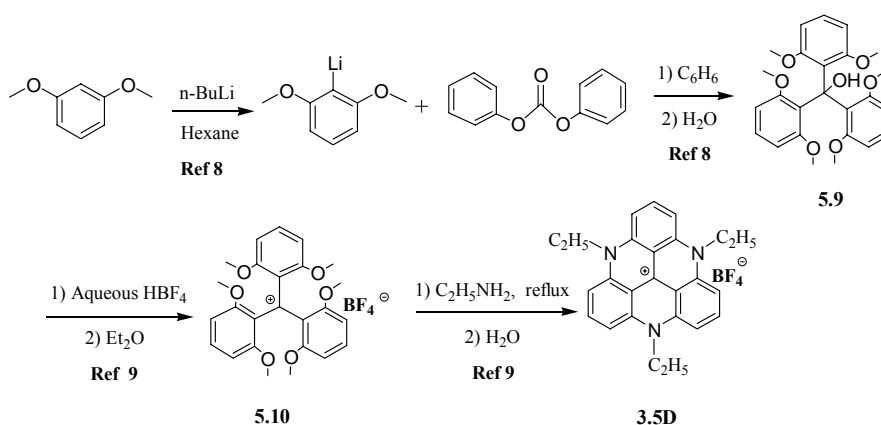


Figure 5.6. Synthesis of 4,8,12-Triethyl-4,8,12-triazatriangulenium tetrafluoroborate (**3.5D**).

### **2,6,2',6',2'',6'''-Hexamethoxytriphenylcarbinol (5.9)**

Under argon protection, 30 mL 2.5 M hexane solution of butyllithium (72.7 mmol), 10 mL (76.4 mmol) resorcinol dimethyl ether and 0.3 mL N,N,N',N'-tetramethylethylenediamine (TMEDA) were added to a 250 mL round bottom flask at 0 °C. The temperature was allowed to rise to room temperature for 30 min. The mixture was diluted with 60 mL benzene. 4.96 g (23 mmol) diphenyl carbonate in 60 mL benzene was triturated into the solution. The mixture was refluxed at 70-80 °C for 28 hrs. The reaction mixture was washed with 90 x 3 mL water and the organic phase was concentrated. Recrystallized with benzene obtained 7.6 g light yellow crystals of **7**, 71% yield. MS (IE)  $m/z$  423 [M-OH]<sup>+</sup>, <sup>1</sup>H NMR (CDCl<sub>3</sub>, 400 MHz) δ 3.45 (s, 6H), 6.49 (d,  $J$  = 8.2, 6H), 6.85 (s, 1H), 7.05 (t,  $J$  = 8.2, 3H). X-Ray diffraction confirmed connectivity.

### **Tris(2,6-dimethoxyphenyl)carbenium tetrafluoroborate (5.10)**

Tris(2,6-dimethoxyphenyl)carbinol **5.9** (1.6 g, 3.64 mmol) was dissolved in 30 mL absolute ethanol in a 100 mL flask. 1.5 mL 48% aqueous HBF<sub>4</sub> solution (11 mmol) was added, followed by 30 mL diethyl ether and petroleum ether. The mixture was filtered and dark-blue precipitate was washed with diethyl ether (3 x 10 mL) and dried. 1.8 g greenish-black solid was collected (99%). <sup>1</sup>H NMR (DMSO, 400 MHz) δ 3.60 (s, 18H), 6.54 (d,  $J$  = 8.4, 6H), 7.61 (t,  $J$  = 8.4, 3H).

### **4,8,12-Triethyl-4,8,12-triazatriangulenium tetrafluoroborate (3.5D)**

0.78 g (1.6 mmol) **5.10** was dissolved in 20 mL NMP (1-methyl-2-pyrrolidinone) in a 100 mL round bottom flask. 4.1 g benzoic acid (33.6 mmol) followed by 4.0 g ethylamine (67.2 mmol) were added. The mixture was reflux with dry ice condenser under argon at 135-150 °C for 22 hrs. Two times ethylamine (1.5 and 2.3 g) was further added. After the mixture was cooled down, it was poured into 100 mL cold water. The mixture was filtered and washed 3 x 10 mL with water, dried. The red powder was further washed with diethyl ether. Recrystallization from CH<sub>3</sub>CN yielded 0.16 g dark red crystal, 23.4%. MS (IE)  $m/z$  366 [M-BF<sub>4</sub>]<sup>+</sup>; <sup>1</sup>H NMR (400 MHz, DMSO):

$\delta$  8.00 (t,  $J = 8.4$  Hz, 3H), 7.28 (d,  $J = 8.4$  Hz, 6H), 4.31 (q,  $J = 6.8$  Hz, 6H), 1.33 (t,  $J = 6.8$  Hz, 9H);  $^{13}\text{C}$  NMR (100 MHz, DMSO):  $\delta$  139.5, 137.8, 109.7, 104.9, 42.3, 10.2; X-Ray diffraction confirmed connectivity.

#### **4,8,12-Tri-*n*-propyl-4,8,12-triazatriangulenium tetrafluoroborate (3.6D)**

0.7 g (1.4 mmol) **5.10** was dissolved in 25 mL NMP (1-methyl-2-pyrrolidinone) in a 100 mL round bottom flask. 3.6 g benzoic acid (29.2 mmol) followed by 2.3 g *n*-propylamine (38.8 mmol) were added. The mixture was reflux under argon at 125 °C for 20 hrs. 4 x 1.0 mL *n*-propylamine (24.3 mmol) was further added. After the mixture was cooled down, it was poured into 50 mL cold water. The mixture was filtered and washed 3 x 10 mL with water, dried. The red powder was further washed with 3 x 10 mL diethyl ether. Recrystallization from CH<sub>3</sub>CN yielded 0.24 g dark red crystal, 24.8%. MS (IE)  $m/z$  408 [M-BF<sub>4</sub>]<sup>+</sup>. mp 337 °C;  $^1\text{H}$  NMR (400 MHz, DMSO):  $\delta$  8.00 (t,  $J = 8.8$  Hz, 3H), 7.30 (d,  $J = 8.8$  Hz, 6H), 4.22 (m, 6H), 1.76 (m, 6H), 1.10 (t,  $J = 7.2$  Hz, 9H);  $^{13}\text{C}$  NMR (100 MHz, DMSO):  $\delta$  141.2, 138.7, 111.2, 106.2, 106.1, 50.1, 19.1, 11.1; X-Ray diffraction confirmed connectivity.

#### **4,8,12-Trimethyl-4,8,12-triazatriangulenium tetrafluoroborate (3.4C)<sup>(10)</sup>**

2.00 g (3.9 mmol) **5.10** was dissolved in 40 mL NMP (1-methyl-2-pyrrolidinone) in a 100 mL round bottom flask. 13.02 g benzoic acid (10.7 mmol) followed by 4.6 g methylamine (148.4 mmol) were added. The mixture was reflux with dry ice condenser under argon at 105 °C for 10 hrs. 4 x 5.0 mL methylamine was further added. After the mixture was cooled down, it was poured into 200 mL 0.1M KPF<sub>6</sub> aqueous solution, which was acidified with 3.7g 60% HPF<sub>6</sub> aqueous solution. The mixture was stirred overnight filtered. The precipitation was recrystallized from CH<sub>3</sub>CN yielded 0.12 g dark red crystal, 9.5%. MS (IE)  $m/z$  324 [M- PF<sub>6</sub>]<sup>+</sup>;  $^1\text{H}$  NMR (400 MHz, DMSO):  $\delta$  7.95 (t,  $J = 8.4$  Hz, 3H), 7.04 (d,  $J = 8.4$  Hz, 6H), 3.52 (s, 9H);  $^{13}\text{C}$  NMR (100 MHz, DMSO):  $\delta$  139.1, 137.3, 137.1, 107.8, 105.0, 34.7.

### 4,8,12-Tri-*n*-propyl-4,8,12-triazatriangulenium

### 4,8-Dioxo-4H-8H-dibenzo[cd,mn]pyren-12-olate (**3.16**)

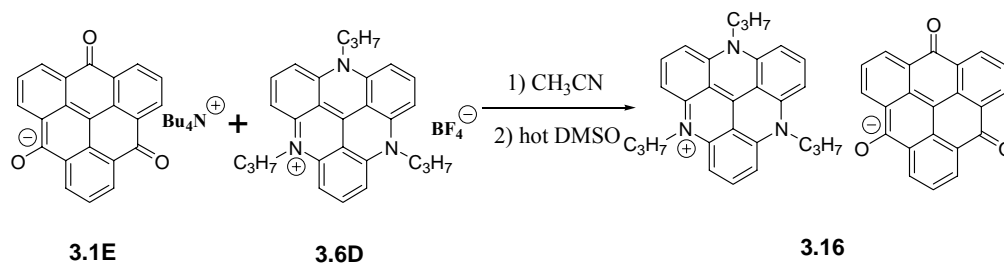


Figure 5.7. 4,8,12-Tri-*n*-propyl-4,8,12-triazatriangulenium  
4,8-Dioxo-4H-8H-dibenzo[cd,mn]pyren-12-olate (**3.16**).

16 mg (0.032 mmol) tri-*n*-propyltriangulenium (**3.6D**) and 18 mg (0.032 mmol) trioxo-4H-8H-dibenzo[cd,mn]pyren-12-olate (**3.1E**) were dissolved separately in two 2 mL CH<sub>3</sub>CN solution. These two solutions were mixed and dark brown precipitation was formed. The mixture was filtered and washed with 3 x 0.5 mL CH<sub>3</sub>CN. The solid was dried and recrystallized in hot DMSO solution. 20 mg needle-like crystal was acquired, 85.7%. Crystal was melt ~337 °C and decomposed ~380 °C. X-Ray diffraction confirmed connectivity.

## References

- 1) Z. Otwinowski, W. Minor, "Processing of X-ray Diffraction Data Collected in Oscillation Mode", 276: Macromolecular Crystallography Part A. Methods in Enzymology, (Eds.: C. W. Carter, Jr., R. M. Sweet), Academic Press, New York, **1997**, pp. 307-326.
- 2) International Tables for Crystallography, vol C: Mathematical, Physical and Chemical Tables, (Ed.: T. H. Hahn), Kluwer Academic Publishers, Holland, **1992**.
- 3) J. Chen, A. Cammers-Goodwin, *Tetrahedron Lett.* **2003**, *44*, 1503-1506.
- 4) J. Chen, A. Cammers-Goodwin, *Eur. J. Org. Chem.* **2003**, *19*, 3861-3867.
- 5) L. Chahen, H. Doucet, M. Santelli, *Synlett.* **2003**, *11*, 1668-1672.
- 6) G. Allinson, R. Bushby, J. Paillaud, M. Thornton-Pett, *J. Chem. Soc., Perkin trans. I.* **1995**, *4*, 385-390.
- 7) E. Clar, D. G. Stewart, *J. Am. Chem. Soc.* **1953**, *75*, 2667-2672.
- 8) M. Wada, H. Mishima, T. Watanabe, S. Natsume, H. Konishi, K. Kirishima, S. Hayase, T. Erabi, *Bull. Chem. Soc. Jpn.* **1995**, *68*, 243-249.
- 9) B. W. Laursen, F. C. Krebs, *Chem. Euro. J.* **2001**, *7*, 1773-1783.
- 10) B. W. Laursen, F. C. Krebs, *Angew. Chem., Int. Ed.* **2000**, *39*, 3432-3434.

**Appendices**  
**A-1: Crystal data for 2b and 2c.**

<b>Compound</b>	<b>2b</b>	<b>2c</b>
formula	C <sub>30</sub> H <sub>20</sub> F <sub>6</sub> N <sub>2</sub>	C <sub>30</sub> H <sub>16</sub> F <sub>10</sub> N <sub>2</sub>
formula weight	522.48	594.45
crystal system	triclinic	monoclinic
space group	P-1	P 21/c
a(Å)	9.8280(3)	14.009(3)
b(Å)	13.0840(4)	12.981(3)
c(Å)	14.2130(5)	15.554(3)
α(°)	78.7500(19)	90.00
β(°)	88.0420(19)	93.29(3)
γ(°)	82.200(2)	90.00
volume(Å <sup>3</sup> )	1775.89(10)	2824.0(10)
Z	2	4
temperature(K)	90.0(2)	90.0(2)
reflections used	34244	20524
θ measurement range (°)	1-27.48	1-25.35
crystal description	irregular plate	broken plate
color	pale yellow	yellow
crystal size(mm <sup>3</sup> )	0.45x0.20x0.05	0.45x0.22x0.04
crystal density (Mg/m <sup>3</sup> )	1.549	1.774
F(000)	836	1480
absorption coefficient (mm <sup>-1</sup> )	2.352	2.962
data/ parameters / restraints	8137/456/0	3687/378/397
R <sub>1</sub>	0.0598	0.0524
R <sub>all</sub>	0.097	0.0894
goodness-of-fit	1.101	1.025
school XRD file codes	k02080	k02078



### A-2: Crystal coordinates of 2b.

atom/axis	X	Y	Z
N	0.3662	-0.1167	0.307
N	-0.0217	0.3864	0.3158
C	0.4877	-0.077	0.3122
C	0.5944	-0.1397	0.3636
H	0.6795	-0.1138	0.3667
C	0.5785	-0.2407	0.4108
H	0.6511	-0.2826	0.4486
C	0.4569	-0.2801	0.403
H	0.4456	-0.3499	0.4333
C	0.3523	-0.2159	0.3502
H	0.2683	-0.2422	0.3443
C	0.2437	-0.0477	0.261
H	0.1689	-0.0904	0.2571
H	0.2674	-0.014	0.195
C	0.1957	0.036	0.3195
C	0.1755	0.1419	0.2763
H	0.1914	0.1624	0.2094
C	0.1319	0.2175	0.3309
C	0.1123	0.1872	0.4289
H	0.0868	0.239	0.4669
C	0.1297	0.0821	0.4716
H	0.1134	0.0616	0.5385
C	0.171	0.0067	0.4167
H	0.1825	-0.0656	0.446
C	0.1107	0.3322	0.283
H	0.188	0.367	0.2987
H	0.1092	0.3381	0.2125
C	-0.1449	0.3543	0.3005
C	-0.2628	0.4005	0.3381
H	-0.3485	0.3785	0.3278
C	-0.2586	0.4782	0.3903
H	-0.3403	0.5086	0.4173
C	-0.1336	0.5115	0.4028
H	-0.1286	0.5664	0.437
C	-0.0176	0.4642	0.3651
H	0.0683	0.4867	0.3738
C	-0.1437	0.2719	0.2416
F	-0.1897	0.1452	0.3759

C	-0.162	0.1681	0.2814
C	-0.1496	0.0886	0.2293
H	-0.1602	0.0183	0.2583
F	-0.1065	0.0405	0.0802
C	-0.1212	0.1165	0.1337
C	-0.1055	0.2173	0.0876
H	-0.0869	0.234	0.0207
F	-0.1047	0.393	0.1024
C	-0.1185	0.2924	0.1443
C	0.4974	0.0326	0.2637
F	0.5114	-0.0124	0.1123
C	0.51	0.0629	0.165
C	0.5189	0.164	0.118
H	0.5292	0.1817	0.0503
F	0.5204	0.3395	0.1323
C	0.5119	0.2379	0.1755
C	0.4975	0.2166	0.2732
H	0.4909	0.2704	0.31
F	0.4805	0.0881	0.4112
C	0.4931	0.1132	0.3151
N	0.7474	0.7172	0.0797
O	0.8032	0.6813	-0.0676
C	0.7649	0.6567	0.0146
H	0.7453	0.5865	0.0344
C	0.6938	0.6835	0.1757
H	0.6764	0.6103	0.1839
H	0.6078	0.7283	0.1848
H	0.7609	0.6893	0.2232
C	0.7754	0.8254	0.0556
H	0.8206	0.8376	-0.0074
H	0.8355	0.8389	0.1041
H	0.6889	0.8728	0.0537
N	0.2573	0.6481	0.122
O	0.362	0.7964	0.1099
C	0.2626	0.7483	0.1286
H	0.1814	0.7857	0.1499
C	0.1362	0.5978	0.1515
H	0.0642	0.649	0.1714
H	0.159	0.5392	0.2054
H	0.1034	0.5712	0.0977
C	0.3784	0.5829	0.0961

H	0.4506	0.6269	0.0735
H	0.3557	0.5477	0.0449
H	0.411	0.53	0.1523
Br	0.3676	0.4586	0.381
Br	0.0321	0.2166	0.6794

### A-3: Crystal coordinates of 2c.

atom/axis	X	Y	Z
N	0.7452	-0.0099	0.4392
C	0.6811	0.0692	0.4303
C	0.6143	0.0696	0.3627
H	0.5709	0.1255	0.3552
C	0.6101	-0.0124	0.305
H	0.5614	-0.0148	0.26
C	0.6762	-0.0893	0.3134
H	0.6755	-0.1443	0.273
C	0.7441	-0.0862	0.3811
H	0.7909	-0.1391	0.3866
C	0.8108	-0.0171	0.5178
H	0.8462	0.0485	0.5261
H	0.858	-0.0727	0.5104
C	0.7556	-0.039	0.5963
C	0.7773	0.0129	0.6729
H	0.8265	0.0633	0.6754
C	0.7283	-0.0076	0.7456
C	0.6558	-0.08	0.7421
H	0.6214	-0.0937	0.7917
C	0.6334	-0.1325	0.6662
H	0.5843	-0.1831	0.6639
C	0.6824	-0.1111	0.594
H	0.6658	-0.1463	0.5417
C	0.7523	0.0488	0.8282
H	0.6998	0.097	0.8399
H	0.8113	0.0897	0.8226
N	0.7667	-0.0252	0.902
C	0.8436	-0.0893	0.9092
C	0.8549	-0.1553	0.9768
H	0.9092	-0.1991	0.9817
C	0.788	-0.1589	1.0382
H	0.7965	-0.2039	1.0862
C	0.7086	-0.0967	1.029
H	0.6605	-0.1003	1.0696
C	0.6992	-0.0299	0.9618
H	0.6449	0.014	0.9564
C	0.9151	-0.0837	0.8421

F	0.991	0.0576	0.9118
C	0.9881	-0.0122	0.8477
F	1.1306	0.057	0.7984
C	1.0597	-0.0112	0.7909
F	1.1261	-0.0831	0.6704
C	1.0569	-0.0825	0.7258
F	0.981	-0.2217	0.6521
C	0.9835	-0.1538	0.7167
F	0.8418	-0.2218	0.7652
C	0.9145	-0.1537	0.7752
C	0.6864	0.1546	0.4942
F	0.5425	0.0998	0.5511
C	0.6159	0.1663	0.5514
C	0.6183	0.2465	0.6103
F	0.5471	0.258	0.6634
F	0.6962	0.3928	0.6692
C	0.6933	0.3145	0.6124
F	0.8341	0.3762	0.5554
C	0.7637	0.3062	0.5558
F	0.8246	0.2239	0.4385
C	0.7591	0.2282	0.4968
Br	1.0042	-0.3502	0.8921
Br	0.4776	-0.3513	0.6171

**A-4: Crystal data for 5.1 and 5.2.**

<b>Compound</b>	<b>5.1</b>	<b>5.2</b>
formula	C <sub>11</sub> H <sub>6</sub> F <sub>3</sub> N	C <sub>11</sub> H <sub>4</sub> F <sub>5</sub> N
formula weight	209.17	245.15
crystal system	monoclinic	monoclinic
space group	P 21/c	P 21
a(Å)	8.1930(4)	5.6710(3)
b(Å)	10.8610(5)	7.6920(5)
c(Å)	10.5980(5)	10.7540(6)
α(°)	90.00	90.00
β(°)	109.719(3)	104.790(3)
γ(°)	90.00	90.00
volume(Å <sup>3</sup> )	887.75(7)	453.56(5)
Z	4	2
temperature(K)	90.0(2)	90.0(2)
reflections used	6193	5356
θ measurement range (°)	1-27.48	1-27.48
crystal description	irregular slab	plates
color	colorless	colorless
crystal size(mm <sup>3</sup> )	0.25x0.23x0.08	0.30x0.17x0.03
crystal density (Mg/m <sup>3</sup> )	1.565	1.795
F(000)	424	244
absorption coefficient (mm <sup>-1</sup> )	0.137	0.179
data/ parameters / restraints	2044/137/0	2055/155/1
R <sub>1</sub>	0.0474	0.0439
R <sub>all</sub>	0.0766	0.0637
goodness-of-fit	1.017	1.049
school XRD file codes	k02070	k02056

### A-5: Crystal coordinates of 5.1.

atom/axis	X	Y	Z
N	0.3069	0.1286	0.9622
C	0.3242	0.2358	0.9041
C	0.4566	0.3192	0.9644
H	0.4658	0.3938	0.9205
C	0.5749	0.2914	1.0899
H	0.6656	0.3472	1.1339
C	0.5584	0.1814	1.1494
H	0.638	0.1595	1.2348
C	0.4237	0.1037	1.0823
H	0.4134	0.0281	1.124
C	0.191	0.2605	0.7712
C	0.1024	0.3724	0.7397
C	-0.0259	0.3991	0.621
H	-0.0836	0.4764	0.605
C	-0.0657	0.3072	0.5264
C	0.013	0.1935	0.5464
H	-0.0185	0.1315	0.4793
C	0.1398	0.1744	0.6686
F	0.1448	0.4623	0.8355
F	-0.1904	0.3298	0.4059
F	0.2214	0.0636	0.6878

### A-6: Crystal coordinates of 5.2.

atom/axis	X	Y	Z
N	1.1463	0.1575	0.9142
C	0.9818	0.2244	0.9726
C	0.7592	0.2907	0.9067
H	0.6492	0.3365	0.9518
C	0.6985	0.2895	0.7732
H	0.5466	0.3348	0.7252
C	0.8628	0.2213	0.7115
H	0.8264	0.2189	0.6203
C	1.0822	0.1564	0.7852
H	1.1935	0.1085	0.7419
C	1.0552	0.2237	1.1158
C	1.2717	0.2987	1.1854
C	1.34	0.2979	1.3192
C	1.193	0.2193	1.3855
C	0.9775	0.1436	1.3195
C	0.9106	0.1468	1.1878
F	1.4181	0.3812	1.125
F	1.5481	0.3761	1.3831
F	1.2589	0.2169	1.5151
F	0.8349	0.0632	1.3857
F	0.7022	0.067	1.1276



**A-7: Crystal data for 2e and 3.16.**

<b>Compound</b>	<b>2e</b>	<b>3.16</b>
formula	C <sub>32</sub> H <sub>26</sub>	C <sub>50</sub> H <sub>39</sub> N <sub>3</sub> O <sub>3</sub>
formula weight	410.53	729.84
crystal system	orthorhombic	triclinic
space group	Pbca	P-1
a(Å)	7.4995(11)	8.1193(2)
b(Å)	19.420(3)	10.5975(3)
c(Å)	30.314(4)	20.8300(6)
α(°)	90.00	85.5030(10)
β(°)	90.00	81.8080(10)
γ(°)	90.00	74.2940(10)
volume(Å <sup>3</sup> )	4415.0(11)	1706.29(8)
Z	8	2
temperature(K)	90.0(2)	90.0(2)
reflections used	1477	6218
θ measurement range (°)	4.6-66.25	1.00-25.35
crystal description	plate	very thin plate
color	colorless	dark blue
crystal size(mm <sup>3</sup> )	0.25x0.20x0.03	0.20x0.12x0.02
crystal density (Mg/m <sup>3</sup> )	1.235	1.421
F(000)	1744	768
absorption coefficient (mm <sup>-1</sup> )	0.524	0.089
data/ parameters / restraints	3962/290/0	6027/508/168
R <sub>1</sub>	0.0494	0.0589
R <sub>all</sub>	0.0836	0.1662
goodness-of-fit	1.013	0.958
school XRD file codes	x04071	k03052

**A-8: Crystal coordinates of 2e.**

atom/axis	X	Y	Z
C	0.3014	0.1943	0.6671
C	0.2202	0.1458	0.6945
H	0.2607	0.0994	0.6943
C	0.0811	0.1645	0.7221
H	0.0268	0.1309	0.7405
C	0.0203	0.232	0.7231
H	-0.0743	0.2449	0.7422
C	0.0994	0.2802	0.6958
H	0.0578	0.3264	0.6959
C	0.2388	0.2617	0.6681
H	0.2922	0.2954	0.6497
C	0.4541	0.1747	0.6379
C	0.6238	0.2007	0.6472
H	0.6394	0.2303	0.6718
C	0.7697	0.1843	0.6212
H	0.8836	0.2031	0.6277
C	0.7482	0.14	0.5856
H	0.8476	0.1279	0.5678
C	0.5818	0.1138	0.5764
H	0.5683	0.0834	0.5521
C	0.4324	0.1306	0.6017
C	0.252	0.1049	0.5864
H	0.258	0.0546	0.5814
H	0.1627	0.1136	0.6098
C	0.1937	0.1401	0.5444
C	0.1548	0.2104	0.5444
H	0.1659	0.2361	0.571
C	0.1003	0.2429	0.5061
H	0.0709	0.2905	0.5067
C	0.0884	0.2064	0.4672
H	0.0532	0.2293	0.4409
C	0.1275	0.1365	0.4659
C	0.1793	0.1042	0.505
H	0.2054	0.0564	0.5046
C	0.1102	0.0971	0.4234
H	0.1666	0.0514	0.4272
H	0.1774	0.1219	0.4002
C	-0.08	0.0866	0.4075

C	-0.2262	0.0982	0.4348
H	-0.2071	0.1133	0.4642
C	-0.3993	0.0881	0.4199
H	-0.4971	0.0967	0.4391
C	-0.4297	0.0656	0.3775
H	-0.5479	0.0584	0.3672
C	-0.2856	0.0536	0.35
H	-0.3064	0.0379	0.3208
C	-0.1109	0.0638	0.3641
C	0.0408	0.0494	0.3336
C	0.118	-0.0155	0.3326
H	0.0749	-0.0503	0.3518
C	0.2568	-0.0304	0.3039
H	0.3078	-0.0752	0.3037
C	0.3214	0.0194	0.2757
H	0.4163	0.0092	0.256
C	0.2465	0.0847	0.2765
H	0.2902	0.1194	0.2572
C	0.1079	0.0996	0.3052
H	0.058	0.1445	0.3055

### A-9: Crystal coordinates of 3.16.

atom/axis	X	Y	Z
N	0.0119	0.0878	0.1706
C	0.132	-0.0193	0.1432
C	0.2277	-0.0097	0.0823
H	0.2111	0.0717	0.0583
C	0.3458	-0.1196	0.0578
H	0.4105	-0.1119	0.0167
C	0.3749	-0.241	0.0903
H	0.458	-0.3145	0.0715
C	0.2815	-0.2544	0.1507
N	0.3047	-0.3741	0.1857
C	0.2111	-0.3891	0.2462
C	0.2368	-0.508	0.2811
H	0.317	-0.5844	0.2638
C	0.1431	-0.5135	0.342
H	0.1649	-0.5944	0.3665
C	0.0198	-0.4075	0.3686
H	-0.0398	-0.4151	0.4108
C	-0.0158	-0.2888	0.3325
N	-0.15	-0.1822	0.3537
C	-0.1793	-0.0616	0.3203
C	-0.3117	0.0458	0.3424
H	-0.3837	0.0385	0.3819
C	-0.3369	0.1627	0.3064
H	-0.4304	0.2341	0.3212
C	-0.2331	0.1811	0.2499
H	-0.253	0.264	0.2271
C	-0.0988	0.076	0.2268
C	-0.073	-0.0469	0.2615
C	0.1573	-0.1432	0.177
C	0.0847	-0.2772	0.2722
C	0.057	-0.1556	0.2373
C	0.0014	0.2196	0.14
H	0.1177	0.2233	0.1193
H	-0.0362	0.2852	0.174
C	-0.1228	0.2556	0.0892
H	-0.2417	0.2613	0.1103
H	-0.0923	0.1863	0.057
C	-0.1152	0.3865	0.0548

H	-0.1393	0.454	0.0869
H	-0.2014	0.4113	0.0244
H	0	0.3786	0.0309
C	0.4048	-0.4925	0.1515
H	0.445	-0.5646	0.1835
H	0.5074	-0.4746	0.1246
C	0.2934	-0.5336	0.1085
H	0.2342	-0.4556	0.0832
H	0.2039	-0.5673	0.1363
C	0.397	-0.6387	0.0617
H	0.4887	-0.6072	0.0351
H	0.3206	-0.6577	0.0335
H	0.4482	-0.7187	0.0865
C	-0.272	-0.2008	0.4108
H	-0.2753	-0.2938	0.414
H	-0.3886	-0.1468	0.4035
C	-0.2328	-0.1663	0.4749
H	-0.2434	-0.071	0.4748
H	-0.1132	-0.214	0.4816
C	-0.3584	-0.2038	0.5292
H	-0.4767	-0.1606	0.5209
H	-0.3387	-0.1759	0.5706
H	-0.3409	-0.2992	0.5313
O	-0.6228	0.1882	0.1932
O	-0.1599	-0.4946	0.209
O	-0.8035	-0.2207	0.4713
C	-0.5994	0.0773	0.2212
C	-0.4636	-0.0359	0.195
C	-0.3601	-0.0213	0.1373
H	-0.3794	0.0622	0.1152
C	-0.2295	-0.1246	0.1109
H	-0.1591	-0.112	0.0717
C	-0.204	-0.2465	0.1429
H	-0.1163	-0.318	0.1247
C	-0.303	-0.2676	0.2011
C	-0.2682	-0.398	0.2339
C	-0.3668	-0.4095	0.2981
C	-0.3233	-0.5257	0.3356
H	-0.2303	-0.596	0.3192
C	-0.4124	-0.5409	0.3959
H	-0.3813	-0.6209	0.4207

C	-0.5481	-0.4381	0.4202
H	-0.6109	-0.4496	0.4614
C	-0.594	-0.3191	0.3857
C	-0.7288	-0.2093	0.4154
C	-0.7667	-0.0846	0.3768
C	-0.898	0.0211	0.4009
H	-0.9642	0.0105	0.4414
C	-0.9348	0.1416	0.3672
H	-1.0255	0.2126	0.3843
C	-0.8373	0.157	0.3083
H	-0.8623	0.2393	0.285
C	-0.704	0.0547	0.2825
C	-0.6682	-0.0705	0.3155
C	-0.4357	-0.1604	0.2287
C	-0.5016	-0.3016	0.3232
C	-0.5361	-0.1781	0.2888

**A-10: Crystal data for 3.1 and 3.6.**

<b>Compound</b>	<b>3.1</b>	<b>3.6</b>
formula	C <sub>38</sub> H <sub>46</sub> NO <sub>3</sub>	C <sub>28</sub> H <sub>31</sub> BF <sub>4</sub> N <sub>3</sub>
formula weight	564.78	496.37
crystal system	monoclinic	trigonal
space group	P2 <sub>1</sub> /n	R-3
a(Å)	9.5700(19)	12.8297(18)
b(Å)	18.573(4)	12.8297(18)
c(Å)	17.668(4)	26.367(5)
α(°)	90.00	90.00
β(°)	97.17(3)	90.00
γ(°)	90.00	120.00
volume(Å <sup>3</sup> )	3115.78	3758.5(11)
Z	4	6
temperature(K)	90.0(2)	90.0(2)
reflections used	14252	11034
θ measurement range (°)	1.00-27.48	1.00-27.48
crystal description	block	irregular slab
color	dark blue	red
crystal size(mm <sup>3</sup> )	0.3x0.3x0.2	0.25x0.22x0.10
crystal density (Mg/m <sup>3</sup> )	NA	1.368
F(000)	NA	1626
absorption coefficient (mm <sup>-1</sup> )	0.1468	0.101
data/ parameters / restraints	7149/392/0	1906/164/95
R <sub>1</sub>	0.1043	0.0513
R <sub>all</sub>	0.1330	0.0674
goodness-of-fit	NA	1.041
school XRD file codes	k03049	k03063

### A-11: Crystal coordinates of 3.1.

atom/axis	X	Y	Z
C	-0.0791	0.0611	0.9023
H	-0.0599	0.0117	0.9131
C	-0.1535	0.1008	0.9488
H	-0.1838	0.0789	0.9925
C	-0.1855	0.1728	0.9331
C	-0.2686	0.2135	0.9835
C	-0.3111	0.2861	0.9594
C	-0.4036	0.3245	0.9993
H	-0.4377	0.3028	1.0421
C	-0.4463	0.3925	0.9784
H	-0.5124	0.4165	1.0054
C	-0.3939	0.4273	0.9179
H	-0.422	0.4752	0.905
C	-0.2987	0.391	0.8757
C	-0.2457	0.4277	0.8114
C	-0.1588	0.3849	0.7655
C	-0.1105	0.4161	0.7017
H	-0.1364	0.4642	0.688
C	-0.0245	0.3776	0.6581
H	0.0098	0.3995	0.6154
C	0.0104	0.3071	0.6773
H	0.0689	0.281	0.6473
C	-0.0383	0.2734	0.7396
C	-0.0034	0.1984	0.7561
C	-0.0589	0.1652	0.822
C	-0.0314	0.0932	0.8389
H	0.0205	0.0655	0.8069
C	-0.1387	0.2069	0.8682
C	-0.2589	0.3193	0.8952
C	-0.1237	0.3129	0.7858
C	-0.1723	0.2795	0.8505
O	-0.303	0.1874	1.0426
O	-0.2723	0.4926	0.7954
O	0.0701	0.1626	0.7156
C	-0.6244	0.1176	0.6473
H	-0.7119	0.1089	0.6704
H	-0.6514	0.1419	0.5978
C	-0.5602	0.0461	0.6324



H	-0.5342	0.0205	0.6812
H	-0.4735	0.0536	0.6082
C	-0.6646	0.0003	0.5799
H	-0.7538	-0.0031	0.6027
H	-0.6855	0.0254	0.5303
C	-0.6153	-0.0735	0.5656
H	-0.5234	-0.0711	0.5467
H	-0.6833	-0.0972	0.5275
H	-0.6066	-0.1011	0.6133
C	-0.4825	0.1344	0.7754
H	-0.4296	0.1705	0.8088
H	-0.4165	0.0949	0.7672
C	-0.6	0.104	0.8166
H	-0.6763	0.1401	0.8163
H	-0.6397	0.0605	0.7896
C	-0.544	0.0847	0.8989
H	-0.5151	0.1293	0.9274
H	-0.4597	0.0538	0.8992
C	-0.6538	0.0455	0.9388
H	-0.7407	0.074	0.9344
H	-0.6181	0.0389	0.9928
H	-0.6735	-0.0016	0.9148
C	-0.6221	0.2356	0.7093
H	-0.7147	0.2193	0.7224
H	-0.6389	0.2613	0.6599
C	-0.5589	0.2891	0.7708
H	-0.5565	0.2667	0.8218
H	-0.461	0.3008	0.7626
C	-0.6466	0.3583	0.7677
H	-0.7474	0.3453	0.7647
H	-0.621	0.3856	0.8155
C	-0.6265	0.4049	0.7026
H	-0.526	0.4153	0.703
H	-0.6781	0.4501	0.7064
H	-0.6621	0.3804	0.6549
C	-0.3999	0.1894	0.6644
H	-0.341	0.1457	0.6627
H	-0.3455	0.2245	0.6985
C	-0.4247	0.2214	0.5845
H	-0.4853	0.2646	0.5846
H	-0.4735	0.1859	0.5487

C	-0.284	0.242	0.5584
H	-0.2385	0.2794	0.5929
H	-0.2216	0.1993	0.5621
C	-0.3	0.27	0.4769
H	-0.3252	0.2301	0.4415
H	-0.2108	0.2913	0.4662
H	-0.3742	0.3066	0.4705
N	-0.5315	0.1693	0.6993
O	-0.3713	0.591	0.8788

### A-12: Crystal coordinates of 3.6.

atom/axis	X	Y	Z
N	0.9468	0.7602	0.0622
C	0.8526	0.7839	0.0626
C	0.7325	0.6923	0.0628
H	0.7126	0.6103	0.0623
C	0.6428	0.7218	0.0638
H	0.5614	0.6584	0.0639
C	0.6654	0.8391	0.0645
H	0.6008	0.8553	0.0658
C	0.7843	0.9335	0.0632
C	0.8791	0.906	0.0626
C	1	1	0.0624
C	0.918	0.6334	0.0668
H	0.9837	0.6245	0.0517
H	0.843	0.5806	0.0479
C	0.902	0.595	0.1224
H	0.9749	0.6516	0.1416
H	0.8329	0.5991	0.1368
C	0.8806	0.4678	0.1285
H	0.8112	0.4122	0.108
H	0.8648	0.4442	0.1643
H	0.9521	0.4653	0.1172
N	1.2398	1.1867	0.0622
C	1.2161	1.0687	0.0626
C	1.3077	1.0402	0.0628
H	1.3897	1.1023	0.0623
C	1.2782	0.9209	0.0638
H	1.3416	0.903	0.0639
C	1.1608	0.8263	0.0645
H	1.1447	0.7455	0.0658
C	1.0665	0.8508	0.0632
C	1.094	0.9732	0.0626
C	1.3666	1.2845	0.0668
H	1.3755	1.3592	0.0517
H	1.4194	1.2624	0.0479
C	1.405	1.307	0.1224
H	1.3484	1.3233	0.1416
H	1.4009	1.2338	0.1368
C	1.5322	1.4128	0.1285

H	1.5878	1.399	0.108
H	1.5558	1.4206	0.1643
H	1.5347	1.4868	0.1172
N	0.8133	1.0532	0.0622
C	0.9313	1.1474	0.0626
C	0.9598	1.2675	0.0628
H	0.8977	1.2874	0.0623
C	1.0791	1.3572	0.0638
H	1.097	1.4386	0.0639
C	1.1737	1.3346	0.0645
H	1.2545	1.3992	0.0658
C	1.1492	1.2157	0.0632
C	1.0268	1.1208	0.0626
C	0.7155	1.082	0.0668
H	0.6408	1.0163	0.0517
H	0.7376	1.157	0.0479
C	0.693	1.098	0.1224
H	0.6767	1.0251	0.1416
H	0.7662	1.1671	0.1368
C.	0.5872	1.1194	0.1285
H	0.601	1.1888	0.108
H	0.5794	1.1352	0.1643
H	0.5132	1.0479	0.1172
B	0.6667	0.3333	-0.0095
F	0.6378	0.4194	0.003
F	0.6667	0.3333	-0.0616
F	0.5806	0.2184	0.003
F	0.7816	0.3622	0.003
N	0.4398	0.831	0.1546
C	0.387	0.737	0.158
C	0.259	0.636	0.1673
N	0.169	0.6088	0.1546
C	0.263	0.65	0.158
C	0.364	0.623	0.1673
N	0.3912	0.5602	0.1546
C	0.35	0.613	0.158
C	0.377	0.741	0.1673
N	0.2269	0.5023	0.1787
C	0.2797	0.5963	0.1753
C	0.4077	0.6973	0.166
N	0.4977	0.7245	0.1787

C	0.4037	0.6833	0.1753
C	0.3027	0.7103	0.166
N	0.2755	0.7731	0.1787
C	0.3167	0.7203	0.1753
C	0.2897	0.5923	0.166
F	0.7497	0.3562	0.0283
F	0.7401	0.3563	-0.0511
F	0.629	0.4163	-0.0114

**A-13: Crystal data for 3.5 and 5.5.**

<b>Compound</b>	<b>3.5</b>	<b>5.5</b>
formula	C <sub>25</sub> H <sub>24</sub> BF <sub>4</sub> N <sub>3</sub>	C <sub>22</sub> H <sub>18</sub> O <sub>2</sub>
formula weight	453.28	314.36
crystal system	triclinic	monoclinic
space group	P-1	P2 <sub>1</sub> /c
a(Å)	8.7073(2)	8.5427(2)
b(Å)	11.2000(3)	7.1453(2)
c(Å)	12.2971(4)	27.5180(10)
α(°)	113.1619(12)	90.00
β(°)	101.3856(12)	93.019(2)
γ(°)	101.7058(11)	90.00
volume(Å <sup>3</sup> )	1027.18(5)	1677.37(9)
Z	2	4
temperature(K)	90.0(2)	90.0(2)
reflections used	4648	5792
θ measurement range (°)	1.00-27.48	1.00-25.35
crystal description	irregular block	irregular bent plate
color	red	colorless
crystal size(mm <sup>3</sup> )	0.30x0.30x0.20	0.48x0.30x0.08
crystal density (Mg/m <sup>3</sup> )	1.466	1.245
F(000)	472	664
absorption coefficient (mm <sup>-1</sup> )	0.112	0.079
data/ parameters / restraints	2683/322/146	3079/219/0
R <sub>1</sub>	0.0627	0.0435
R <sub>all</sub>	0.1037	0.0848
goodness-of-fit	1.059	1.023
school XRD file codes	k03243	k02225

**A-14: Crystal coordinates of 3.5.**

atom/axis	X	Y	Z
N	-0.0753	-0.3057	-0.2168
N	0.1734	-0.0537	0.2306
N	0.3338	0.1397	-0.035
C	-0.1455	-0.4092	-0.0844
H	-0.2168	-0.4908	-0.1545
C	-0.1259	-0.3965	0.0335
H	-0.1855	-0.471	0.0429
C	-0.0247	-0.2817	0.1386
H	-0.0168	-0.277	0.2184
C	0.3922	0.1631	0.3212
H	0.4052	0.1709	0.4024
C	0.4886	0.2627	0.3034
H	0.5691	0.3383	0.374
C	0.4744	0.2587	0.1874
H	0.5435	0.33	0.1792
C	0.2184	0.0106	-0.26
H	0.2838	0.0807	-0.2718
C	0.1106	-0.105	-0.3599
H	0.1029	-0.1124	-0.4406
C	0.0119	-0.212	-0.3506
H	-0.0611	-0.2903	-0.423
C	0.0219	-0.2025	-0.233
C	-0.0591	-0.3007	-0.1001
C	0.0664	-0.1718	0.1273
C	0.2753	0.0506	0.2189
C	0.3576	0.1484	0.0836
C	0.2312	0.0242	-0.1403
C	0.1325	-0.085	-0.1266
C	0.0495	-0.1814	0.0067
C	0.2584	0.0417	0.0983
C	0.1456	-0.0737	-0.0071
C	-0.1877	-0.4292	-0.3268
H	-0.2295	-0.4047	-0.3935
H	-0.2832	-0.4682	-0.3055
C	-0.1016	-0.5358	-0.3738
H	-0.0076	-0.4977	-0.3957
H	-0.1792	-0.6166	-0.4475
H	-0.0625	-0.5619	-0.3087

C	0.1908	-0.0488	0.354
H	0.0824	-0.0943	0.3565
H	0.2284	0.0476	0.4182
C	0.3132	-0.1189	0.3823
H	0.2755	-0.2145	0.3191
H	0.3223	-0.115	0.4644
H	0.4211	-0.0726	0.3817
C	0.4238	0.257	-0.0497
H	0.444	0.3428	0.0257
H	0.3548	0.2618	-0.1213
C	0.5864	0.2446	-0.0704
H	0.6622	0.2562	0.0061
H	0.634	0.3154	-0.0928
H	0.5685	0.1542	-0.1378
B	0.6734	0.6478	0.3297
F	0.5382	0.6884	0.3404
F	0.8069	0.7599	0.3748
F	0.6908	0.5782	0.3993
F	0.6488	0.5644	0.2081
B	0.651	0.648	0.331
F	0.521	0.605	0.228
F	0.584	0.614	0.41
F	0.669	0.783	0.376
F	0.762	0.589	0.301



**A-15: Crystal coordinates of 5.5.**

atom/axis	X	Y	Z
C	0.3407	-0.3175	0.1208
O	0.261	-0.1342	0.1242
O	0.0959	0.0467	0.0793
C	0.1728	-0.0955	0.0827
C	0.1321	-0.2625	0.0002
H	0.0628	-0.171	-0.0138
C	0.1755	-0.4167	-0.0259
H	0.1344	-0.4333	-0.0583
C	0.2786	-0.5486	-0.0053
H	0.3072	-0.6536	-0.0241
C	0.3405	-0.53	0.0421
H	0.4124	-0.6194	0.0558
C	0.2944	-0.377	0.0691
C	0.1938	-0.246	0.0477
C	0.5193	-0.2945	0.1273
C	0.6031	-0.1388	0.1118
C	0.767	-0.1409	0.1193
H	0.8254	-0.0349	0.11
C	0.8453	-0.2917	0.1398
H	0.9562	-0.2885	0.1444
C	0.764	-0.4471	0.1536
H	0.8182	-0.5525	0.1672
C	0.6022	-0.4479	0.1474
H	0.5458	-0.5551	0.1571
C	0.2724	-0.4379	0.1606
C	0.2844	-0.3793	0.2097
C	0.2167	-0.492	0.2441
H	0.2228	-0.4538	0.2772
C	0.1403	-0.6585	0.2317
H	0.0954	-0.7325	0.256
C	0.1305	-0.7148	0.184
H	0.0791	-0.8287	0.1751
C	0.1958	-0.6049	0.1486
H	0.1881	-0.6445	0.1156
C	0.5301	0.03	0.0875
H	0.467	-0.0088	0.0585
H	0.6127	0.1158	0.0781
H	0.4629	0.0934	0.1102

C	0.3663	-0.2021	0.2268
H	0.309	-0.0934	0.2133
H	0.4734	-0.2013	0.2156
H	0.3696	-0.1966	0.2624

**A-16: Crystal data for 5.7 and 5.9.**

<b>Compound</b>	<b>5.7</b>	<b>5.9</b>
formula	C <sub>22</sub> H <sub>16</sub> O <sub>6</sub>	C <sub>25</sub> H <sub>28</sub> O <sub>7</sub>
formula weight	376.36	440.49
crystal system	monoclinic	monoclinic
space group	P2 <sub>1</sub> /n	P2 <sub>1</sub> /n
a(Å)	9.5260(2)	11.8690(2)
b(Å)	15.7690(4)	15.7840(2)
c(Å)	14.4100(4)	16.4100(2)
α(°)	90.00	90.00
β(°)	102.0160(12)	90.3530(7)
γ(°)	90.00	90.00
volume(Å <sup>3</sup> )	2117.18(9)	3074.20(7)
Z	4	4
temperature(K)	90.0(2)	90.0(2)
reflections used	5026	7313
θ measurement range (°)	1.00-27.48	1.00-27.48
crystal description	irregular slab	wedge
color	colorless	colorless
crystal size(mm <sup>3</sup> )	0.25x0.25x0.10	0.30x0.20x0.10
crystal density (Mg/m <sup>3</sup> )	1.325	1.468
F(000)	888	1400
absorption coefficient (mm <sup>-1</sup> )	0.098	0.602
data/ parameters / restraints	4861/285/0	7053/368/0
R <sub>1</sub>	0.0442	0.0348
R <sub>all</sub>	0.0825	0.0548
goodness-of-fit	1.013	1.037
school XRD file codes	k03057	k03024

**A-17: Crystal coordinates of 5.7.**

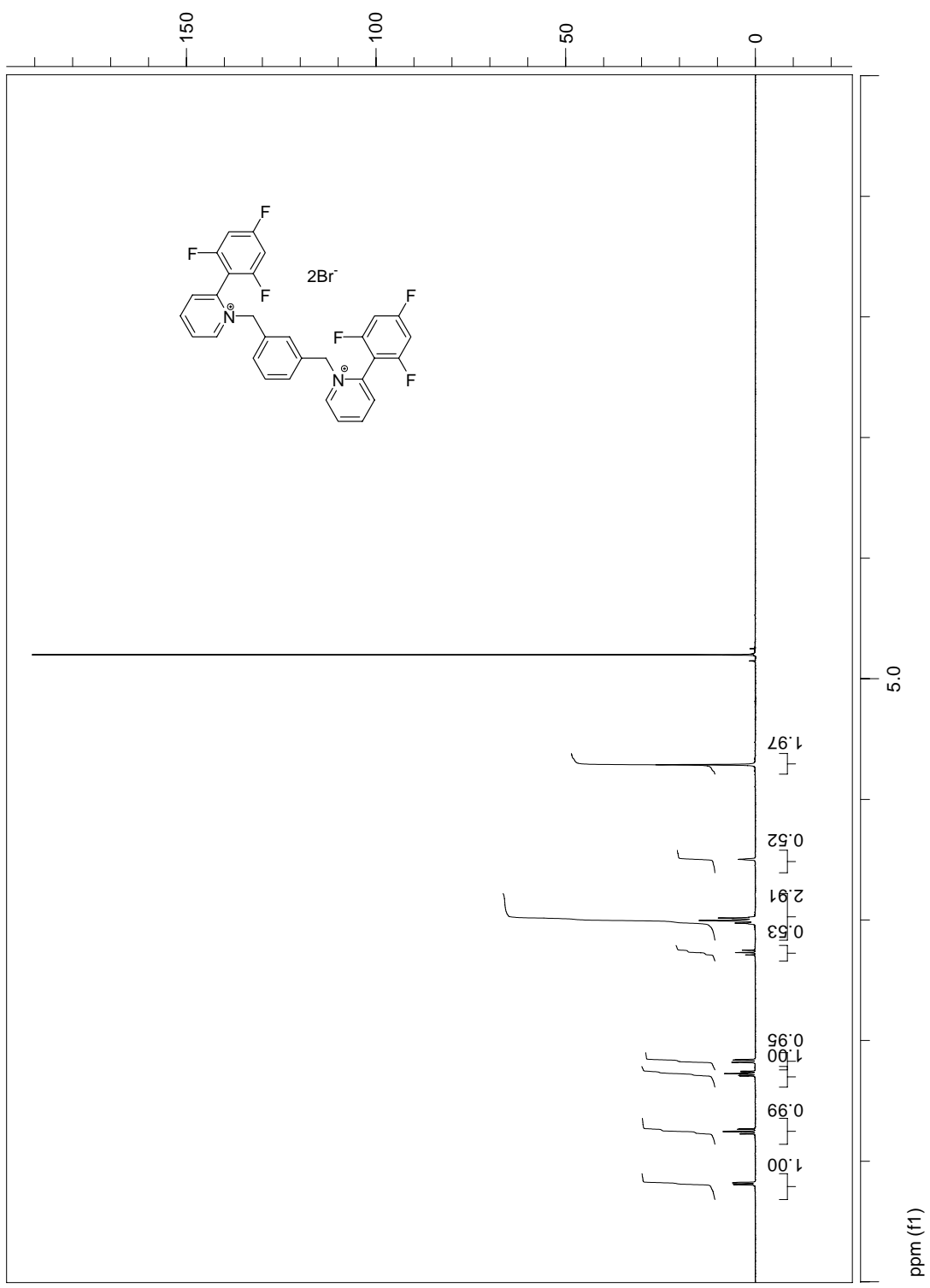
atom/axis	X	Y	Z
O	0.1139	0.1258	0.4509
O	-0.1125	0.1018	0.4649
H	-0.1089	0.0657	0.4227
O	0.1573	0.0286	0.6543
O	0.1434	0.0066	0.8046
H	0.0679	-0.0188	0.7785
O	0.4637	0.0703	0.5692
O	0.5088	0.0931	0.4256
H	0.5245	0.0407	0.4286
C	0.2847	0.1885	0.6279
H	0.2651	0.1343	0.5916
C	0.1388	0.2266	0.6318
C	0.0139	0.2049	0.5652
C	-0.1163	0.2432	0.5701
H	-0.2003	0.2281	0.5251
C	-0.1258	0.3023	0.639
H	-0.2147	0.329	0.6402
C	-0.0044	0.3222	0.7061
H	-0.0101	0.3621	0.7545
C	0.1257	0.2841	0.7031
H	0.2078	0.2975	0.7506
C	0.0135	0.1412	0.4889
C	0.3706	0.1649	0.7265
C	0.3272	0.0972	0.7779
C	0.4071	0.0771	0.8679
H	0.3761	0.0323	0.9028
C	0.5302	0.1213	0.9069
H	0.5845	0.1063	0.9677
C	0.5739	0.1872	0.8571
H	0.659	0.2177	0.8833
C	0.4939	0.2092	0.7685
H	0.524	0.2558	0.7357
C	0.2023	0.0421	0.739
C	0.3661	0.2455	0.571
C	0.4485	0.2113	0.5094
C	0.5124	0.2645	0.4528
H	0.5645	0.2405	0.4097
C	0.5012	0.3517	0.4583

H	0.5466	0.3875	0.4204
C	0.4232	0.3861	0.5199
H	0.4153	0.4459	0.5249
C	0.3562	0.3333	0.5744
H	0.3016	0.3581	0.6155
C	0.473	0.1188	0.5047
O	-0.0946	-0.0693	0.7351
H	-0.1026	-0.0806	0.6773
C	-0.2085	-0.0119	0.7469
H	-0.2022	-0.0017	0.8154
H	-0.3023	-0.0389	0.7211
C	-0.2013	0.0714	0.698
H	-0.1104	0.0996	0.7253
H	-0.2815	0.1073	0.7068
H	-0.2073	0.0617	0.6302

**A-18: Crystal coordinates of 5.9.**

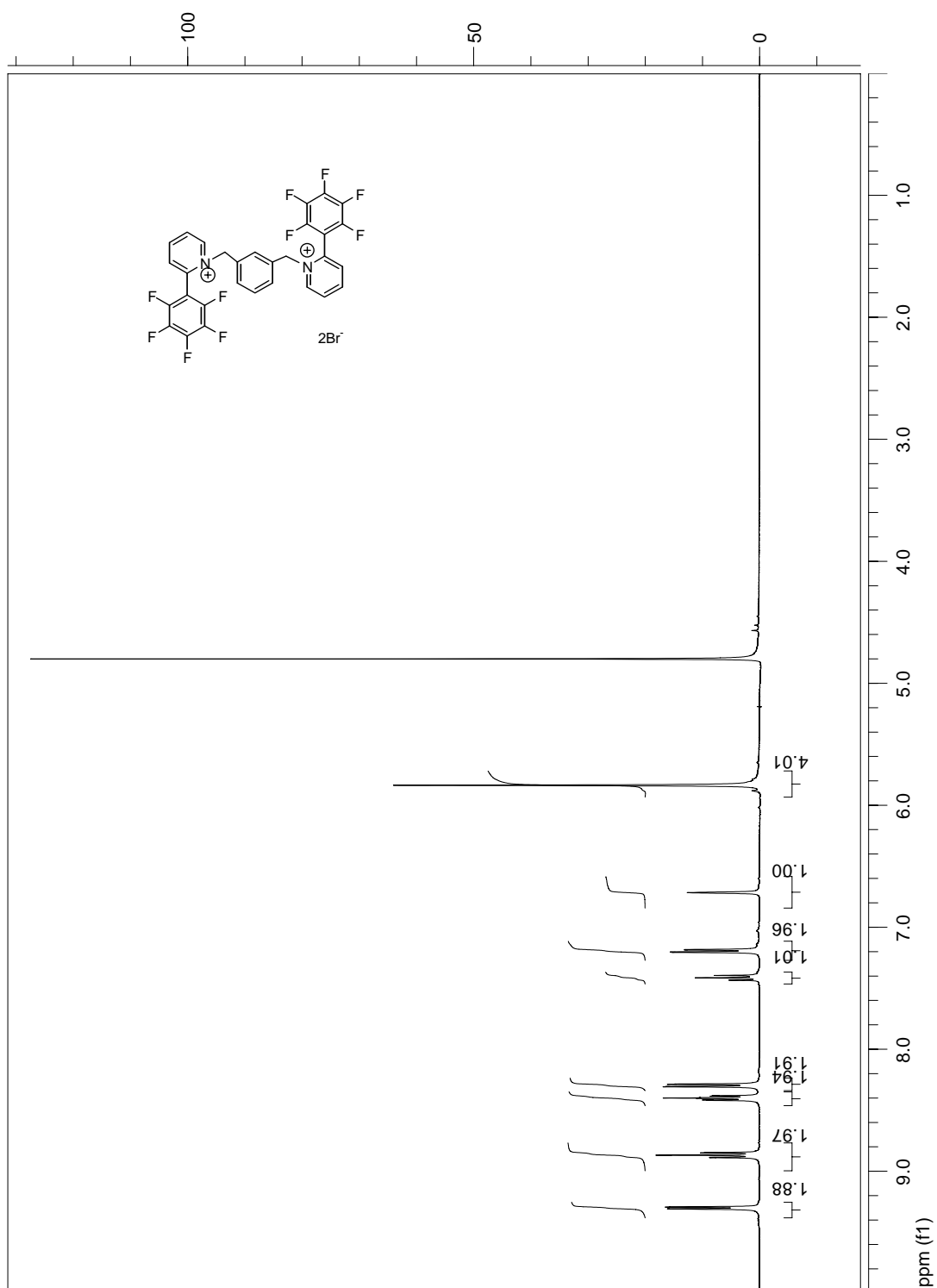
atom/axis	X	Y	Z
O	0.2758	-0.0591	0.253
H	0.276	-0.1045	0.2263
O	-0.0298	-0.0284	0.3055
O	0.3333	0.0962	0.3114
O	0.0078	0.0762	0.158
O	0.1739	-0.1905	0.2008
O	0.3	-0.0731	0.0959
O	0.1775	0.1843	0.2124
C	0.187	-0.0045	0.2227
C	0.1493	0.0388	0.3028
C	0.0457	0.026	0.3411
C	0.0198	0.0644	0.4153
H	-0.0524	0.0564	0.4389
C	0.099	0.1138	0.4541
H	0.081	0.1405	0.5042
C	0.2047	0.125	0.4208
H	0.2599	0.158	0.4484
C	0.229	0.0874	0.3463
C	0.397	0.1688	0.3346
H	0.3477	0.2185	0.3358
H	0.4575	0.178	0.2952
H	0.4298	0.1597	0.3889
C	-0.1468	-0.0159	0.3206
H	-0.1657	-0.0392	0.3742
H	-0.1913	-0.0449	0.2785
H	-0.1639	0.0448	0.3196
C	0.0936	-0.0546	0.1763
C	0.006	-0.0078	0.1396
C	-0.0769	-0.0451	0.0916
H	-0.1346	-0.0116	0.0674
C	-0.0741	-0.1313	0.0795
H	-0.1301	-0.1572	0.0463
C	0.0086	-0.1804	0.1148
H	0.0092	-0.24	0.1062
C	0.0916	-0.1423	0.1633
C	0.1762	-0.2795	0.186
H	0.1057	-0.3049	0.2049
H	0.2399	-0.3048	0.2154

H	0.1844	-0.2898	0.1274
C	-0.072	0.1307	0.1202
H	-0.0663	0.1256	0.0609
H	-0.0568	0.1894	0.1364
H	-0.1481	0.1148	0.1374
C	0.2415	0.0542	0.1569
C	0.2985	0.0136	0.0928
C	0.3508	0.058	0.0301
H	0.388	0.0287	-0.0125
C	0.3474	0.1452	0.031
H	0.3843	0.1761	-0.0107
C	0.2914	0.1882	0.0916
H	0.2898	0.2484	0.0914
C	0.2369	0.1433	0.1533
C	0.168	0.2742	0.2073
H	0.2432	0.2996	0.2097
H	0.1229	0.295	0.253
H	0.1312	0.2896	0.1558
C	0.3352	-0.1194	0.0259
H	0.2901	-0.102	-0.0214
H	0.3249	-0.1801	0.0356
H	0.4149	-0.1078	0.0155
C	0.307	0.6377	-0.0824
H	0.3051	0.5905	-0.1231
Cl	0.1681	0.6707	-0.0633
Cl	0.3863	0.7218	-0.1224
Cl	0.368	0.5999	0.0085
C	0.5257	-0.0182	0.2363
H	0.4427	-0.008	0.2327
Cl	0.5644	-0.0269	0.3398
Cl	0.5575	-0.113	0.1849
Cl	0.5962	0.0673	0.1898

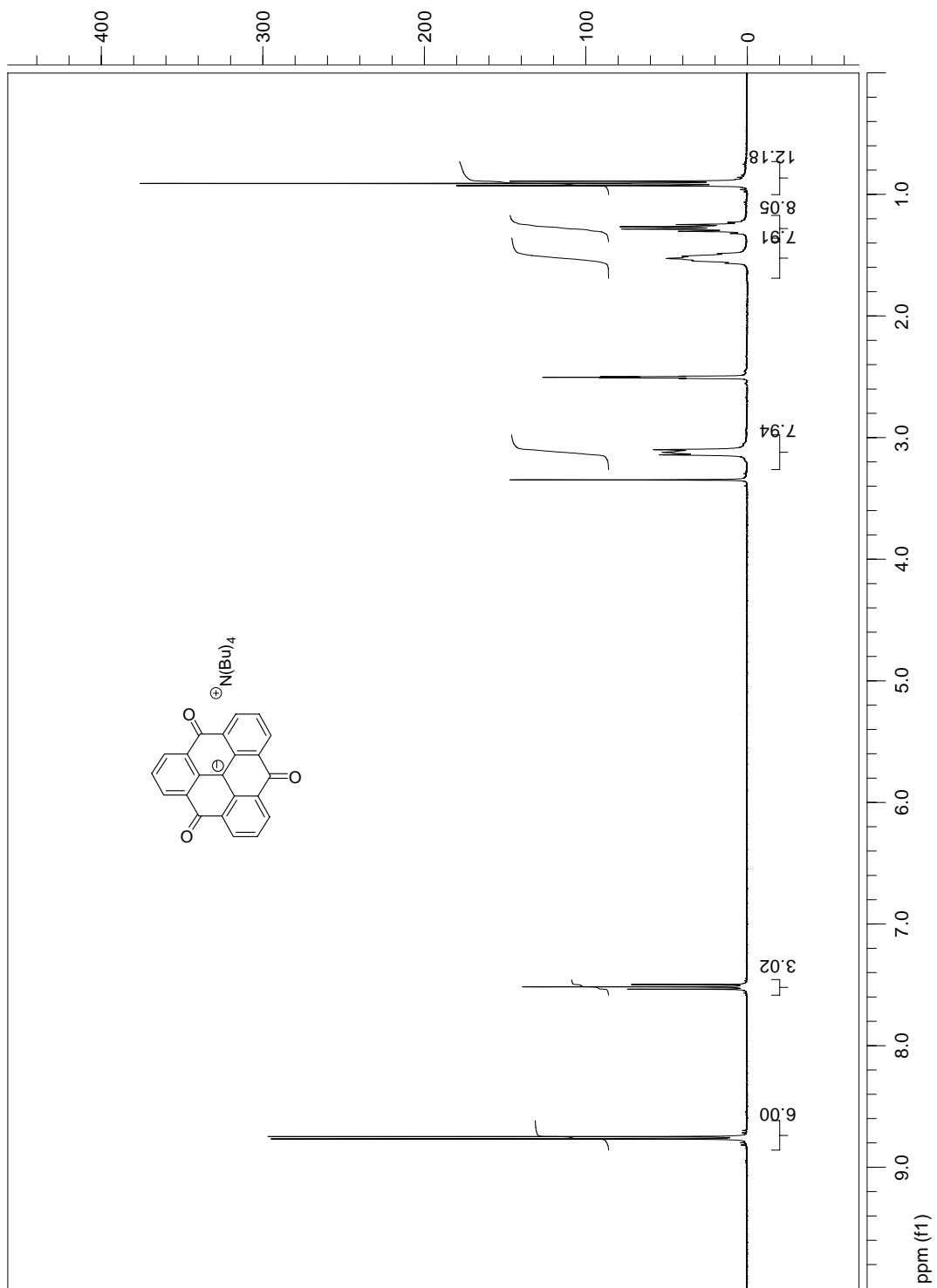




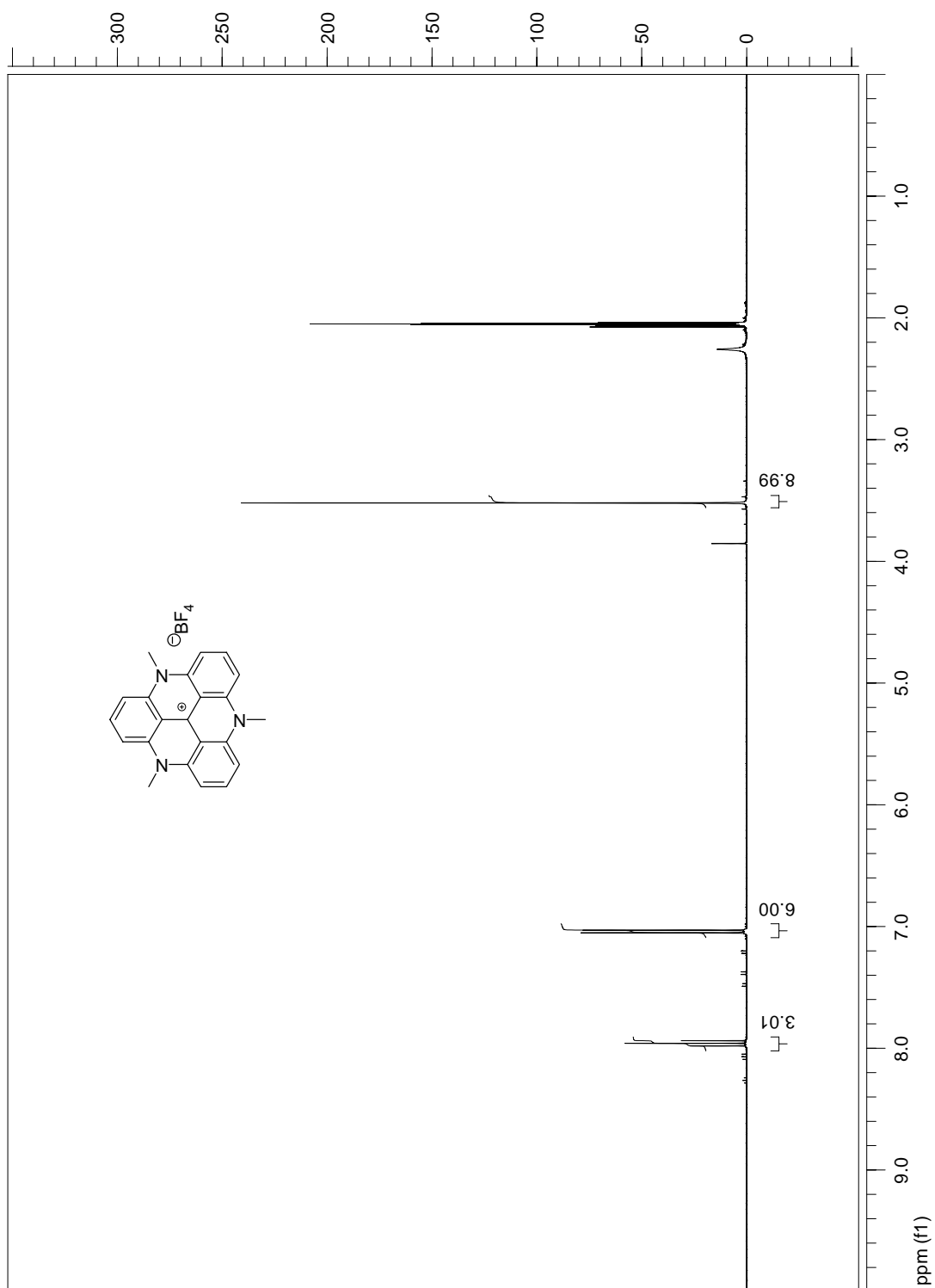
A-20:  $^1\text{H}$  NMR of 2c in  $\text{D}_2\text{O}$



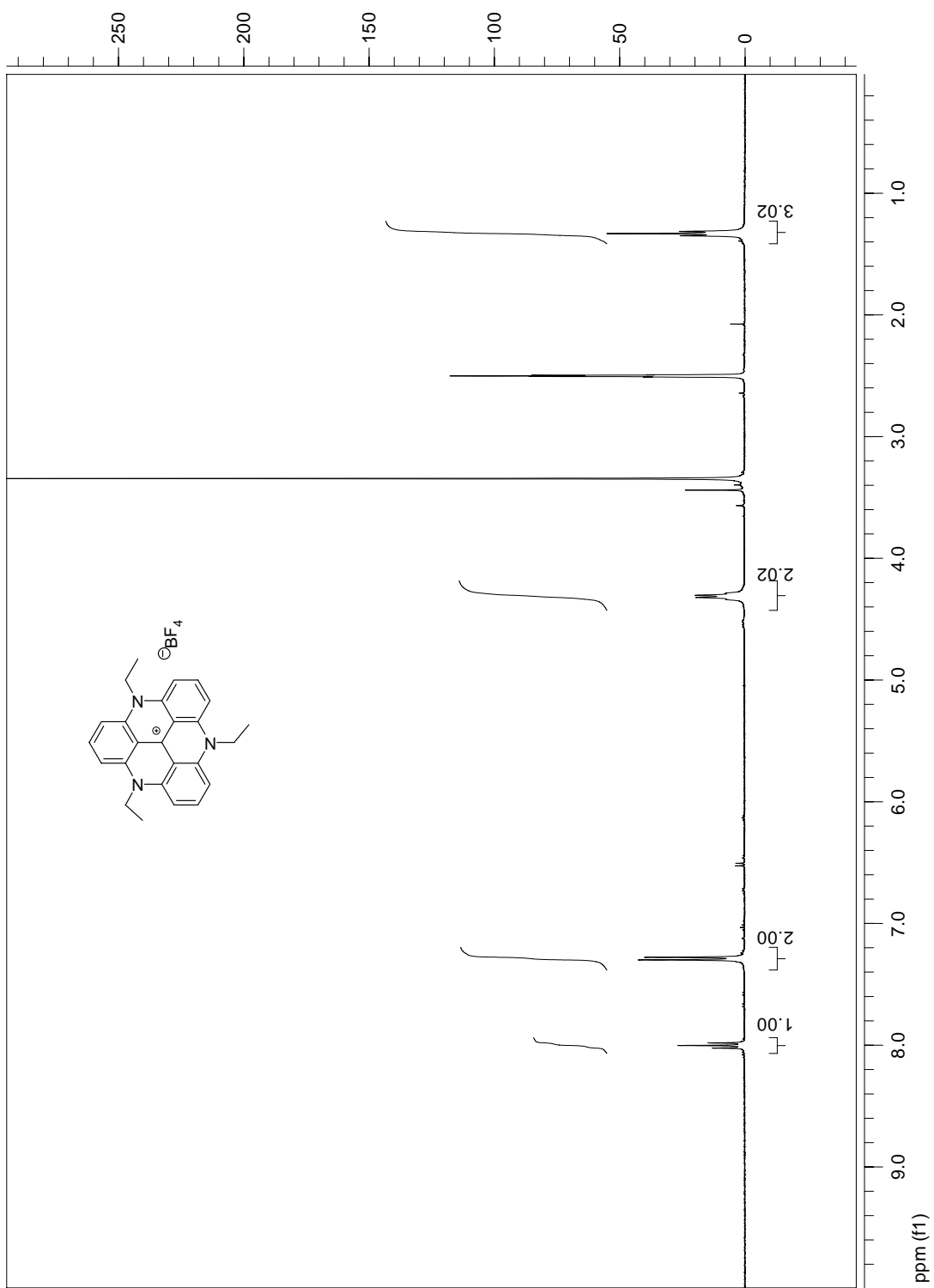
A-21:  $^1\text{H}$  NMR of 3.1 in DMSO



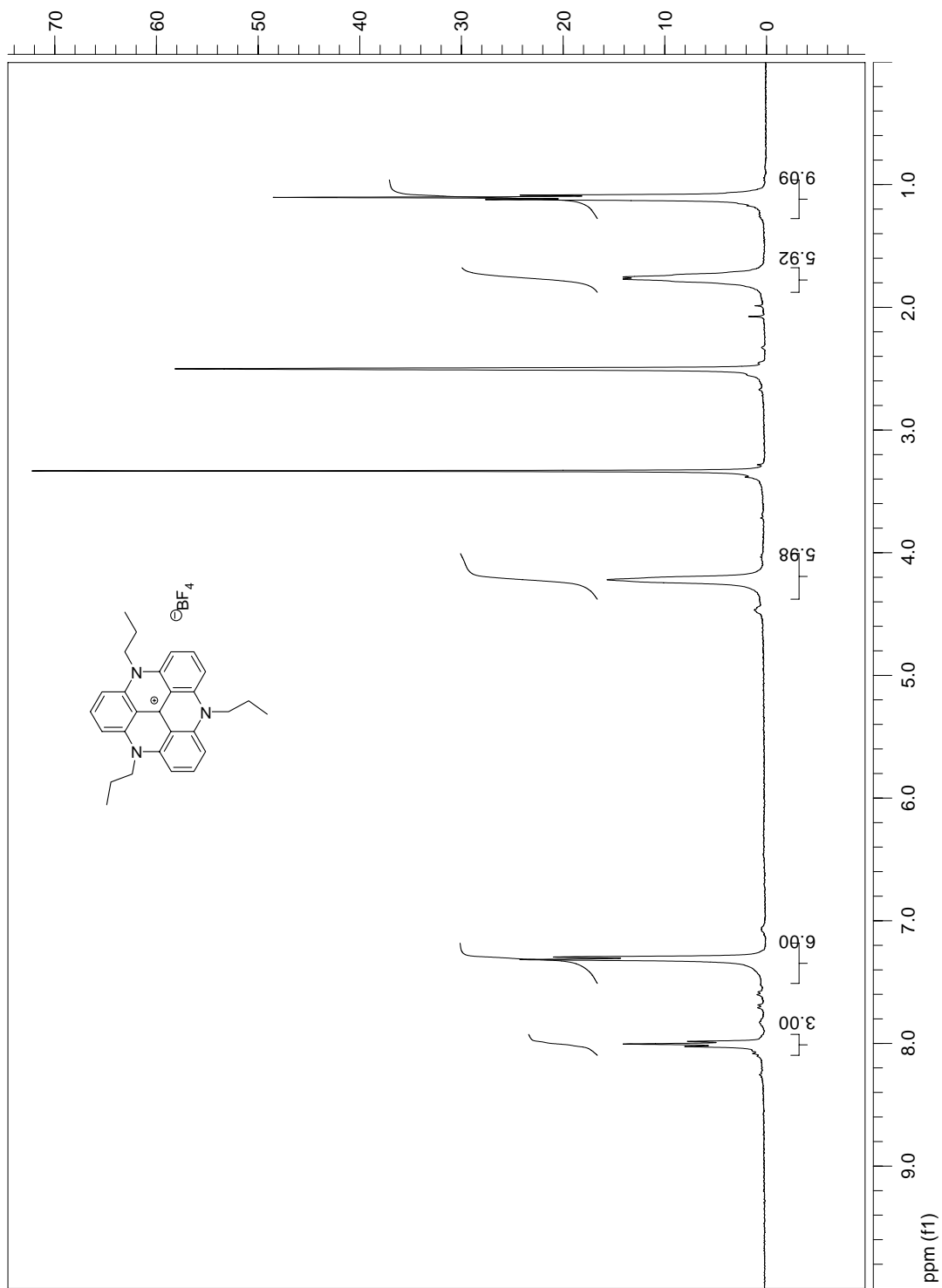
A-22:  $^1\text{H}$  NMR of 3.4 in acetone



A-23:  $^1\text{H}$  NMR of 3.5 in DMSO



A-24:  $^1\text{H}$  NMR of 3.6 in DMSO



## Vita

Jing Chen was born on April 4<sup>th</sup> 1970 in Fujian, P. R. China. He received his high school education from No. 8 Middle School in Fuzhou, P. R. China. He studied Chemistry (1987-1991) at the Nanjing University, P. R. China and received his B. S. degree in Chemistry in July, 1991. He spent three years in the same institution for his graduate study (1997-2000) and received his M. S. degree in Physical Chemistry in July, 2000. He joined the graduate program in the Chemistry Department, University of Kentucky, in August 2000. One year later, he joined the Cammers research group.

### Publications:

- 1) Xiang Hao, Jing Chen, Arthur Cammers, Sean Parkin & Carolyn Pratt Brock. [“A Helical Structure with  \$Z' = 10\$ ”](#), *Acta Cryst.* **2005**, B61, 218-226.
- 2) Jing Chen, Peter G. Willis, Sean Parkin, Arthur Cammers. [“In Search of the Weak, Six-Membered Intramolecular Hydrogen Bond in the Solution and Solid States of Guanidinobenzimidazole”](#), *Eur. J. Org. Chem.* **2005**, 171-178.
- 3) Jing Chen and Arthur Cammers-Goodwin. [“Quantitative Four-state Conformational Analysis by Ring Current NMR Anisotropy: a Family of Molecules Capable of Intramolecular pi-stacking”](#), *Eur. J. Org. Chem.* **2003**, 19, 3861-3867.
- 4) Jing Chen and Arthur Cammers-Goodwin. [“2-\(Fluorophenyl\) pyridines by the Suzuki–Miyaura Method: Ag<sub>2</sub>O Accelerates Coupling over Undesired ipso Substitution \(S<sub>N</sub>Ar\) of Fluorine”](#), *Tet. Lett.* **2003**, 44, 1503-1506.